GLOBAL HYDRLOGIC PERSPECTIVES ON THE MID-CRETACEOUS GREENHOUSE CLIMATE (APTIAN-ALBIAN)

By

© 2009
Marina Bianca Suarez
B.S., Trinity University, 2003
M.S., Temple University, 2005

Submitted to the Department of Geology and the Faculty of the Graduate School of The University of Kansas in partial fulfillment of the requirements for the degree of Doctor of Philosophy

Advisory Committee:

_____
Luis A González, Chair

_____
Gregory A. Ludvigson, Co-Chair

_____
Stephen T. Hasiotis

_____
Bruce S. Lieberman

_____
Edith L. Taylor

Date defended:_____

The dissertation committee for Marina Bianca Suarez certifies
that this is the approved version of the following dissertation:

GLOBAL HYDRLOGIC PERSPECTIVES ON THE MID-CRETACEOUS GREENHOUSE CLIMATE (APTIAN-ALBIAN)

Advisory Committee:

_____
Luis A González, Chair

_____
Gregory A. Ludvigson, Co-Chair

_____
Stephen T. Hasiotis

_____
Bruce S. Lieberman

_____
Edith L. Taylor

Date defended:_____

ABSTRACT

Marina B. Suarez, Ph.D.
Department of Geology, August 2009
University of Kansas

This dissertation examines the mid-Cretaceous greenhouse climate in the Aptian-Albian through the perspective of the global hydrologic cycle. Stable isotopic compositions of pedogenic and exposure surface carbonates presented herein provides low latitude constraints on the oxygen isotopic composition meteoric water during the Cretaceous. Petrographic and isotopic evidence from the Tlayua Formation of Mexico (18.5°N paleolatitude) establishes a shallow-water coastal environment that experienced supratidal conditions in which early meteoric diagenesis occurred. Trends in $\delta^{18}O$ vs. $\delta^{13}C$ space define meteoric calcite lines that are characterized by average $\delta^{18}O$ values of -7.78‰ VPDB (Vienna Pee Dee Belemnite), and are used to calculate meteoric water compositions of -5.46 ± 0.56‰ VSMOW (Vienna Standard Mean Ocean Water). Positive linear covariant trends are defined and used to estimate evaporative losses of vadose groundwater ranging from 8% to 12%. Meteoric sphaerosiderite lines from coastal wetland soils of the Caballos Formation in Colombia (2°N paleolatitude) have an average oxygen isotopic composition of -4.41 ± 0.37‰ VPDB, and are used to calculate meteoric water compositions of -4.56 ± 0.38‰ VSMOW. This new data is incorporated into a revised mass balance model that simulates components of the hydrologic cycle (precipitation , evaporation, oxygen isotopic composition of seawater, relative

humidity and continental feedback). The model simulates the oxygen isotopic composition of water vapor and resulting precipitation. Results suggest precipitation flux and rates were greater in the mid-Cretaceous than modern precipitation flux and rates. Global average precipitation rates for the mid-Cretaceous range between 371 mm/year to 1154 mm/year greater than modern precipitation rates. Sensitivity testing of the model indicates that temperature, air mass origin and pathways, the oxygen isotopic composition of seawater in the low latitudes, and relative humidity are variables that have the potential to greatly affect the oxygen isotopic composition of precipitation, and need greater constraints. These results can be used to further constrain and improve more complex general circulation models to more accurately model the hydrologic cycle during the Aptian-Albian and for future greenhouse climates.

ACKNOWLEDGMENTS

First and foremost I must thank my family, especially my parents: Arturo and Sylvia Suarez, my grandparents: Samuel and Aurora Suarez, and José and Susie Sanchez, my sisters: Bettina Suarez-Cromley, Celina Suarez, and Elisa Suarez, and many aunts, uncles and cousins for the love and understanding they have shown me throughout my studies, and to their commitment and encouragement of my education. Nothing can make up for the birthdays, anniversaries, cross country meets, graduations, births and deaths for which I have been absent during the time spent pursing my research. I hope that the effort put forth in the completion of this dissertation is a small testament of my love for you all and know that I had you all in my thoughts every step of the way and I will continue to do so.

None of this research would have been possible without the support, guidance, and inspiration of great mentors. I am grateful that I have had some of the best: Drs. Edward C. Roy Jr., Dennis O. Terry, Luis A. González, and Gregory A. Ludvigson. I have learned many valuable lessons, both scientific and otherwise from these people. I thank you all for your patience and for believing in my abilities, even and especially when I did not. Thanks to Greg for his persistent positive attitude and his endless enthusiasm. I must especially acknowledge my dissertation advisor, Luis González. As I entered this program I had little understanding of stable isotope geochemistry, and it was his instruction and especially his patience that allowed me to discover the power of stable isotope geochemistry.

Completing this dissertation would not have been possible with the company and support of a great group of fellow graduate students and lab mates. Thanks to Celina Suarez, Julie Retrum, Alvin Bonilla, Darren Welch, Becky Totten, Stacey Rosner, Aisha Al-Suwadii, Emily Tremain, Dr. Jon Smith, Brian Platt, Arne Sturm, Karla Leslie, Ezra Kulczycki, Pete Schillig, and Paul Kenward. I must acknowledge especially my twin sister Celina. She always bore the brunt of my frustrations and I can't thank her enough for putting up with me. Thanks to Stacey for introducing me to the KIEL III and MAT253, and to Dr. Jon Smith for his advice, especially on completing and assembling the final dissertation document. Our lab could not function were it not for the hard work and dedication of our lab manager Greg Cane, as well as the MRB office staff: Terri Herberger, Ann Smith, and Carla Ramirez. Likewise, our department would not function without the hard work of our staff: Gwethalyn Williams, Yolanda Davis, Liz Gravatt, Ian Rowell and Jenna Coker. I must also thank Dr. Francisco Vera and Dr. Jesus Alvarado-Ortega for providing valuable information on the Tlayua Formation

This research was funded by the National Science Foundation grant # EAR-0325072 to Luis Gonzalez and Greg Ludvigson. The Department of Geology at the University of Kansas is acknowledged for summer funding support, teaching assistantships, and scholarships from the Angino Geochemistry Scholarship. Thanks also to Dr. Angino. I have also been supported throughout my college career by the American Geological Institute through the Minority Participation Program. I would

like to thank Cindy Martinez for her work with the program, and for always reminding me to renew my application.

This work is dedicated to the memories of Dr. Edward C. Roy Jr., Samuel Suarez, and Elisa Suarez. Dr. Roy was my first mentor and his caring advice was instrumental in my decision to attend the University of Kansas. My grandfather Samuel Suarez always made me laugh and it's my hope that I will remember to laugh and he will too. Lastly, to my little sister Elisa Suarez in the hope and belief that she shares my adventures.

"Water sustains all."

Thales of Miletus, 600 B.C.E.

"…I go down with the water and come up with the water.

I follow it and forget myself.

I survive because I don't struggle against the water's superior power.

That's all."

Chuang-tse, from *The Tao of Pooh*, by Benjamin Hoff

"By the time it came to the edge of the Forest the stream had grown up, so that it was almost a river, and, being grown up, it did not run and jump and sparkle along as it used to do when it was younger, but moved more slowly. For it knew now where it was going, and it said to itself, 'There is no hurry. We shall get there some day.' But all the little streams higher up in the Forest went this way and that, quickly, eagerly, having so much to find out before it was too late"

A. A. Milne, *The House at Pooh Corner*

TABLE OF CONTENTS

CHAPTER 1. INTRODUCTION

Considering that current atmospheric CO_2 concentrations already exceed the range of pCO_2 values estimated for the Pleistocene and Holocene (Ruddiman, 2005; Soreghan et al., 2003) study of ancient systems with much higher CO_2 concentrations are necessary to gain insights into future climate change and to validate climate models. The mid-Cretaceous with its high pCO_2, shallow temperature gradients, warm high latitudes, absence of polar ice, and an intensified hydrologic cycle (Ludvigson et al., 1998; Jenkyns et al., 2004; Poulsen, 2004; Ufnar et al., 2004) have the extreme conditions, relative to the modern climate, needed to validate climate models. Moreover, during the warm climate of the Cretaceous, important evolutionary events occurred including the origination of angiosperms and advancement in the evolution among social insects, modern lizards, mammals and birds. Indeed, the Cretaceous is regarded as the time when modernization of terrestrial ecosystems took place; an event termed the Cretaceous Terrestrial Revolution (Lloyd et al., 2008).

Given the vital role of the hydrologic cycle in biogeochemical cycles, global temperature regulation, and the evolution of life on the planet (particularly in terrestrial systems) the study of this aspect of the global climate system is of extreme importance. Over the past two decades studies of the mid-Cretaceous hydrologic cycle response to increased global warmth have resulted in significant advance in our state of knowledge (Barron et al., 1989; Ludvigson et al., 1998; Hay and DeConto, 1999; Ufnar et al., 2002, 2004). This has led to the recognition of significant

differences between climate model outputs and the inferences or extrapolations based on geological and paleontological data. An important goal of recent studies has been to reconcile the known differences between climate models and climate proxies (e.g., Poulsen et al., 2007) and the generation of larger proxy data sets and derived climate data (e.g., White et al., 2001; Ufnar et al, 2002, 2004; Ludvigson et al., 2003, 2004).

This dissertation examines the global greenhouse during the Aptian-Albian and aims to gain a better understanding of the hydrologic cycle during periods of elevated CO_2 and temperatures. This study contributes low latitude stable oxygen isotopic proxy data from carbonates described in chapters 2 and 3. This data is incorporated into an improved hydrologic cycle mass balance model presented in chapter 4.

As global temperature increases, the ability of the atmosphere to hold more water vapor also increases, and it is widely held that increased temperature should result in an intensified hydrologic cycle, with global circulation model (GCM) results supporting this hypothesis (Barron et al., 1989; Hay and DeConto, 1999). From the mid 1990's to the early part of this century the Kansas Cretaceous Studies Group (formerly the Iowa Cretaceous Studies Group), under the direction of principal investigators Gregory A. Ludvigson and Luis A. González, generated a profuse amount of stable isotope data ($\delta^{18}O$ and $\delta^{13}C$) from sphaerosiderites formed in wetland soils from localities ranging from 35°N to 75°N (White et al., 2001; Ufnar et al., 2002). The utility of sphaerosiderite $\delta^{18}O$ as a hydrologic cycle proxy was noted by Ludvigson et al. (1998) who recognized meteoric sphaerosiderite lines (MSLs),

which, like meteoric calcite lines (MCLs), are vertical trends in $\delta^{18}O$ vs. $\delta^{13}C$ space. The invariant oxygen isotopic compositions of these trends reflect the oxygen isotopic composition of stable non-evaporative meteoric groundwater in saturated paleosols.

Portions of this extensive data set were utilized by White et al. (2001) to explore the mid-Cretaceous hydrologic cycle. A more complete data set was utilized by Ufnar et al. (2002) who developed a simple mass balance model that uses the oxygen isotopic composition of sphaerosiderites to estimate precipitation and evaporation fluxes over northern hemisphere America. The findings of these studies suggest significant increases in precipitation in the mid to high latitudes. Since data in these studies were limited to 35°N and 75°N, there is need for additional coverage in the tropics to test the validity of the findings of those studies as they relate to the lower latitudes.

Chapter 2 discusses the proxy data obtained from limestones of the Tlayua Formation of Puebla, Mexico (~18.5°N paleolatitude). This chapter has been published in the Bulletin of the Geological Society of America (Suarez et al., 2009). The Tlayua Formation site is an important fossil locality in which marine, freshwater, and terrestrial flora and fauna are preserved. Petrographic observations (fenestral fabrics, gypsum crystal molds, stromatolitic structures, and pedogenic matrix birefringence fabric) and interpretation of MCLs from isotopic analyses of stable oxygen and carbon of micrites confirm a shallow near-shore depositional environment. Meteoric calcite lines are used to calculate meteoric water

compositions. In addition to the meteoric calcite lines, the study uses *positive linear covariant trends* (PLCT) in oxygen and carbon isotopic values from some horizons to estimate evaporative losses of the vadose groundwater.

Chapter 3 describes sphaerosiderites from lowland soils of the Caballos Formation in the Upper Magdalena Valley of Colombia (~2°S paleolatitude) and provides equatorial, and our only southern hemisphere data set. Macroscopic and microscopic soil features establish that these soils developed in coastal settings near sea level, and were often water saturated. The common appearance of pyrite suggests occasional influence of marine fluids. Well formed sphaerosiderites produce MSLs that are used to calculate the oxygen isotopic composition of meteoric water.

In chapter 4, the mass balance model developed by Ufnar et al. (2002) is modified and integrated with data from the Tlayua Formation (chapter 2), the Caballos Formation (chapter 3), and data from the Cedar Mountain Formation reported by Ludvigson et al. (2003), and data from the Antlers, Walnut, and Glen Rose Formations reported by Ludvigson et al. (2004). The combination of calcite and siderite oxygen isotopic data requires that the oxygen isotopic compositions of meteoric water be calculated in order to maintain a consistent empirically derived data set for model comparison. In addition to the new oxygen isotopic constraints, the revised model also incorporates air mass origin, composition and pathway as inputs. It provides for latitudinal variations in seawater composition, and variable terrestrial feedback. Precipitation flux, evaporation flux, relative humidity, $\delta^{18}O$ of seawater and terrestrial feedback are adjusted to simulate the oxygen isotopic

composition of precipitation and it is matched to the empirically derived meteoric compositions. Model results suggests that precipitation fluxes and rates for the range of temperature gradients hypothesized for the Cretaceous are greater than modern fluxes and rates. In addition to providing precipitation rate estimates, the model was tested to determine the sensitivity of different variables on the oxygen isotopic composition of precipitation.

REFERENCES

Barron, E. J., Hay, W. W., and Thompson, S., 1989, The hydrologic cycle: A major variable during Earth History: Palaeogeography, Palaeoclimatology, Palaeoecology, v. 75, p. 157-174.

Hay, W. W. and DeConto, R.M., 1999, Comparison of modern and Late Cretaceous meridional energy transport and oceanology, *in* Barrera, E., and Johnson, C.C., ed., Evolution of the Cretaceous ocean-climate system: Boulder, Geological Society of America Special Paper 332, p. 283-300.

Jenkyns, H. C., Forster, A., Schouten, S., Sinninghe Damste, J.S., 2004, High temperatures in the Late Cretaceous Arctic Ocean: Nature, v. 432, p. 888-892.

Lloyd, G. T., Davis, K. E., Pisani, D., Tarver, J. E., Ruta, M., Sakamoto, M., Hone, D. W. E., Jennings, R., and Benton, M. J., 2008, Dinosaurs and the Cretaceous terrestrial revolution: Proceedings of the Royal Society B, v. 275, p. 2483-2490.

Ludvigson, G., González, L.A., Metzger, R.A., Witzke, B.J., Brenner, R.L., Murillo, A.P., White, T.S., 1998, Meteoric sphaerosiderite lines and their use for paleohydrology and paleoclimatology: Geology, v. 26, no. 11, p. 1039-1042.

Ludvigson, G. A., González, L.A., Kirkland, J.I., and Joeckel, R.M, 2003, A mid-Cretaceous record of carbon isotope excursions in palustrine carbonates of the Cedar Mountain Formation of Utah: Marine-terrestrial correlations of Aptian-Albian oceanic anoxic events 1a, 1b, and 1d: The 3rd International Limnogeology Congress, March 29-April 2, Tucson, Arizona, Abstract Volume, p. 169.

Ludvigson Greg, A., Ufnar David, F., González Luis, A., Carpenter Scott, J., Witzke Brian, J., Brenner Robert, L., Davis, J., and Anonymous, 2004, Terrestrial paleoclimatology of the Mid-Cretaceous greenhouse; I, Cross-calibration of pedogenic siderite & calcite $\delta^{18}O$ proxies at the Hadley Cell boundary.; Geological Society of America, 2004 annual meeting: Abstracts with Programs Geological Society of America, v. 36, no. 5, p. 305.

Poulsen, C. J., 2004, A balmy arctic: Nature, v. 432, p. 814-815.

Poulsen, C. J., Pollard, D., and White, T.S., 2007, General circulation model simulation of the $\delta^{18}O$ content of continental precipitation in the middle Cretaceous: a model-proxy comparison: Geology, v. 35, p. 199-202.

Ruddiman, W. F., 2005, Plow, Plagues, and Petroleum: How humans took control of climate: Princeton, Princeton University Press, 224 p.

Soreghan, G. S., Maples, C.G., Parrish, J.T., 2003, Report of the NSF sponsored workshop on paleoclimate, *in* Paleoclimate Workshop, Arlington, VA.

Ufnar, D. F., González, L.A., Ludvigson, G.A., Brenner, R.L., Witzke, B.J., 2002, The mid-Cretaceous water bearer: isotope mass balance quantification of the Albian hydrologic cycle: Palaeogeography, Palaeoclimatology, Palaeoecology, v. 188, p. 51-71.

-, 2004, Evidence for increased latent heat transport during the Cretaceous (Albian) greenhouse warming: Geology, v. 32, no. 12, p. 1049-1052.

White, T., González, L., Ludvigson, G., and Poulsen, C., 2001, Middle Cretaceous greenhouse hydrologic cycle of North America: Geology, v. 29, no. 4, p. 363-366.

CHAPTER 2. ISOTOPIC COMPOSITION OF LOW-LATITUDE PALEO-PRECIPITATION DURING THE EARLY CRETACEOUS

ABSTRACT

The response of the hydrologic cycle in global greenhouse conditions is important to our understanding of future climate change and to the calibration of global climate models. Past greenhouse conditions, such as that of the Cretaceous, can be used to provide empirical data with which to evaluate climate models. Recent empirical studies have utilized pedogenic carbonates to estimate the isotopic composition of meteoric waters and calculate precipitation rates for the Aptian-Albian. These studies were limited to data from mid (35°N) to high (75°N) paleolatitudes, and thus future improvements in accuracy will require more estimates of meteoric water compositions from numerous localities around the globe. This study provides data for tropical latitudes (18.5°N paleolatitude) from the Tlayua Formation (Puebla, Mexico). In addition, the study confirms a shallow near-shore depositional environment for the Tlayua Formation. Petrographic observations of fenestral fabrics, gypsum crystal molds, stromatolitic structures, and pedogenic matrix birefringence fabric, support the interpretation that the strata represent deposition in a tidal flat environment. Carbonate isotopic data from limestones of the Tlayua Formation provide evidence of early meteoric diagenesis, in the form of meteoric calcite lines. These trends in $\delta^{18}O$ vs. $\delta^{13}C$ crossplots are used to calculate the mean $\delta^{18}O$ value of meteoric water, which is estimated at -5.46 ± 0.56‰ (Vienna

Standard Mean Ocean Water [VSMOW]). *Positive linear covariant trends* in oxygen and carbon isotopic values from some horizons are used to estimate evaporative losses of vadose groundwater from tropical exposure surfaces during the Albian, with values that range from 8% to 12%. However, the presence of evaporative mineral molds indicates more extensive evaporation.

The added tropical data improves latitudinal coverage of paleo-precipitation $\delta^{18}O$ estimates. The data presented imply that earlier isotope mass balance models most likely underestimated tropical to subtropical precipitation and evaporation fluxes. The limited latitudinal constraints for earlier isotope mass balance modeling of the Albian hydrologic cycle of the northern hemisphere Americas resulted in extrapolated low latitude precipitation $\delta^{18}O$ that are much heavier (up to 3‰) than those observed in this study. The lighter values identified in this study indicate a more pronounced rainout effect for tropical regions and quite possibly a more vigorous evaporation effect. These and additional low latitude data are required to better constrain changes in the hydrologic cycle during the Cretaceous greenhouse, and to reduce the uncertainties resulting from limited geographic coverage of proxy data.

INTRODUCTION

The hydrologic cycle is a major variable in the evolution of the Earth system (Barron et al., 1989). Chahine (1992) suggested that most uncertainties in global-scale perturbations within the global climate system are due to inadequate understanding of

the hydrologic cycle and its interactions with other parts of the global climate system. The persistence of these major scientific uncertainties about the extent to which precipitation and evaporation rates change in response to the forcing of higher global temperatures is highlighted by the recent findings of Zhang et al. (2007) and Graversen et al. (2008). Zhang et al. (2007) report observations of recent increases in high latitude precipitation rates and decreases in subtropical precipitation rates that are greater in magnitude than those estimated from general circulation models of global climate. Graversen et al. (2008) suggested that higher than expected Arctic temperature increases (i.e. "Arctic amplification") in both the lower and upper atmosphere might be the result of increased northward atmospheric transport of heat and moisture. If general circulation models originally tuned for modern climate forecasting do not capture the details of changes in the hydrologic cycle during the historic warming of the late 20th century, then how can their performance be improved to better forecast the pending changes in precipitation and evaporation rates forced by near-range twenty-first century warming?

Paleoclimatologic studies that can better quantify the hydrologic cycles during past greenhouse conditions offer an empirical approach to better constrain the boundary conditions needed for fine-tuning climate models of near-range future climates. Meteoric $\delta^{18}O$ values calculated from isotopic compositions of pedogenic and freshwater carbonates have been used to better quantify the paleohydrologic cycle in the mid-Cretaceous greenhouse (Ludvigson, 1998; White et al., 2001; Ufnar et al., 2002, 2004; Poulsen et al., 2007). Ufnar et al. (2002) developed an oxygen

isotope mass balance model based on meteoric $\delta^{18}O$ values of North American pedogenic sphaerosiderites (meteoric sphaerosiderite lines or MSLs). The model results indicate intensification of precipitation in the equatorial and mid to high latitudes, and intensification of evaporation in the sub-tropics. Ufnar et al. (2004) suggest that increased latent heat transport to the polar regions via an intensified hydrologic cycle contributed to Cretaceous polar warmth as now proposed by Graversen et al. (2008) for modern arctic warming. The model, however, was based solely on pedogenic siderite data from the mid (~35° N) to high latitudes (~75°N), and thus greater uncertainty is added by the lack of sub-tropical to equatorial empirical data with which to constrain the modeling exercise. To further test the accuracy and to improve on the findings of the mass balance modeling, it is imperative that the latitudinal empirical data be expanded to tropical latitudes. The addition of low latitude data is not only necessary to improve the mass balance-dependant precipitation and evaporation rates of the Ufnar et al. (2002) model, but they are also needed to improve comparisons between proxy data and general circulation models which now generate oxygen isotope values for precipitation (Poulsen et al., 2007).

Relevant data from the dry tropical to subtropical latitudes can be extracted from shallow marine-supratidal carbonates that experienced early meteoric diagenesis. Micritic domains of exposed shallow marine sediments frequently undergo early diagenetic stabilization by meteoric water in which the carbonate oxygen isotopic values are determined by the isotopic composition of mean annual

rainfall, and the carbon values are modified by dissolved CO_2 derived from the oxidation of soil organic matter (Lohmann, 1988; Banner and Hanson, 1990). These diagenetic carbonates often produce unique systematic linear trends in $\delta^{13}C$ versus $\delta^{18}O$ crossplots defining meteoric calcite lines (MCLs *sensu* Lohmann, 1988), which are linear trends with more variable carbon isotopic values and invariant oxygen isotopic values.

The Albian Tlayua Formation in southern Mexico was considered an ideal candidate to capture tropical meteoric signals because it had been interpreted to represent a shallow water back-reef lagoon with episodic freshwater input (Malpica-Cruz et al., 1989; Pantoja-Alor, 1992; Espinosa-Arrubarrena and Applegate, 1996; Applegate et al., 2006). However, at the onset of our investigation, Kashiyama et al. (2004) questioned the shallow fresh-water influenced interpretation and suggested an open marine basin for the origin of the Tlayua Formation. Thus, a more rigorous petrographic evaluation and an expanded stable isotopic analysis was undertaken to determine the nature of Tlayua depositional environments. The results of our analyses confirm the shallow marine to terrestrial depositional environment. Freshwater early diagenetic signatures allow us to extend the latitudinal meteoric $\delta^{18}O$ data into the tropics.

In addition to its contribution to global paleoclimate study, the Tlayua Formation at the Tlayua Quarry study site contains numerous well-preserved vertebrate and invertebrate fossils of mixed marine, freshwater, and terrestrial origin, as well as soft-tissue preservation (Martill, 1989; Pantoja-Alor, 1992; Appelgate et

al., 2006; Alvarado-Ortega et al., 2007). Isotopic and petrographic study provides further paleoenvironmental data to help understand this extraordinary paleontological resource.

GEOLOGIC SETTING

The Tlayua Formation, described by Pantoja-Alor (1992), crops out in the southern area of the Mexican state of Puebla known as Tepexi de Rodríguez (Figure 1). In this area, Late Paleozoic low-grade metamorphosed rocks (phyllites and schists) through early Tertiary sedimentary rocks rest on Early Paleozoic tectonic fault blocks called the Acatlán Complex (Pantoja-Alor, 1992). This complex was an emergent area of land exposure during the Jurassic and possibly the Early Cretaceous (Applegate et al., 2006).

The Tlayua Formation consists of three carbonate members (Pantoja-Alor, 1992; Applegate et al., 2006). The Lower Member consists of at least 50 m of bluish-gray, massive micritic (mudstone to wackestone) limestone. This member is characterized by intraclasts, miliolids, 20-50-cm-high rudist biostromes, inoceramids, and chert concretions and lenses. The member is capped by a horizon of small bivalves and gastropods. The rudist *Toucasia polygyra* and the inoceramid *Chondrodonta sp.* are used to assign a lower Albian age to this member (Alencáster, 1973).

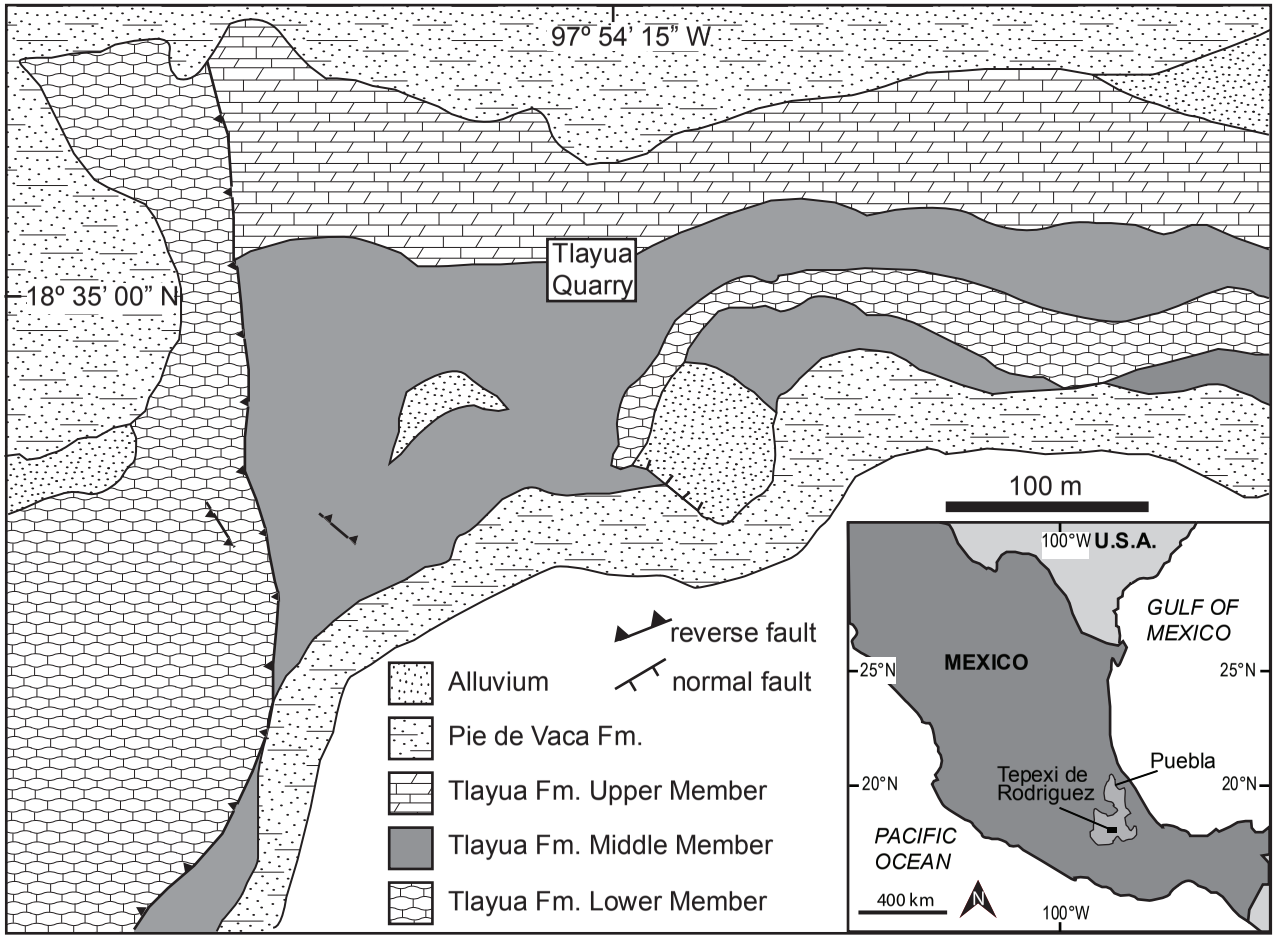

FIGURE 1—Local geologic map and location of the Tlayua Quarry in south-central Mexico. Modified from Applegate et al. (2006).

The Middle Member consists of 35 m of thinly bedded to laminated yellow-brown micritic limestone with reddish-yellow to purplish-red hematitic partings to thin hematitic clay layers. The Tlayua Quarry exposes most of the Middle Member, and it is from this unit that the majority of the well-preserved fossil material is found. The invertebrate fauna includes foraminfera, two unidentified sponges, two unidentified corals, bivalves, gastropods, cephalopods, arthropods (including arachnids, insects, isopods, decapod crabs, and ostracods), and echinoderms (see Appelgate et al., 2006 for complete faunal and floral list). The fossil assemblage of the Tlayua Quarry is dominated (70%) by fishes of both marine and freshwater origin. Other vertebrate fossils include turtles, pterosaurs, crocodiles, and lizards (Reynoso, 1997, 2000, 2006). A few fragmentary plant fossils have also been recovered. Based on biostratigraphic and magnetostratigraphic analysis, the Middle Member is considered to be Albian (Benammi et al., 2006).

The conditions of preservation for the Tlayua Quarry have, and continue to be a subject of intensive study. The shallow, marginal marine hypothesis cites evidence for periodic exposure and freshwater influences and proposes the presence of stagnant, hypersaline environments and anaerobic conditions leading to superb preservation. Evidence includes algal mats, mudcracks, and the mixed marine, freshwater and terrestrial fauna. The open marine basin hypothesis of Kashiyama et al. (2004) suggests that deep water leading to anaerobic to dysaerobic conditions are responsible for preservation, and suggest that stylolites and wavy pressure-solution

features and/or the recrystallization of primary fabrics have mistakenly been identified as shallow water indicators, such as algal mats.

The Upper Member of the Tlayua Formation is a truncated sequence of dolomite and dolomitic limestone. Petrographically, the Upper Member ranges from dolomite with intraclasts and miliolids to dolomite crystals in a micritic matrix (Pantoja-Alor, 1992). The miliolid species *Dicyclina schlumbergeri* is used to assign a Cenomanian age for this member (Pantoja-Alor, 1992). The Upper Member is truncated by overlying Cenozoic continental deposits.

METHODS

Samples were collected from the active quarry in the Middle Member at 1 m intervals (Figure 2), and where there were distinct lithologic changes. A total of 27 samples were collected. Each sample was slabbed to produce two 1-3-cm-thick slabs. One of the two slabs for each sample was used to produce a 50 x 76 mm petrographic thin section, while the other slab was polished and used for isotopic sampling. Petrographic thin sections were used for identification of structures that could be used as indicators for depositional environment, identification of diagenetic features, and identification of various carbonate domains for isotope sampling. Carbonates are classified using Folk (1962), with Dunham (1962) in parentheses. Stable isotope samples were milled from polished slabs using a microscope-mounted dental drill with 3-500-µm-diameter tungsten-carbide burrs to produce samples ranging from 25 to 100 µg, and analyzed at the W.M. Keck Paleoenvironmental and

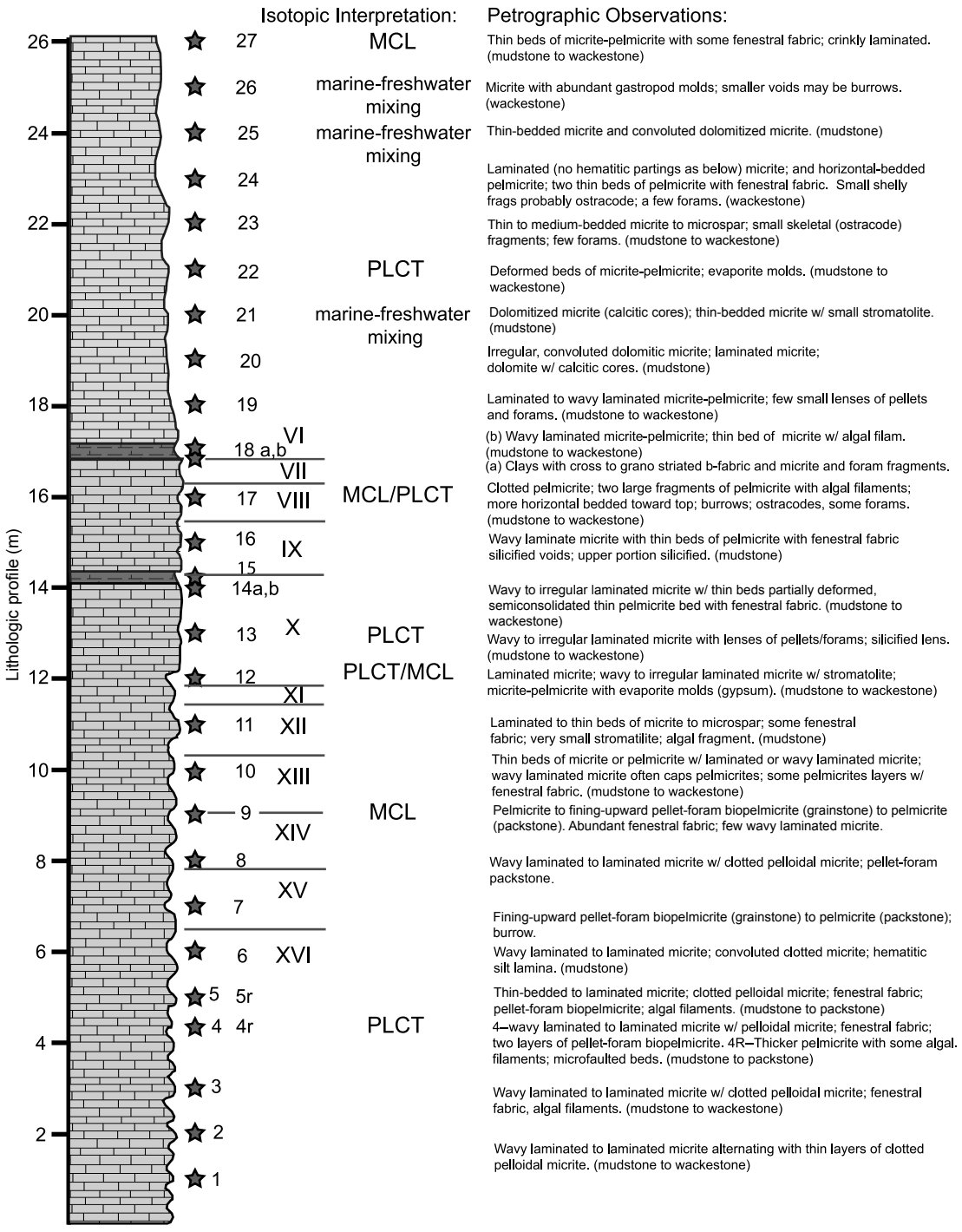

FIGURE 2—Lithologic profile of the Tlayua Quarry. Stars indicate sample positions. Roman numeral divisions are strata designations used by the quarry operators. The middle column indicates interpretation of carbonate isotopic composition indicative of either meteoric calcite lines (MCL) or positive linear covariant trends (PLCT). The right column contains petrographic observations.

Environmental Stable Isotope Lab at the University of Kansas. Individual beds were sampled repetitively to evaluate their unique intrinsic variability, and to define diagenetic trends in carbon-oxygen isotope space that yielded information on the paleohydrologic processes that led to stabilization of each bed. Samples were vacuum roasted at 200°C for one hour to remove volatile contaminants and analyzed using phosphoric acid digestion at 75° C on a ThermoFinnigan Kiel III single sample acid dosing system connected to a ThermoFinnigan MAT 253 isotope ratio mass spectrometer. Precision was monitored by daily analysis of NBS-18 and NBS-19 and is better than 0.1 ‰ for both carbon and oxygen. All carbonate data are reported relative to VPDB. Confidence ellipses were generated using PAST (paleontological statistics software version 1.79; Hammer et al., 2008), and the principal axes of the ellipses was calculated using algorithms presented in Sokal and Rohlf (1995). All other statistics were calculated using data analysis toolpack for Excel® 2008.

RESULTS

Petrography

Lower laminated facies

The lowermost 19 meters of the section consist primarily of laminated to wavy laminated micrites (mudstones) and pelmicrites (wackestones) with hematitic (occasionally silty) partings. Many of the pelmicrites (wackestones) are characterized by fenestral fabrics (Figure 3A), and some of the laminated to wavy laminated micrites (mudstones) are stromatolitic (Figure 3B). Cyanobacteria filaments (Figure

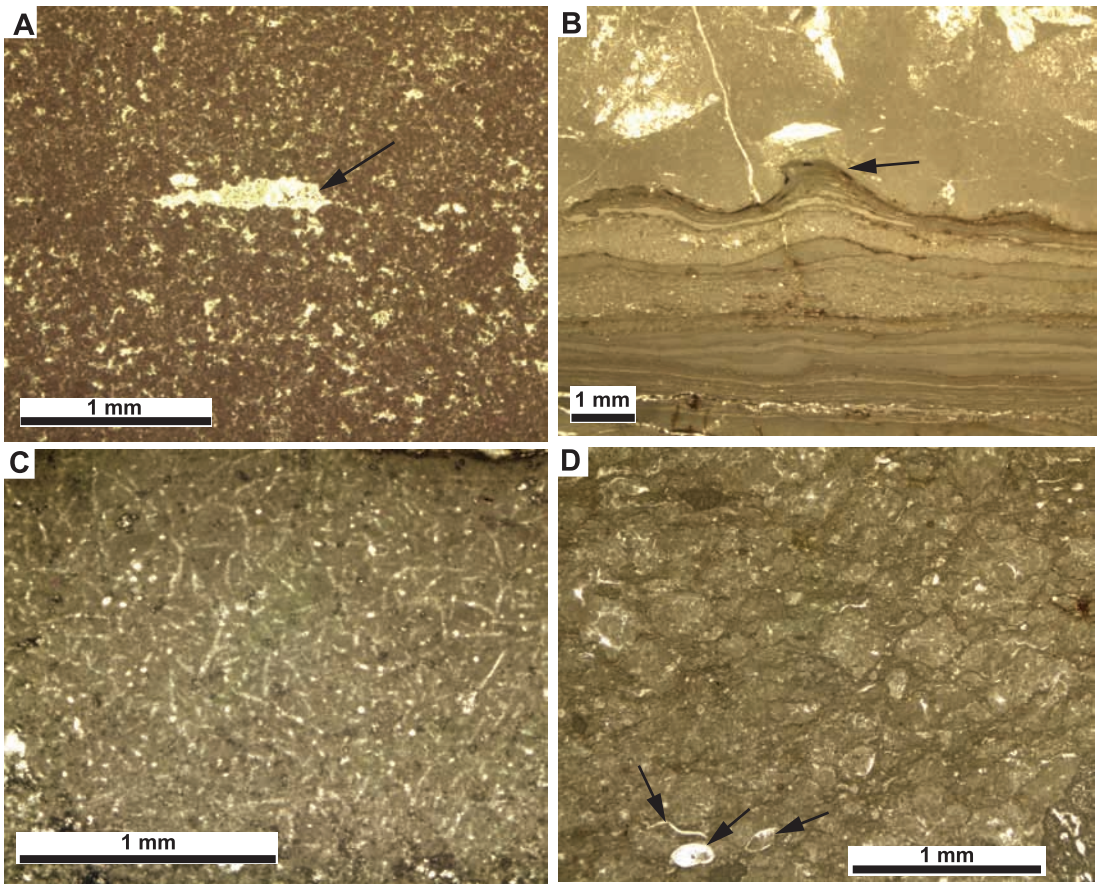

FIGURE 3—Features of the lower laminated facies. Photomicrographs taken with plane polarized light. All scale bars are 1 mm. (A) Fenestral fabric (bird's eye structure) from sample 5 indicated by arrow. (B) Laminated micrite and small stromatolite from sample 12 indicated by arrow. (C) Cyanobacterial filaments from sample 5R. (D) Clotted micrite texture and ostracodes (indicated by arrow) in sample 17.

3C) are also present in the micrites and pelmicrites. Lenses to thin beds of foraminiferal biopelsparite (packstones) are less common than the pelmicrites and micrites, but are consistently present in some of these units.

There are some notable exceptions to the laminated lithologies that dominate the lowermost 19 meters. Samples 7 and 9 consist of a foraminiferal biopelsparite (packstone) that fines upward to a pelmicrite (wackestone). Sample 7 preserves a small part of a vertical *skolithos*-like burrow. A fossiliferous intrapelmicrite (wackestone) occurs at 16 meters above the base of the section. This unit consists of a clotted texture of pelleted intraclast, abundant ostracodes and miliolid foraminifera, and a few micrite clasts (approximately 1 cm) that contain common cyanobacterial filaments (Figure 3D).

Upper bedded facies

The uppermost seven meters consist primarily of thin-bedded to thick-bedded micrite (mudstone) to pelmicrite (wackestone) and microspar, little to no hematitic partings are present, and foraminifera are less abundant. Micrite (mudstone) and dolomitized micrite characterized by distinct dolomite rhombs with calcitic centers (i.e. dedolomite) occur in samples 20, 21 and 25 (Figure 4A). Sample 26 consists of massive micrite with abundant gastropods (wackestone). The uppermost part of the section (sample 27) has crinkly laminated fabric with micrite (mudstone), microspar and sparry calcite (Figure 4B). Secondary structures are common throughout the

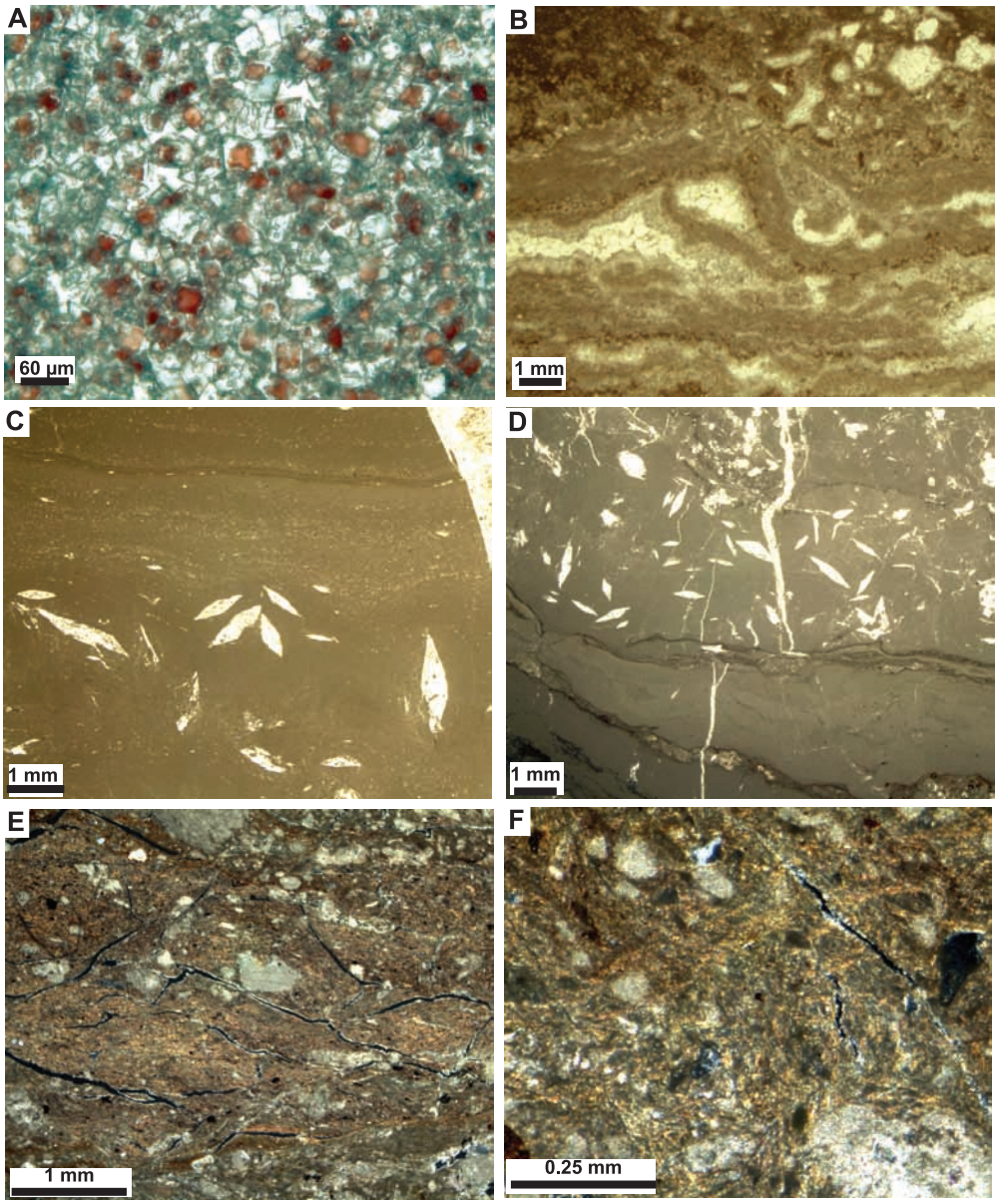

FIGURE 4—Features of the upper bedded facies, evaporites, and paleosols. Photomicrographs A to D taken with plane polarized light. Photomicrographs E and F taken with crossed-polarized light. (A) Dolomite with calcitic centers (stained red with Alizarin Red S) from sample 20. Scale bar is 60 µm. (B) Crinkly-laminated texture from sample 27. Scale bar is 1 mm. (C) Calcite spar-filled gypsum molds from lower laminated facies, sample 12. Scale bar is 1 mm. (D) Calcite spar-filled gypsum molds from the upper bedded facies, sample 22. Scale bar is 1 mm. (E) Micritic clasts surrounded by birefringence clays within the paleosol at sample 18A. Scale bar is 1 mm. (F) Photomicrograph showing cross-striated birefringent fabric and grano-striated birefringence fabric within the paleosol at sample 18A. Scale bar is 0.25 mm.

section including soft-sediment deformation, microfaults, stylolites, silicified lenses, and calcite-filled veins.

Evaporite crystal molds

Calcite-filled molds of gypsum crystals are found at twelve (sample 12) and twenty-one (sample 22) meters above the base of the section (Figure 4C-D). Sample 12, contains soft-sediment deformed laminations while sample 22 consists of micro-faulted beds of micrite (mudstone) to pelmicrite (wackestone). These structures are important to note because they have not previously been documented in strata at the Tlayua Quarry.

Paleosols

Two calcareous clay layers are present in the Tlayua quarry. Both layers are 10-12 cm thick, and occur at 14 and 17 m above the base of the section. A thin section of sample18a has a clay microstructure characterized by cross-striated birefringence fabric (b-fabric) to grano-striated b-fabric (Stoops 2003) and abundant clasts of foraminiferal biomicrites (Figure 4E-F).

Isotopic analysis

Over 300 carbonate microsamples were analyzed for carbon and oxygen isotopic composition. Most of these microsamples were extracted from micritic matrix to characterize the diagenetic trends in carbon-oxygen isotope space encoded

by early diagenesis. To rule out possible overprinting effects by later diagenetic fluids, calcite veins and calcite spar-filled voids were also sampled.

The majority of the micro samples (302) were taken from micritic domains and 22 micro samples were drilled from sparry calcite (13 from veins, 9 from voids). Overall, the isotopic data from micritic samples are widely scattered in $\delta^{13}C$-$\delta^{18}O$ crossplots with an overall positive covariance (covariance =1.94) (Figure 5). $\delta^{18}O$ values range from -11.67‰ to -0.39‰, and $\delta^{13}C$ values range from -8.45‰ to -0.89‰. Sparry domains in veins and void-fills are also highly variable and generally more negative with $\delta^{18}O$ values ranging from -12.62‰ to -7.37‰, and $\delta^{13}C$ values ranging from -9.09‰ to -3.31‰. At least five MCLs were identified and described below.

INTERPRETATION

Our petrographic and stable isotope analysis confirms the freshwater-influenced shallow-water coastal lagoon environments for strata in the Tlayua Quarry. The overall sequence represented at the Tlayua Quarry is specifically interpreted to range from subtidal lagoon deposits to the supratidal environments of a tidal flat (Figure 6). Clay accumulations record pedogenesis and indicate sustained exposure of the strata to meteoric fluids that led to early diagenetic stabilization of micritic carbonate. This interpretation is based on a number of observations indicative of these environments.

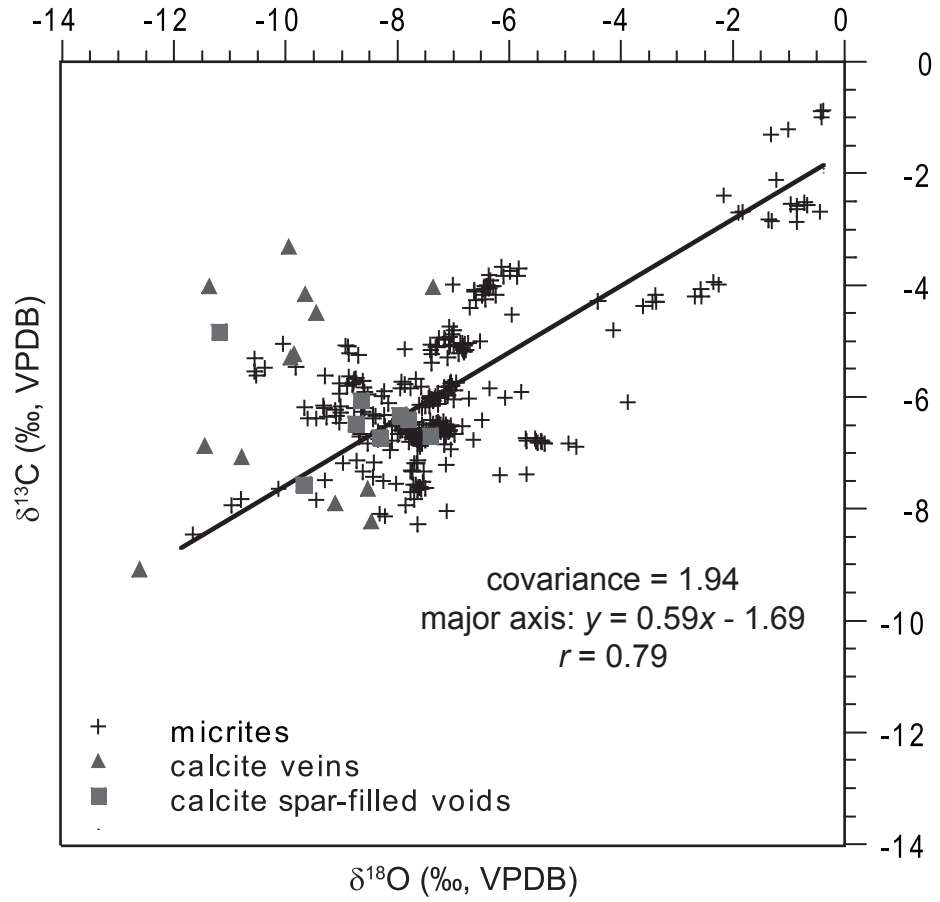

FIGURE 5—$\delta^{18}O$ vs. $\delta^{13}C$ crossplot of all isotopic data from the Tlayua Quarry. Line indicates the major axis of a 95% confidence ellipse for all the micritic data. Overall the micritic data is covariant (covariance = 1.94).

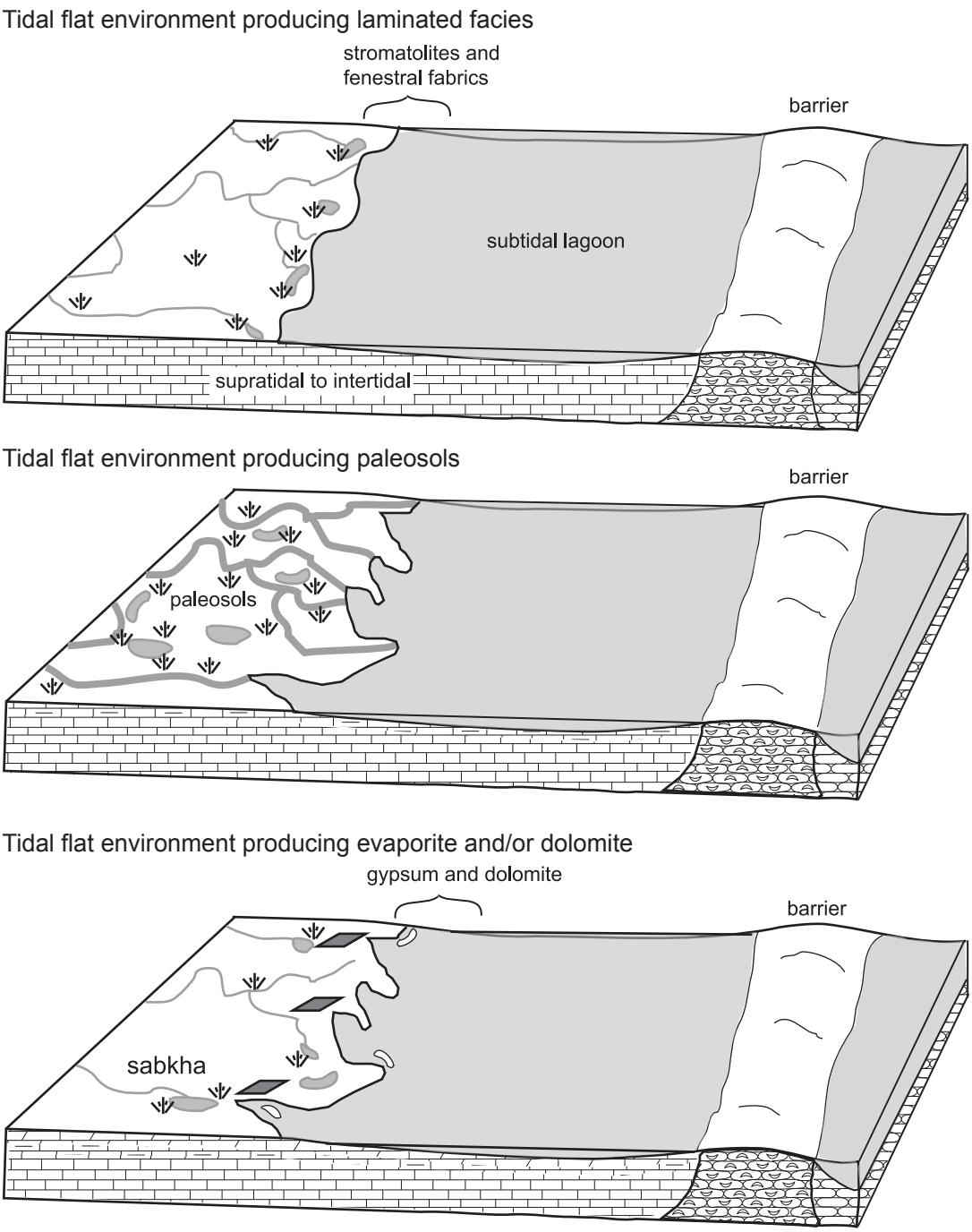

FIGURE 6—Schematic diagrams (not to scale) showing interpreted depositional environments for the Tlayua Quarry. Tidal flat environments existing behind a theoretical barrier as described in Applegate et al. (2006). Intertidal to supratidal conditions produced laminated facies. Paleosols developed on exposed surfaces in siliciclastic muds transported by fluvial discharge. Dolomite and evaporite facies likely occurred during more arid conditions in sabkha paleoenvironments.

Supratidal and Intertidal Environments

The majority of the structures observed in the Tlayua Quarry are indicative of supratidal to intertidal conditions. Many of the structures found in supratidal conditions can also form in the intertidal zone. Structures diagnostic of supratidal conditions (e.g., Shinn, 1983) that are present in thin section include cyanobacterial filaments, stromatolitic structures, fenestral fabrics, soil microstructure, and gypsum molds (Figures 3 and 4).

A sustained period (i.e., tens to thousands of years) of emergence consistent with supratidal conditions is indicated by the presence of paleosols. Cross-striated to grano-striated b-fabrics in sample 18A (Figure 4E-F) suggest soil development (Retallack, 1997). The clay accumulation was likely the result of fluvial influx, and subsequent, wetting and drying caused shrinking and swelling resulting in the cross striated b-fabrics (Brewer, 1964; Stoops 2003).

Gypsum molds are also indicative supratidal conditions and occur in samples 12 and 22. Gypsum suggests more arid sabkha-like conditions. It is also important to note that the gypsum molds retain their original euhedral crystal margins, and are not collapsed, suggesting gypsum dissolution after early calcite cementation of the surrounding micritic matrix.

Evidence for lower intertidal zone includes lenses and thin beds of marine benthic foraminifera (e.g., sample 4), ostracodes (e.g., sample 17), and bioturbation including vertical burrows (e.g., sample 7). Fining upward biopelsparites (packstones to wackestones) layers are likely the result of storm deposition.

Subtidal Environments

Petrographic evidence for subtidal conditions includes massive micritic limestone (thoroughly bioturbated) (sample 26). The primary evidence for subtidal conditions is the variety of marine fauna found in the quarry described by previous authors. In addition to the marine fish found at the quarry, a diverse open marine fauna has been described, including stenohaline organisms such as corals and echinoderms (Applegate et al., 2006), suggesting that in portions of the section, strata were deposited without major fluctuations in salinity (Heckel, 1972).

Isotope Geochemistry

Despite the wide spread in carbon and oxygen values of the micritic components, the isotopic evidence indicates that most of the strata in the Tlayua quarry were diagenetically stabilized in tidal flat environments dominated by early meteoric (freshwater) diagenesis. Four of the hand samples (samples 9, 17, 18a, and 27) and two laminae in sample 12 display unique meteoric calcite lines (Figure 7A). In addition to MCLs, linear trends with positive slopes in which carbon and oxygen isotopic values trend along a covariant line, occur in samples 4r, 13, two lamina in sample 12, combined samples 17 and 18a, and sample 22 (Figure 7B). Such trends have been described as "positive linear covariant trends" (PLCTs) (Sorensen et al., 2002; Davis et al., 2004; Ludvigson et al., 2004; Ufnar et al., 2008). These patterns are interpreted as evaporative trends, in which oxygen values were progressively enriched by preferential evaporation of ^{16}O-bearing water molecules. The carbon isotopes vary independently of the oxygen isotopes and probably reflect kinetic

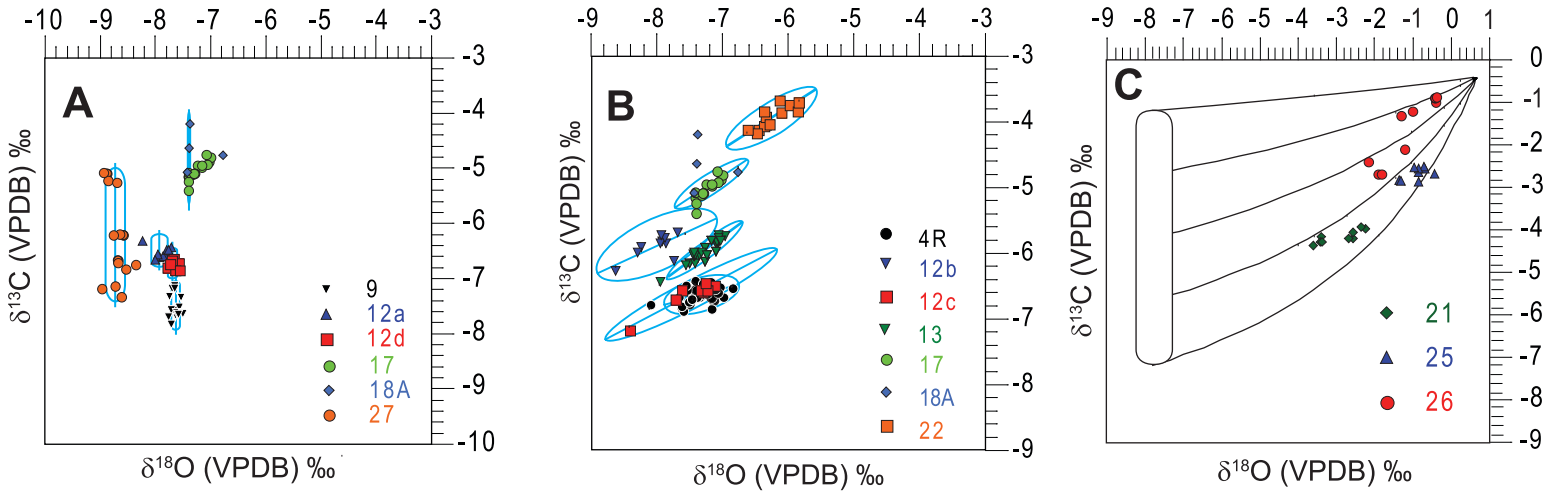

FIGURE 7—$\delta^{18}O$ vs. $\delta^{13}C$ crossplots for diagenetic trends interpreted as meteoric calcite lines (MCLs), positive linear covariant trends (PLCTs) and marine-freshwater mixing. (A) Meteoric calcite lines. The averages of the MCLs are given by the vertical blue lines, with the standard deviation represented by the width of the rounded rectangles. (B) Data interpreted as PLCTs. The ellipses are the 95% confidence ellipses. Values for covariance and the coefficients and constants for the major axes of the 95% confidence ellipse are summarized in Table 2. (C) Data interpreted to have resulted from marine-freshwater mixing and modeled mixing curves. Data fall within hyperbolic arrays calculated using a marine fluid $\delta^{18}O$ of 3.50‰ (VSMOW) and a freshwater $\delta^{18}O$ of -5.46‰ (VSMOW) estimated from the average values of the MCLs. Curvature of the hyperbolic trends is determined by the amount and isotopic composition of dissolved inorganic carbon (DIC) in the respective paleogroundwaters. End member seawater DIC is assumed to be 2.5 mmol/L with a $\delta^{13}C$ of -2.25 (VPDB). The DIC of freshwater end members ranges from 3.0 to 7.0 mmol/L, and $\delta^{13}C$ values from -3.00 ‰ to -9.00‰ (VPDB). Temperature was held constant at 29°C. The rounded rectangle represents the average MCL value (-7.78 ± 0.56 ‰ VPDB).

effects from degassing of dissolved CO_2 originally derived from the oxidation of organic matter. When evaluated with coeval MCLs, the PLCT can potentially indicate the extent of evaporative enrichment in the vadose zone during early diagenetic stabilization.

Meteoric Calcite Lines

The average $\delta^{18}O$ values of meteoric calcite lines for each sample that produced these trends are summarized in Table 1. A meteoric calcite line generated from the data from sample 9 is consistent with the petrographic evidence for fenestral fabric indicating early cementation in upper intertidal to supratidal conditions.

Within sample 12, four different laminae were microsampled, and four distinct populations of isotopic data were produced. The lowest (12a in Figure 7A) and uppermost laminae (12d in Figure 7A) sampled produced unique clusters of invariant $\delta^{18}O$ and $\delta^{13}C$ data. Two laminae between 12a and 12d (12b and 12c in Figure 7B) display positive linear covariant trends. This rock sample clearly demonstrates the complexity and fine spatial scale of the deposition and early meteoric diagenesis that characterizes these strata.

When plotted together, data from samples 17 and 18A (paleosol horizon) are define a meteoric calcite line. In addition to the meteoric calcite line, a PLCT is also produced by the data from 17 and 18a (Figure 7). We interpret that samples 17 and 18a were stabilized in the same phreatic-vadose paleogroundwater system.

TABLE 1. Meteoric Calcite Lines

Sample	Average $\delta^{18}O$	Standard deviation
9	–7.66‰	0.08‰
12a	–7.88‰	0.16‰
12d	-7.67‰	0.08‰
17/18A	–7.40‰	0.02‰
27	–8.71‰	0.17‰

Data from sample 27 also produce a meteoric calcite line, though it is somewhat more variable and is characterized by more negative $\delta^{18}O$ values (-8.71‰ ±0.17‰). This sample is characterized by crinkly-laminated fabric, associated with the presence of algal mats in supratidal conditions. These environments are ideal for early cementation by meteoric waters.

Positive Linear Covariant Trends

Data from samples that produce PLCTs are summarized in Table 2, which contains the covariance as well as the coefficients and constants for the line of the major axis of the 95% confidence ellipse. Like the samples that produce MCLs, the samples that produce PLCTs show petrographic features indicative of tidal flat depositional environments. These environments were influenced by infiltrating meteoric water and evaporative losses to the atmosphere. The determination of whether isotopic compositions from a sample define a MCL or a PLCT was probably governed by whether crystallization occurred in a shallow phreatic (MCL) or vadose (PLCT) paleogroundwater.

Marine Water-Freshwater Mixing

Isotopic data in samples 21, 25, and 26 have $\delta^{13}C$ and $\delta^{18}O$ values that are significantly heavier than those defining MCLs and PLCTs, and are much closer to expected marine VPDB standard values. Their data can be modeled as covariant trends in carbon and oxygen isotope space that are arrayed along hyperbolic curves (Figure 7C), which suggests mixing of marine and meteoric fluids (Lohmann, 1988).

Table 2. Positive Linear Covariant Trends

Sample	Covariance	Slope	Y-intercept	R
4R	0.01	0.27	– 4.66	0.43
12b	0.03	0.49	– 2.01	0.81
12c	0.08	0.52	– 2.71	0.94
13	0.03	0.74	– 0.57	0.93
17/18A	0.02	0.68	– 0.18	0.88
22	0.03	0.62	– 0.04	0.81

Specific hyperbolic trends result from differences in the concentrations of dissolved inorganic carbon in each end-member fluid (Lohmann, 1988). Samples 21 and 25 contain dolomitized micrite, which may also be consistent with mixing zone dolomitization (Shinn, 1983). Sample 26 is characterized by values that are closest to marine values. Oxygen isotopic values range from -2.17‰ to -0.39‰, and carbon isotopic values range from -2.69‰ to -1.00‰. These values were generated from a layer containing abundant gastropods, and are probably indicative of restricted marine conditions. These more marine values were produced from strata in the upper bedded facies. These facies accumulated in environments that were more influenced by seawater than those of underlying units, and their depositional waters were also likely modified by evaporation. The depositional environment is still interpreted to have been tidal flats, but the freshwater influence that dominated lower in the section is muted in the upper portion, possibly due to more arid, sabkha-like conditions.

DISCUSSION

Implications for Depositional Environment

Identification of the depositional environments for the Tlayua Quarry strata has been the focus of many investigations since its discovery. It was important for this study to correctly identify the depositional environment in order to place the isotope data in an appropriate context for interpreting isotopic patterns, particularly since Kashiyama et al. (2004) raised doubts about the shallow marginal marine to coastal lagoon depositional environments postulated by previous authors. The bulk of

the isotopic and petrographic data presented here are consistent with the shallow marginal marine to coastal lagoon interpretation for the Tlayua Quarry deposits (Malpica-Cruz et al., 1989; Pantoja-Alor, 1992; Espinosa-Arrubarrena and Applegate, 1996; Applegate et al., 2006). Specifically, we identify the depositional environment as a tidal flat that included subtidal to supratidal subenvironments. Tidal flats occur in shallow marginal marine conditions, and coastal lagoons are common in tidal flat environments. We reject the open marine hypothesis suggested by Kashiyama et al. (2004), however, the burial and/or tectonic diagenetic overprinting noted by Kashiyama et al. (2004) is recorded by some microfabrics and isotopic data. Kashiyama et al. (2004) suggested that these features were misinterpreted by others as evidence for shallow marine deposition. Stylolites are indeed abundant in thin section, but under petrographic examination they can be easily distinguished from the stromatolitic features. We found ample field, petrographic, and geochemical evidence of freshwater influence, exposure, and alteration by meteoric fluids. In addition, the calcite vein and calcite spar void fills were dominated by the lightest $\delta^{18}O$ values, and a number of micritic samples had similar light values with much greater ranges of $\delta^{18}O$ variability (samples 1-4, 5-8, 10, 11, 14-16, 19, 20, and 22-24), suggesting that some of the micritic values were influenced by later diagenetic fluids (Lohmann, 1988). Despite the late diagenetic overprinting on the isotopic composition of many of the micrites, well-defined MCLs and PLCTs are easy to distinguish in some of the horizons (Figure 7). The abundant red clays were likely the result of transportion and discharge from fluvial runoff. A detailed spectral

analysis of the microfacies at the Tlayua Quarry conducted by Kashiyama et al. (2004) reported evidence of Milankovitch cyclicity, with an interpretation of a precessional cycle that was modified due to a double-monsoon effect. They argued that this effect was due to the geographic position of the Tlayua Quarry during the Early Cretaceous between the northern and southern American continents. Such monsoon effects would be a logical mechanism to explain delivery of the red clay sediments into the Tlayua shallow coastal lagoon. Moreover, pedogenesis in the red clays clearly indicates that these are near-shore deposits that were modified by terrestrial environments during minor sea-level fluctuations.

Estimates of Groundwater $\delta^{18}O$ Values

The early meteoric diagenetic signals identified in the Tlayua Quarry deposits allow us to estimate the composition of meteoric water, which is equivalent to local precipitation (Lohmann, 1988) during the deposition of the Middle Member of the Tlayua Formation. We utilize the second-order polynomial regression generated by Ufnar et al. (2002) from the latitudinal temperature gradient presented by Spicer and Corfield (1992) and based on fossil leaf physiognomy data of Wolfe and Upchurch (1987):

$$t = 30.25 - 0.2025 \bullet l - 0.0006 \bullet l^2,$$

where t is temperature in degrees Celsius and l is latitude. There are no independent paleotemperature data from the Tlayua Quarry site. Thus, we utilized the terrestrial temperature gradient based of fossil leaf data rather than other temperature gradients because plants are directly in contact with atmospheric conditions and because this

data set provides purely empirical data that are independent of modeled latitudinal temperature gradients. As shown by Spicer and Corfield (1992), the empirical Cretaceous terrestrial and sea-surface temperature gradients are not significantly different. In addition, the temperature estimate compares well to modeled mean annual temperatures from 18°N t o 19°N at 2 times modern pCO_2 levels (Poulsen et al., 2007).

The Tlayua Quarry site is estimated to have been located between 18 to 19° N during the Cretaceous, based on paleogeographic reconstructions (e.g., Meschede and Frisch, 1998) and paleomagnetic data (Benammi et al., 2006). At these latitudes, the leaf physiognomy-based mean annual temperature estimate is approximately 26°C. The calcite-water ^{18}O fractionation factor (α) calculated from the relationship reported by Friedman and O'Neil (1977) is used with the estimated temperature to determine the $\delta^{18}O$ values of the meteoric fluids at Tlayua Quarry. The isotopic compositions of the meteoric waters that produced the MCLs in sample 9, the two laminae in sample12, combined samples17 and 18a, and sample 27 is estimated at -5.34‰, -5.57‰, -5.36‰, -5.09‰, and -6.40‰ (VSMOW) respectively.

The data generated in this study produce Cretaceous tropical groundwater $\delta^{18}O$ values that improve latitudinal groundwater $\delta^{18}O$ trends (Figure 8) which have been estimated from Cretaceous pedogenic siderite (Ufnar et al., 2002; Suarez et al., 2007) and pedogenic calcite (Ludvigson et al., 2004; Ufnar et al., 2005). These new tropical-subtropical data (this study and Suarez et al., 2007) indicate lighter $\delta^{18}O$ compositions than values produced by projecting the initial mid-latitude to polar trend

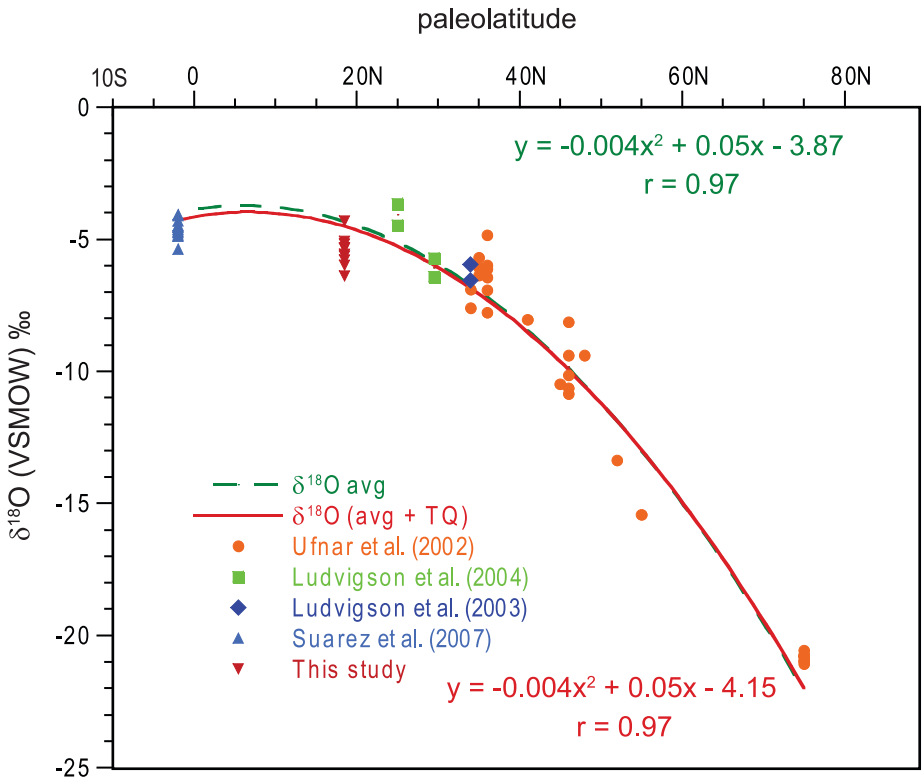

FIGURE 8—Latitudinal gradient for $\delta^{18}O$ of mid-Cretaceous meteoric water estimated from the isotopic composition of pedogenic or early diagenetic carbonates (siderite or calcite). Each symbol represents the oxygen isotopic composition of meteoric water calculated from the average value of a MCL or a MSL at a given latitude. The green dashed line is a second order polynomial fit to the average estimated groundwater $\delta^{18}O$ value for each latitude based on Ufnar et al., 2002 (MSL based), Ludvigson et al., 2003 (MCL based), Ludvigson et al., 2004 (MCL based), and Suarez et al., 2007 (MSL based). The solid red line is the second order polynomial fit to all the data including the Tlayua Quarry data.

generated by Ufnar et al. (2002), which produces a meteoric water composition approximately 3‰ heavier (-2.08‰ VSMOW) than the values estimated from the Tlayua Quarry carbonates. This suggests that greater rainout effects are needed to produce the more depleted values observed in this study. Our estimates of $\delta^{18}O$, ranging from -5.09‰ to -6.40‰, however, are similar to the ~ - 4.0 to -7.0 ‰ range modeled by Poulsen et al. (2007) for this latitude.

Estimates of the Extent of Tropical Evaporation

The presence of PLCTs allow us to estimate minimum amounts of evaporation needed to produce the more enriched carbonate $\delta^{18}O$ values from ancient tidal flats in the Tlayua Quarry section, by using a simple Rayleigh distillation approach (Table 3). The $\delta^{18}O$ of meteoric groundwater for each PLCT was calculated using the most depleted calcite $\delta^{18}O$ value for each PLCT. The Rayleigh distillation approach was used to determine what fraction must be evaporated and lost to the atmosphere in order to produce the most enriched PLCT values:

$$\delta_l = (\delta_{lo} + 1000) \bullet f^{(\alpha_{l-v}-1)} - 1000,$$

where, δ_l is the final liquid isotopic composition, δ_{lo} is the isotopic composition of the initial fluid (calculated from the most depleted PLCT value), *f* is the fraction remaining, and α is the fractionation factor of liquid from vapor (Gonfiantini, 1986). For all of the PLCT trends, 8-12% of the groundwater must be evaporated to produce the most enriched values (Table 3). It should be noted that these values reflect evaporation in the vadose zone during early meteoric diagenesis of the tidal flat

Table 3. Calculation of Percent Evaporation via Rayleigh Distillation

Sample	δ_{lo}	δ_{l}	α	f	% evaporation
4R	−5.79	−4.53	1.029	0.89	11%
12b	−6.31	−5.27	1.029	0.90	10%
12c	−6.11	−4.82	1.029	0.88	12%
13	−5.64	−4.64	1.029	0.91	9%
17/18A	−5.09	−4.45	1.029	0.94	6%
22	−4.31	−3.52	1.029	0.92	8%

sediments. It is likely that even greater evaporation effects occurred during the deposition of the tidal flat sediments that contain gypsum molds. Indeed the 8-12% estimate of evaporation may be an underestimate as Ufnar et al. (2008) recently demonstrated that the PLCT offset from the MCL, and thus the slope the PLCT, are significantly controlled by the calcite saturation and pCO_2 of the precipitating fluid. For fluids that degass quickly, calcite precipitation can occur before the fluid undergoes significant evaporation and before the fluid can become extremely enriched in ^{18}O, and thus calcite might not record the full extent of evaporative enrichment (i.e. the PLCT). In general, our findings are consistent with the modeling study on Cretaceous (Wealden) climates by Haywood et al. (2004) arguing for development of evaporation deficits despite large increases in zonal Cretaceous precipitation.

CONCLUSIONS

Petrographic and isotopic data from the Tlayua Formation at the Tlayua Quarry indicate that the quarry strata were deposited in a tidal flat-shallow lagoon system that was often subject to freshwater influx from precipitation and fresh groundwater discharge. Evidence for tidal flat - shallow lagoon systems includes fenestral fabrics, gypsum molds, cyanobacterial and stromatolitic structures, a fauna that include a mixture of marine organisms with terrestrial and freshwater aquatic fauna, and isotopic signatures characteristic of early meteoric diagenesis. Paleosols and their matrix micromorphology are clear indicators of subaerial exposure at

Tlayua, and the associated red clay accumulations indicate frequent influence of fluvial deposition during the monsoon months.

MCLs and PLCTs that are unique to meteoric environments yield an estimate average $\delta^{18}O_{(VSMOW)}$ of early meteoric diagenetic fluids of -5.46‰ ± 0.56‰ and a minimum estimate for evaporative loss of ground water at 8-12%. These estimates for precipitation isotopic composition are consistent with the geometry of modern latitudinal trends that show a plateau in the subtropical regions. The trends generated by the limited mid- to high-latitude data used in the model of Ufnar et al. (2002) project much heavier precipitation $\delta^{18}O$ values in the subtropical and tropical regions. The data presented here imply that the earlier model might have underestimated tropical to subtropical precipitation and evaporation fluxes due to the inaccurate precipitation $\delta^{18}O$ value extrapolated from the high latitude data. The lighter values estimated in this paper would require greater rainout to cause the depletion of $\delta^{18}O$ of meteoric water and possibly much higher evaporation rates to sustain the aridity that prevailed in the region as suggested by the presence of evaporite minerals. Estimates of the impact on evaporation fluxes and latent heat transport calculations (Ufnar et al., 2004) require that model runs be carried out with the constraints afforded by the Tlayua data and other low-latitude data that are being generated by our group (e.g. Suarez et al., 2007).

Our results suggest that oxygen isotopic compositions of pedogenic carbonates and early diagenetic carbonate cements provide reliable paleoclimatic data with which to calibrate empirical and numerical models used to simulate ancient and

future climate. Moreover, it is imperative that we expand empirical data acquisition into the southern hemisphere where Cretaceous data are nearly nonexistent, and modeled precipitation and evaporation values are not constrained.

REFERENCES

Alencáster, G., 1973, Una nueva especie de *Toucasia* en el Cretácico medio de los estados de Oaxaca y Puebla: Paleontología Mexicana, v. 36, p. 1-20.

Alvarado-Ortega, J., Espinosa-Arrubarrena, L., Blanco, A., Vega, F.J., Benami, M., and Briggs, D.E.G., 2007, Exceptional preservation of soft tissues in Cretaceous fishes from the Tlayua Quarry, Central Mexico: PALAIOS, v. 22, p. 682-685.

Applegate, S. P., Espinosa-Arrubarrena, L., Alvarado-Ortega, J., Benammi, M., 2006, Revision of recent investigations in the Tlayua Quarry, *in* Vega, F. J., Nyborg, T.G., Perrilliat, M.C., Montellano-Ballesteros, M., Cevallos-Ferriz, S.R.S., and Quiroz-Barroso, S.A., ed., Studies on Mexican Paleontology: Topics in Geobiology: Dordrecht, Springer, p. 275-304.

Banner, J. L., and Hanson, G. N., 1990, Calculation of simultaneous isotopic and trace-element variations during water-rock interaction with applications to carbonate diagenesis. Geochimica et Cosmochimica Acta 54, 3123-3137.

Barron, E. J., Hay, W.W., Thompson, S., 1989, The hydrologic cycle: A major variable during earth history: Palaeogeography, Palaeoclimatology, Palaeoecology, v. 75, no. 3, p. 157-174.

Benammi, M., Alvarado-Ortega, J., Urrutia-Fucugauchi, J. , 2006, Magnetostratigraphy of the Lower Cretaceous strata in Tlayua Quarry, Tepexi de Rodríguez, state of Puebla, Mexico: Earth Planets Space, v. 58, p. 1295-1302.

Brewer, R., 1964, Fabric and Mineral Analysis of Soils: New York, John Wiley and Sons, 470 p.

Chahine, M.T., 1992, The hydrologic cycle and its influence on climate: Nature, v. 359, p. 373-380.

Davis, J. M., Ludvigson, G.A., Ufnar, D.F., Atchley, S., González, L.A., Brenner, R.L., and Witzke, B.J., 2004, Diagenetic analysis of a subaerial exposure surface from the Cretaceous (Albian) Walnut Formation, Central Texas: Geological Society of America Abstracts with Programs, v. 36, p. 75.

Dunham, R. J., 1962, Classification of carbonate rocks according to their depositional texture, *in* Ham, W. E., ed., Classification of carbonate rocks-a symposium: Tulsa, American Association of Petroleum Geologists Memoir 1, p. 108-121.

Espinosa-Arrubarena, L., and Applegate, S.P., 1996, A paleoecological model of the vertebrate bearing beds in the Tlayua Quarries, near Tepexi de Rodríguez, Puebla, Mexico, *in* Arratia, G., and Viohl, G., eds., Mesozoic Fishes - Systematics and Paleoecology: Munich, Verlag, p. 539-550.

Friedman, I., and O'Neil, J.R., 1977, Compilation of stable isotope fractionation factors of geochemical interest, *in* Fleisher, N. ed., Data of geochemistry. USGS Professional Paper 440-KK: Washington, D.C., 110 p.

Folk, R. L., 1962, Spectral subdivision of limestone types, *in* Ham, W. E., ed., Classification of carbonate rocks-a symposium: Tulsa, American Association of Petroleum Geologists Memoir 1, p. 62-84.

Gonfiantini, R., 1986, Environmental isotopes in lake studies, *in* Fritz, P. a. F., J.-Ch., ed., Handbook of Environmental Isotope Geochemistry, Vol. 2, The Terrestrial Environment: Amsterdam, Elsevier, p. 113-168.

Graversen, R. G., Mauritsen, T., Tjernström, M., Källen, E., and Svensson, G., 2008, Vertical structure of recent arctic warming: Nature, v. 541, p. 53-57.

Hammer, Ø., Harper, D. A. T., and Ryan, P. D., 2008, PAST-Paleontological Statistics, version 1.79.

Haywood, A.M., Valdes, P.J., and Markwick, P.J., 2004, Cretaceous (Wealden) climates: a modeling perspective: Cretaceous Research, v. 25, p. 303-311.

Heckel, P.H., 1972, Recognition of ancient shallow marine environments: *in* Recognition of Ancient Sedimentary Environments, a symposium: J. K. Rigby and W.K. Hamblin, eds. Society of Econ. Paleontologists and Mineralogists Spec. Pub. 16, p. 226-286.

Kashiyama, Y., Fastovsky, D.E., Rutherford, S., King, J., and Montellano, M., 2004, Genesis of a locality of exceptional fossil preservation: paleoenvironments of Tepexi de Rodríguez (mid-Cretaceous, Puebla, Mexico): Cretaceous Research, v. 25, p. 153-177.

Lohmann, K. C, 1988, Geochemical patterns of meteoric diagenetic systems and their application to studies of paleokarst, *in* James, N. P., and Choquette, P.W., ed., Paleokarst: New York, Springer, p. 58-80.

Ludvigson, G., González, L.A., Metzger, R.A., Witzke, B.J., Brenner, R.L., Murillo, A.P., and White, T.S., 1998, Meteoric sphaerosiderite lines and their use for paleohydrology and paleoclimatology: Geology, v. 26, no. 11, p. 1039-1042.

Ludvigson, G.A., Ufnar, D.F., González, L.A., Carpenter, S. J., Witzke, B. J., Brenner, R. L., and Davis, J., 2004, Terrestrial paleoclimatology of the Mid-Cretaceous greenhouse; I, Cross-calibration of pedogenic siderite & calcite $\delta^{18}O$ proxies at the Hadley Cell boundary.; Geological Society of America, 2004 annual meeting: Abstracts with Programs Geological Society of America, v. 36, no. 5, p. 305.

Malpica-Cruz, V. M., Pantoja-Alor, J., and Galguera-Rosas, G., 1989, Microfacies de la Cantera Tlayua, Puebla, Mexico: Primer Simposio sobre Geología Regional de México, v. 3, p. 53-56.

Martill, D., 1989, A new Solnhofen in Mexico: Geology Today, v. 5, p. 25-28.

Meschede, M., and Frisch, W., 1998, A plate-tectonic model for the Mesozoic and Early Cenozoic history of the Caribbean plate: Tectonophysics, v. 296, p. 269-291.

Pantoja-Alor, J., 1992, Geología y paleoambientes de la Cantera Tlayua, Tepexi de Rodríguez, estado de Puebla: Revista - Instituto de Geología, v. 9, p. 156-169.

Poulsen, C. J., Pollard, D., and White, T.S., 2007, General circulation model simulation of the $\delta^{18}O$ content of continental precipitation in the middle Cretaceous: a model-proxy comparison: Geology, v. 35, p. 199-202.

Retallack, G. J., 1997, A Colour Guide to Paleosols: New York, Wiley, 175 p.

Reynoso, V. H., 1997, A "beaded" sphenodontian (Diapsida: Lepidosauria) from the Early Cretaceous of central Mexico: Journal of Vertebrate Paleontology, v. 17, p. 52-59.

-, 2000, An unusual aquatic sphenodontian (Reptilia: Diapsida) from Tlayua Formation (Albian), Central México: Journal of Paleontology, v. 74, p. 133-148.

-., 2006, Research on fossil amphibians and reptiles in Mexico from 1869 to early 2004 (including marine forms, but excluding pterosaurs, dinosaurs, and obviously birds), *in* Vega, F. J., Nyborg, T.G., Perrilliat, M.C., Montellano-Ballesteros, M., Cevallos-Ferriz, S.R.S., and Quiroz-Barroso, S.A., ed., Studies on Mexican Paleontology Dordrecht, Springer, p. 209-226.

Shinn, E. A., 1983, Tidal flat environment, *in* Scholle, P. A., Bebout, D.G., Moore, C.H., ed., Carbonate depositional environments: Tulsa, American Association of Petroleum Geologists, p. 171-210.

Sokal, R. R., and, and Rohlf, F. J., 1995, Biometry: The Principals and Practice of Statistics in Biological Research: New York, W. H. Freeman and Company, 887 p.

Sorensen, A. C., Ludvigson, G.A., González, L.A., Joeckel, R.M., and Kirkland, J.I., 2002, Petrography and diagenesis of palustrine carbonate beds in the Early Cretaceous Cedar Mountain Formation, Eastern Utah: Geological Society of America Abstracts with Programs, v. 34, no. 6, p. 17-18.

Spicer, R. A., and Corfield, R.M., 1992, A review of terrestrial and marine climates in the Cretaceous with implications for modeling the 'Greenhouse Earth': Geology Magazine, v. 2, p. 169-180.

Stoops, G., 2003, Guidelines for Analysis and Description of Soil and Regolith Thin Sections: Madison, Soil Science Society of America, 184 p.

Suarez, M., González, L. A., Ludvigson, G. A., and Davis, J., 2007, Pedogenic sphaerosiderites from the Caballos Formation (Aptian-Albian) of Colombia; a stable isotope proxy for Cretaceous paleoequatorial precipitation.; Geological Society of America, South-Central Section, 41st annual meeting: Abstracts with Programs Geological Society of America, v. 39, no. 3, p. 75.

Ufnar, D. F., González, L.A., Ludvigson, G.A., Brenner, R.L., and Witzke, B.J., 2002, The mid-Cretaceous water bearer: isotope mass balance quantification of the Albian hydrologic cycle: Palaeogeography, Palaeoclimatology, Palaeoecology, v. 188, p. 51-71.

-, 2004, Evidence for increased latent heat transport during the Cretaceous (Albian) greenhouse warming: Geology, v. 32, no. 12, p. 1049-1052.

Ufnar, D. F., Ludvigson, G. A., González, L. A., and Davis, J., 2005, Mid-Cretaceous evaporation rates estimated from pedogenic carbonate isotopic values in the

Glen Rose Formation, Texas.; Geological Society of America, 2005 annual meeting: Abstracts with Programs Geological Society of America, v. 37, no. 7, p. 357.

Ufnar D. F., Gröcke, D. R., and Beddows, P. A., 2008, Assessing pedogenic calcite stable-isotope values: Can positive linear covariant trends be used to quantify palaeo-evaporation rates?: Chemical Geology. doi: 10.1016/j.chemgeo.2008,07,022.

White, T. S., González, L. A., Ludvigson Greg, A., and Poulsen, C. J., 2001, Middle Cretaceous greenhouse hydrologic cycle of North America: Geology, v. 29, p. 363-366.

Wolfe, J. A., Upchurch, G.J.R., 1987, North American nonmarine climates and vegetation during the Late Cretaceous: Palaeogeography, Palaeoclimatology, Palaeoecology, v. 61, p. 31-77.

Zhang X., Zwiers F. W., Hegerl G. C., Lambert F. H., Gillet N. P., Soloman S, Stott P. A., and Nozawa P., 2007, Detection of human influence on twentieth-century precipitation trends: Nature, v. 448, p. 461-466.

CHAPTER 3. ESTIMATING THE OXYGEN ISOTOPIC COMPOSITION OF EQUATORIAL PRECIPITATION DURING THE MID-CRETACEOUS

ABSTRACT

Recent studies utilize the oxygen isotopic composition of pedogenic carbonates (siderite and calcite) to empirically evaluate the response of the global hydrologic cycle during the Aptian-Albian (mid-Cretaceous) greenhouse climate. Pedogenic carbonates are used as a proxy for the isotopic composition of meteoric waters in order to estimate precipitation rates in the Aptian-Albian via a mass balance model. These modeling studies have previously been limited to mid to high latitude data, thus a more extensive latitudinal data set is needed to produce a more globally constrained model.

This study provides an equatorial (~2°S paleolatitiude) data set from pedogenic sphaerosiderites of the Caballos Formation from the Upper Magdalena Valley, Colombia. In addition, macroscopic and microscopic morphological features of paleosols were used to identify ancient soil conditions. The gleyed appearance and presence of sphaerosiderites suggest soils were dominated by water-saturated conditions, with occasional incursions of marine-influenced water resulting in pyrite precipitation. Importantly, this observation constrains the sampling sites to paleoelevations near sea level. Paleosols are interpreted to have been entisols, inceptisols, and ultisols similar to soils in coastal equatorial regions of modern Colombia. Relatively invariant $\delta^{18}O$ values and more variable $\delta^{13}C$ values produce

vertical trends in $\delta^{18}O$ vs. $\delta^{13}C$ space called meteoric sphaerosiderite lines. The average oxygen isotopic composition for these trends is -4.41 ± 0.37‰ (VPDB). The average oxygen isotopic composition of meteoric waters precipitating the sphaerosiderites is estimated at -4.56 ± 0.38‰ (VSMOW). These are slightly more enriched than modern and modeled Cretaceous estimates of precipitation compositions, and suggest a significant component of source waters for air masses that produced this precipitation was ^{18}O-enriched sea water from the superheated Tethys Sea.

INTRODUCTION

The Cretaceous Period is a well-documented interval of global warmth and increased atmospheric moisture due to higher atmospheric concentrations of greenhouse gasses such as carbon dioxide (e.g., Barron and Moore, 1994; Jenkyns et al., 2004; Poulsen, 2004 and references therein). Average global temperatures are suggested to have been approximately 6°C higher than the modern global average (e.g., Barron and Moore 1994). However, while the importance of changes in the hydrologic cycle on global climate has been recognized for some time (Barron et al., 1989), only recently has it been the subject of rigorous investigations (Ludvigson et al., 1998; Hay and DeConto, 1999; White et al., 2001; Ufnar et al, 2002, 2004; Poulsen et al., 2007; Ufnar et al., 2008). Most authors hypothesize an intensified hydrologic cycle during the mid-Cretaceous, for example Barron et al. (1989)

suggested increases in global average precipitation between 18 to 22 % higher than present day.

Ufnar et al. (2002) used paleoprecipitation $\delta^{18}O$ values calculated from isotopic values of pedogenic siderites in a simple isotope mass balance model to estimate zonal precipitation rates during the mid-Cretaceous (Albian). While both general circulation model (GCM) simulations (e.g., Poulsen et al. 2007) and the Ufnar et al. (2002, 2004) mass balance models indicate increased precipitation rates in the tropics and mid-to-high latitudes, the Ufnar et al.(2002, 2004) estimates generally are higher, particularly in the mid-to-high latitudes. For example, Ufnar et al. (2002) estimated zonal precipitation rate estimates at 45° N at 7.2 mm/day, while the GENESIS GCM estimates of Poulsen et al., (2007) are 4.0 mm/day. The mass balance models simulate precipitation and evaporation fluxes during the poleward transport of atmospheric moisture from the equator, with an explicit goal of closely simulating the empirical $\delta^{18}O$ data from a wide range of paleolatitudes. The models of Ufnar et al. (2002, 2004) were constrained, however, by empirical data spanning only from 35°N to 75°N. Characterizing more complete ranges of Cretaceous latitudinal variations in $\delta^{18}O$ values of meteoric precipitation (i.e., full equator-to-pole trends) is critical for further improving the precipitation estimates in the isotope mass balance models of Ufnar et al., (2002, 2004). Suarez et al. (2009) found that tropical isotopic compositions of meteoric precipitation are much lighter than those expected from the extrapolation of the paleogeographically limited 35°N to 75°N $\delta^{18}O$ trend of Ufnar et al., (2002). Moreover, the recent addition of a water isotope module to the GENESIS

GCM, simulating water isotopic transport and fractionation effects (Poulsen et al., 2007) calls for further development of empirical $\delta^{18}O$ data sets for model calibration.

This study utilizes pedogenic sphaerosiderites from the Caballos Formation of Colombia to provide near-equatorial data expanding the range of our paleolatitudinal meteoric $\delta^{18}O$ transect from 75°N to 2°S. Pedogenic sphaerosiderites are millimeter-scale spherulitic siderite nodules that form in wetland soils of variable drainage. The oxygen and carbon isotopic compositions of sphaerosiderites from a single paleosol often form linear trends called *meteoric sphaerosiderite lines* (MSLs) defined by relatively invariant oxygen isotopic values and more variable carbon isotopic values, and are indicative of a shallow fresh groundwater system with relatively stable oxygen isotopic compositions (Ludvigson et al., 1998). These diagenetic trends can be used to determine the oxygen isotopic composition of meteoric water, in an application similar to that of *meteoric calcite lines* (Lohmann, 1988; Ludvigson et al., 1998).

GEOLOGIC SETTING

The Caballos Formation, formally described by Corrigan (1979) (as cited in Vegara 1995) is dominated by sandstones and dark gray shales with coaly laminations transitioning to marine carbonates and has been interpreted to have formed in fluvial-estuarine environments (Villamil et al., 1999; Acevedo and Pennington, 2003). The Caballos Formation was deposited in an extensional basin in what is now the Upper Magdalena River Valley region of Colombia (Figure 1). Barrero et al. (2007)

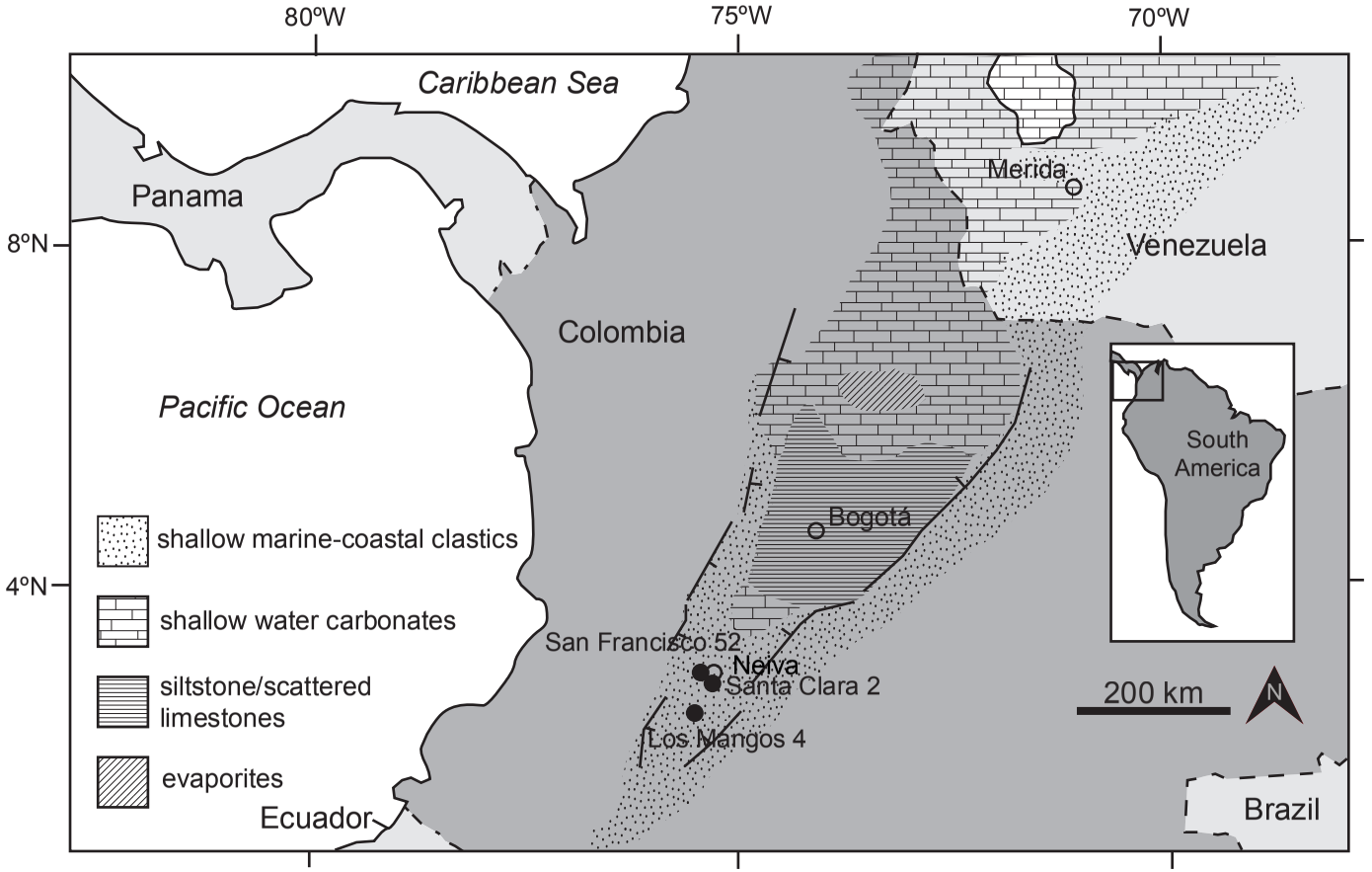

FIGURE 1—Location of cores and distribution of late Early Cretaceous facies in northwestern South America. Core penetrating Caballos Formation occur in the Neiva sub-basin in the Upper Magdalena Valley of western Colombia (modified from Villamil, et al., 1999).

described the present-day Upper Magdalena Valley Basin as a "Neogene Broken Foreland" basin that evolved from the collision-related Paleogene foreland basin (Barrero et al. 2007). Guerrero et al. (2000) proposed the use of the term Cretaceous Colombian Basin to differentiate it from the compressional regime related basins that formed during the Paleogene and dominate the modern day Upper Magdalena Valley Basin. The Cretaceous Colombian Basin extended south into northernmost Ecuador and to the north into the open marine Maracaibo Basin of Venezuela. To the west the basin was bound by the ancestral Central Cordillera and to the east the by the shorelines of the Guyana shield.

The Cretaceous rocks of northwestern to northern Colombia and northern Venezuela document an overall transgressive succession during the Aptian, with the lower to middle portions of the Caballos Formation representing the transition from fluvial deposits to marine deposits, and the upper sections documenting a regression during the Albian (Villamil, 1994; Villamil et al., 1999; Guerrero 2002). The similarity between the depositional environments of the coal-bearing Caballos Formation with those of other Aptian-Albian sphaerosiderite bearing formations (e.g. Ludvigson et al., 1998; Ufnar et al. 2001, 2002 led the authors to predict that sphaerosiderites would be present and probably abundant in portions of the Caballos Formation that were subject to subaerial exposure (interfluves) and paleosol development. Informal conversations with other researchers working in the Caballos Formation confirmed these predictions, and indicated the presence of well-developed paleosols and sphaerosiderites in the Caballos Formation.

METHODS

Core descriptions provided by the Litoteca Nacional de Colombia of the Instituto Colombiano de Petróleo (ICP), confirmed the presence of paleosols, and numerous sphaerosiderite-bearing horizons in several long drillcores penetrating the Caballos Formation in the Upper Magdalena River Valley. Sphaerosiderite-bearing horizons were sampled from seven cores housed at the Litoteca Nacional de Colombia, in Bucamaranga, Colombia (Table 1). A total of 61 resin-impregnated samples were sectioned to produce polished thin sections used for petrographic analysis and matching polished slabs for microsampling.

Thin sections were analyzed both to identify sphaerosiderites for isotopic analysis, to identify any late-diagenetic carbonates, and to generally evaluate paleosol micromorphology. Macroscopic and microscopic observations serve to provide qualitative evidence of depositional environment and soil conditions. Color was described using Munsell® Color chart. Analysis of thin sections was carried out using plane polarized and cross-polarized light on a Nikon SMZ1500 microscope fitted with an Optronics Magnafire SP digital camera and an Olympus BX51 microscope fitted with a Diagnostic Instruments SPOT Insight Firewire digital camera. In evaluating paleosol micromorphology, the fine-grained matrix (groundmass) and pedofeatures (coatings, mineral accumulations etc.) of the paleosols were described using terms from Stoops (2003). Clay minerals are described with respect to their birefringence fabric (b-fabric), which describes the pattern, orientation, and distribution of interference colors from the clay mineral crystals.

Table 1. Cores, location, and number of samples from the Caballos Formation

Core	Latitude	Longitude	# of Samples
Los Mangos 4	2º 37' 29.97"	-75º 33' 33.05"	5
Los Mangos 7	2º 37' 11.39"	-75º 32' 47.93"	9
San Francisco 2	3º 4' 58.49"	-75º 23' 10.95"	8
San Francisco 52	3º 3' 10.49"	-75º 24' 16.53"	20
Santa Clara 2	2º 58' 59.24'	-75º 21' 2.92	6
Toy 2	3º 56' 13.89"	-75º 19' 34.26"	10
Toy 3	3º 57' 33.14"	-75º 18' 27.04'	3

Through petrographic analysis, 15 horizons from 3 cores (San Francisco 52, Los Mangos 4, and Santa Clara 2) were identified that had un-oxidized or minimally oxidized sphaerosiderites that were large enough in diameter to produce 60 to 180 µg powdered samples. Analyses were carried out at the W. M. Keck Paleoenvironmental and Environmental Stable Isotope Lab at the University of Kansas, and the Paul H. Nelson Stable Isotope Laboratory at the University of Iowa. Microsamples were extracted using a microscope-mounted dental drill fitted with 3 to 500 µm diameter tungsten-carbide bits. Microsamples (n = 119) were vacuum roasted at 200°C for one hour to remove volatile contaminants. Samples were digested at 75° C with 100% phosphoric acid in a ThermoFinnigan Kiel III single sample acid dosing system connected to a dual-inlet ThermoFinnigan MAT 253 isotope ratio mass spectrometer (University of Kansas), or Finnigan MAT 252 isotope ratio mass spectrometer (University of Iowa). Precision was monitored by daily analysis of NBS-18 and NBS-19 and is better than 0.1 ‰ for both carbon and oxygen, with all carbonate data being reported relative to VPDB. Siderite oxygen isotopic values were corrected to account for the temperature-dependent fractionation factor between phosphoric acid and siderite utilizing data in Carothers et al. (1988).

RESULTS

Macroscopic Features

The three cores examined in detail generally consist of meter-scale beds of gray mudstones, sandstones, and conglomerates. Approximately 1.25 m of

stratigraphic section with sphaerosiderite-bearing horizons were sampled from the Los Mangos 4 core (Fig. 2), and 0.95 m from the Santa Clara 2 core (Fig, 3). Two sections from the San Francisco 52 core were sampled. The lower section was approximately 3.0 m long (Fig. 4), whereas the upper section was the longest section that was sampled at approximately 14 m (Fig. 5). A number of features provide evidence of depositional and soil-forming conditions.

Root Traces

Root traces are abundant in all three cores examined. These features occur as sinuous, downward-branching black traces, most likely organic, that range in diameter between a few millimeters to approximately 0.5 cm, and are as long as 8 cm. (Fig. 6A and 6B)

Burrows

Burrows are common in the three cores, but are particularly evident in the San Francisco 52 core because they are mostly preserved as distinct Fe-oxide mineral accumulations that are very dusky red (5R2.5/2) to reddish black (5R2.5/1) and have sharp boundaries with the surrounding matrix (Fig. 6B). The burrows occur as a network of interconnected burrows that most often occur in association with root traces. More discrete sand-filled burrows also occur in the San Francisco 52 and the Los Mangos 4 cores. One burrow in the San Francisco 52 core is a branching burrow approximately 1 mm in diameter (Fig. 6C). Another burrow in the Los Mangos 4 core is a vertical sand-filled burrow approximately 2.5 mm in diameter (Fig. 9A) and

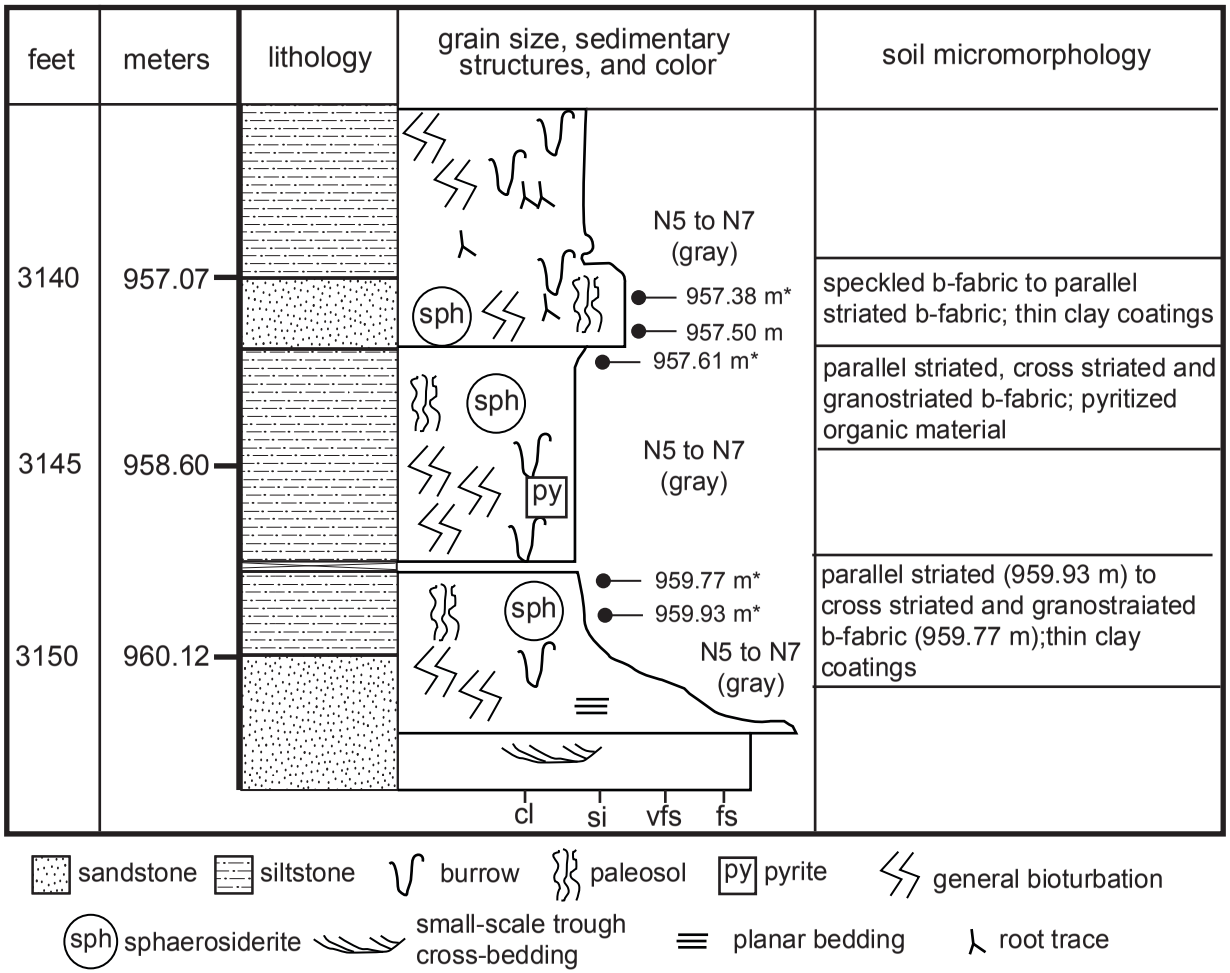

FIGURE 2—Lithology, grain size, sedimentary structures, and soil micromorphology from a section of the Los Mangos 4 core. Modified from Ecopetrol-ICP (2000a).

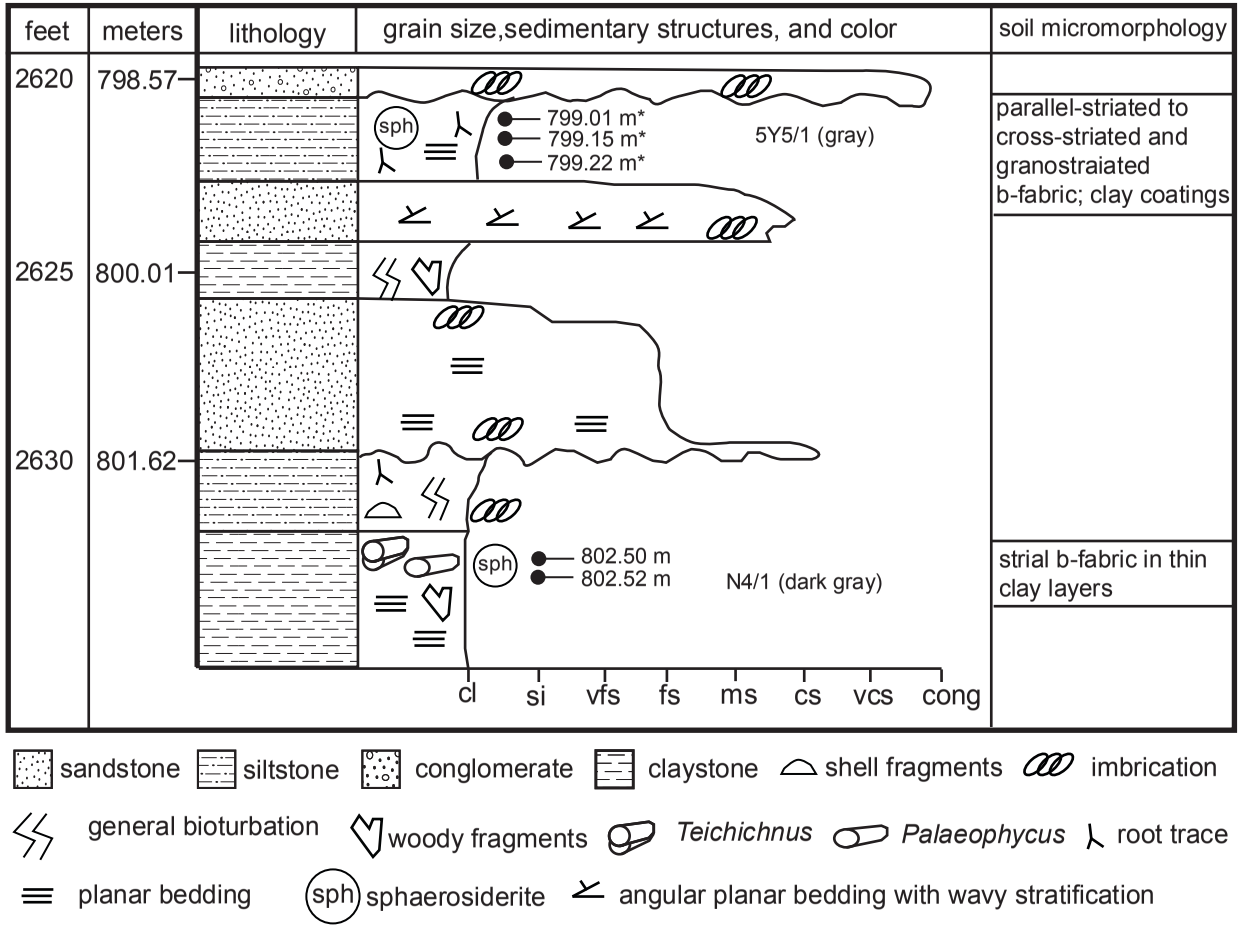

FIGURE 3—Lithology, grain size, sedimentary structures, and soil micromorphology from a section of the Santa Clara 2 core. Modified from Ecopetrol-ICP (1999).

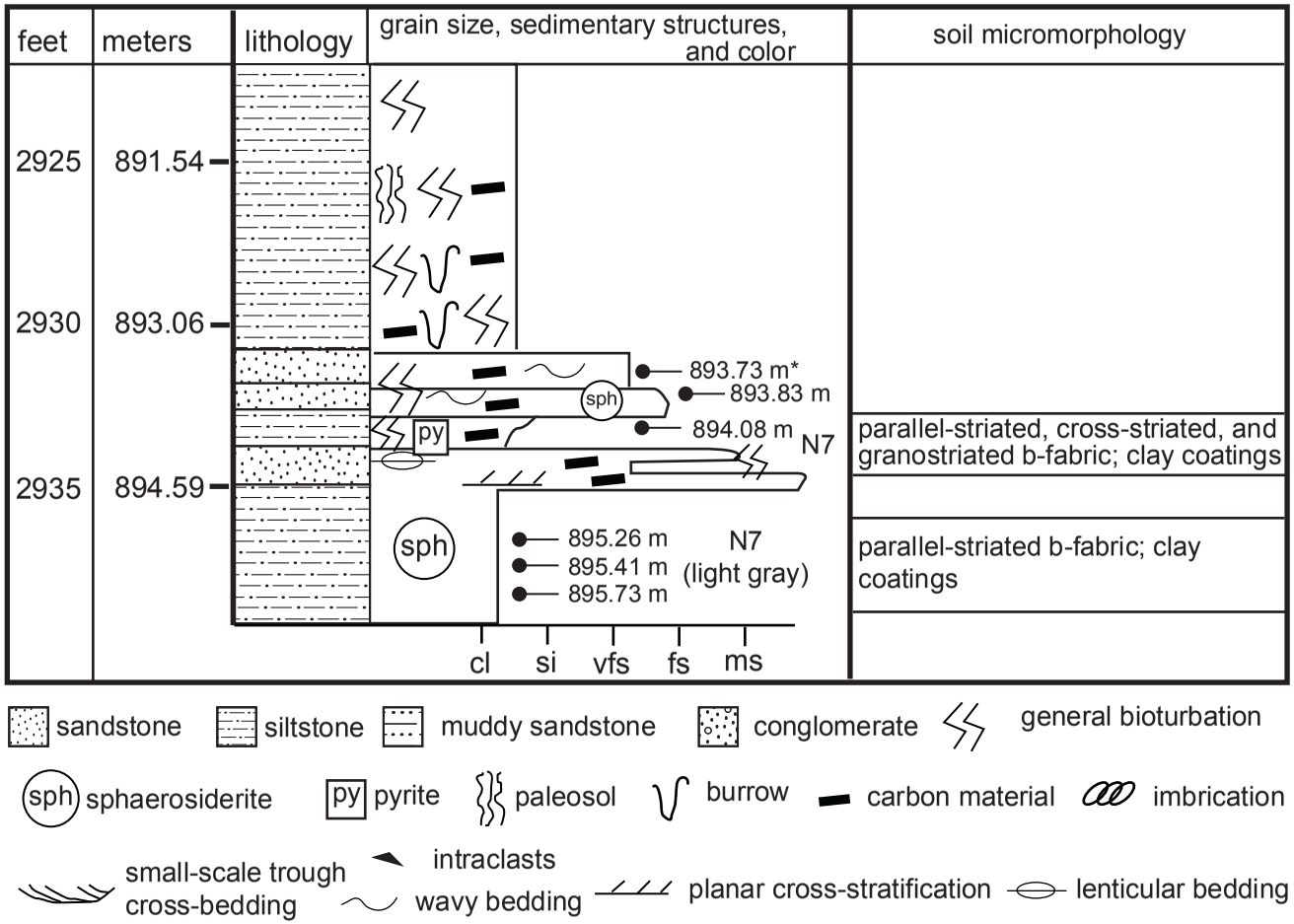

FIGURE 4—Lithology, grain size, sedimentary structures, and soil micromorphology from a section of the lower portion of the San Francisco 52 core. Modified from Ecopetrol-ICP (2000b).

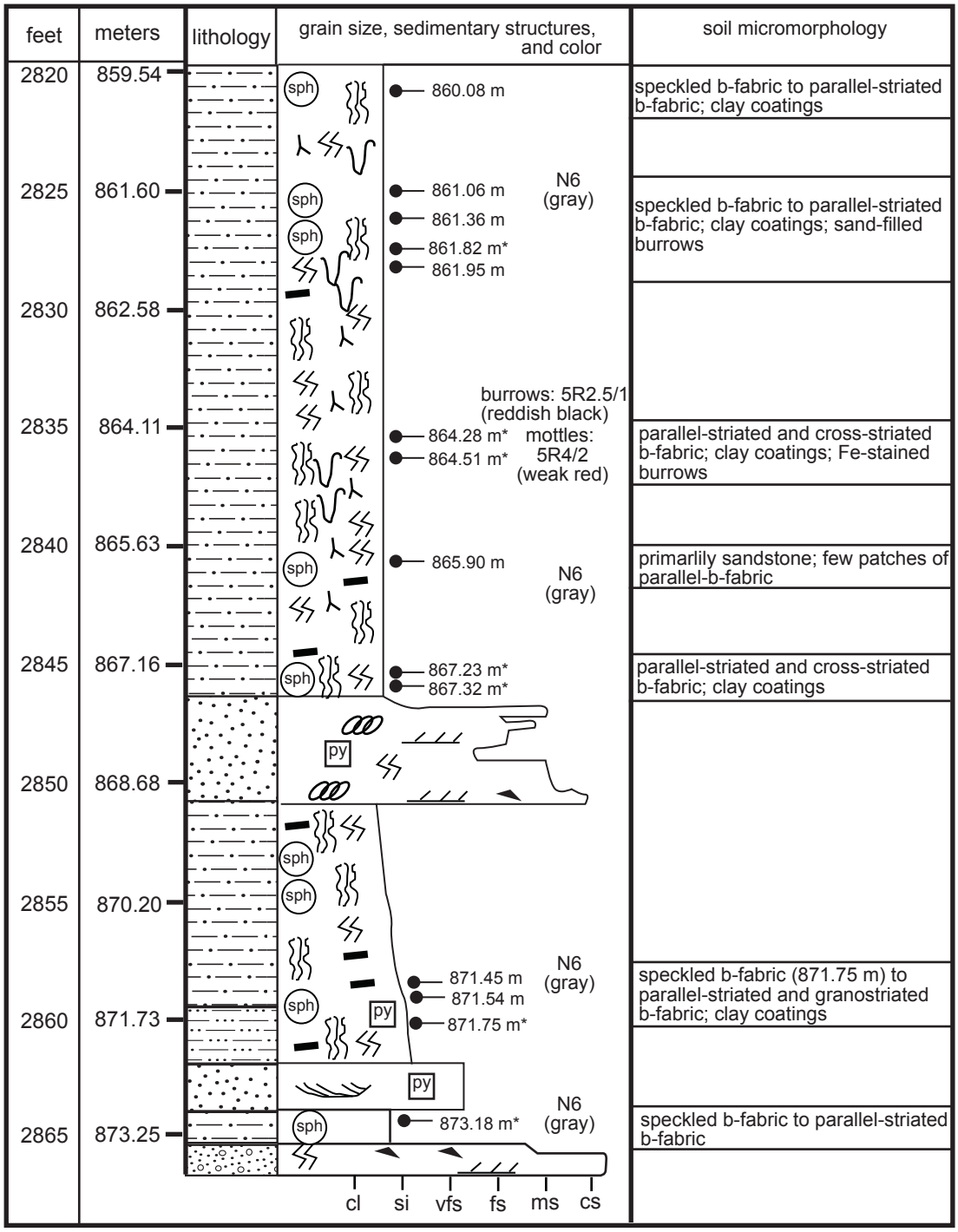

FIGURE 5—Lithology, grain size, sedimentary structures, and soil micromorphology from a section of the upper portion of the San Francisco 52 core. See Figure 4 for legend. Modified from Ecopetrol-ICP (2000b).

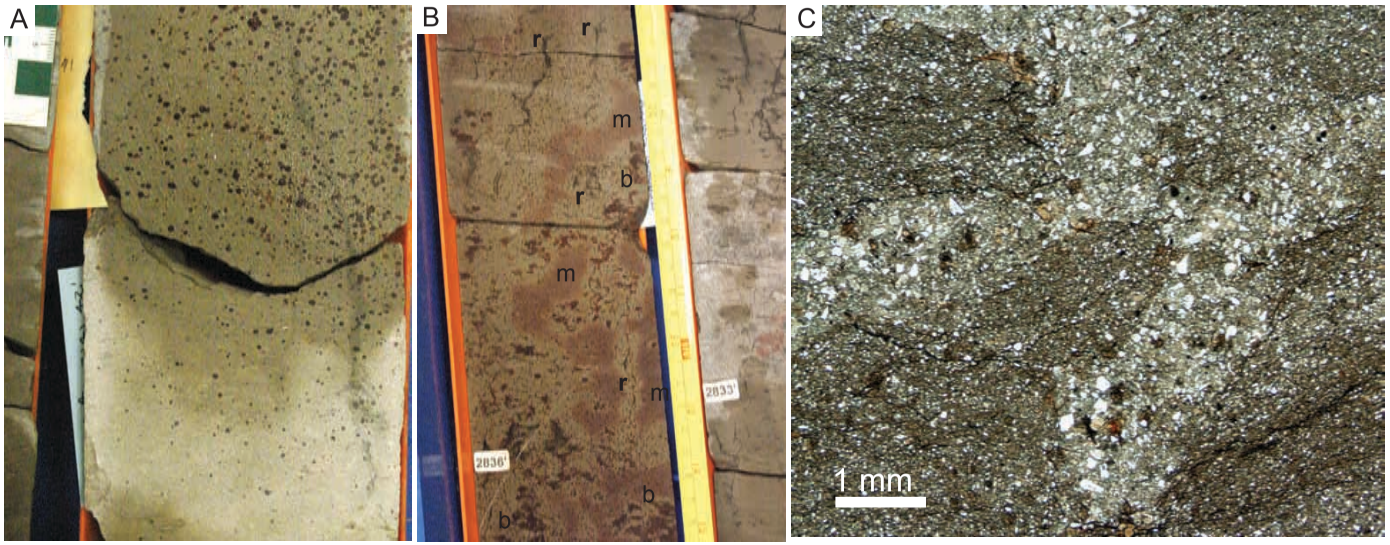

FIGURE 6—Photographs and photomicrographs of the root traces and burrows A) Photograph at 957.38m of the Los Mangos 4 core showing a root trace (black vertical feature) and millimeter scale sphaerosiderites (dark red spherical nodules). B) Photograph of the San Francisco 52 core at 864.41m showing root traces (black feature marked "r"), redoxomorphic color mottles (red patches marked "m"), and red-stained burrows (marked "b"). C) Photomicrograph of a sand-filled burrow from the San Francisco 52 core, horizon 861.06m. Scale bar = 1 mm.

10 mm long. Burrows from the Santa Clara 2 core are identified as *Paleophycus* and *Teichichnus* in ICP core logs.

Mottling

Color mottles occur primarily in the upper section of the San Francisco 52 core between about 864 m and 862 m, and are associated with the root traces and Fe-oxide preserved burrows described in the previous sections. The mottles are weak red (5R4/2) and differ from the burrows in having diffuse boundaries with the surrounding matrix (Fig. 6B).

Microscopic Features

Thin sections of hand samples collected from the three cores were examined under polarized, cross polarized, and reflected light. Groundmass and other features are described below.

Groundmass

The birefringence of the fine-grained components includes strial b-fabrics, speckled b-fabrics and various morphologies of striated b-fabrics. The Los Mangos core is characterized primarily by parallel striated to cross-striated and granostriated b-fabrics, which consist of zones or streaks of birefringent clays that form parallel, cross, or concentric patterns around grains, such as quartz grains and sphaerosiderites (Fig. 7A and 7B). In more sandy horizons (e.g., 957.38 m) fine-grained portions

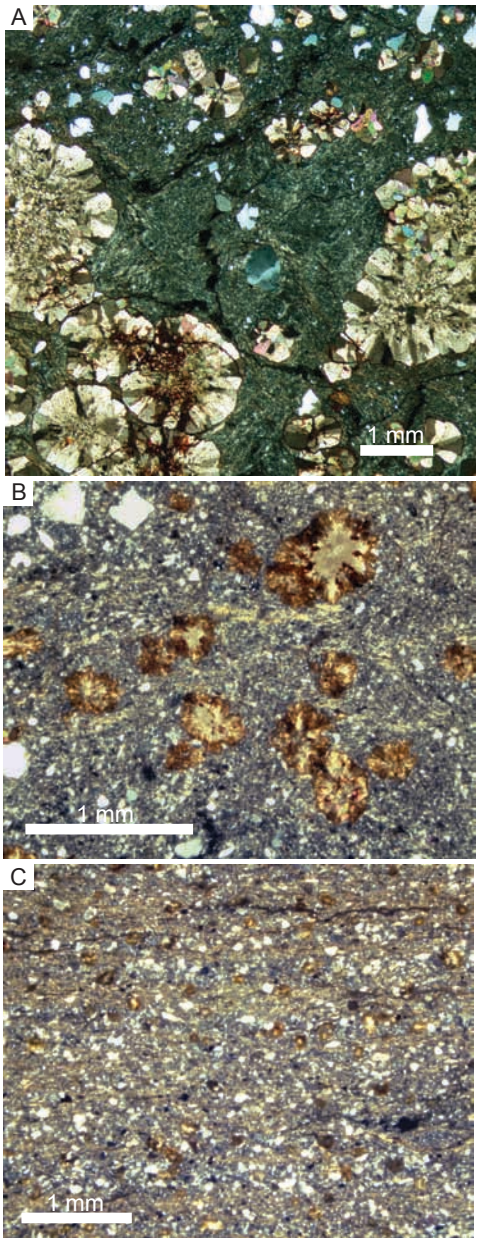

FIGURE 7—Photomicrographs under crossed polarized light of birefringence fabrics (b-fabrics). Scale bars = 1 mm. A) Photomicrograph of the horizon at 959.77 m of the Los Mangos 4 core showing cross-striated b-fabric (bright streaks of clay minerals within the clay matrix forming a cross pattern) to granostriated b-fabric (bright streaks of clay minerals around quartz grains and sphaerosiderites). B) Dominantly parallel-striated b-fabric (streaks of clay oriented parallel to each other. to granostriated b-fabric in horizon at 799.15 m of the Santa Clara 2 core. C) Strial b-fabric (preferred parallel orientation that becomes extinct when rotated) in horizon at 802.50 m of the Santa clara 2 core.

consist of speckled b-fabrics consisting of smaller random domains of birefringent zones.

The fine-grained groundmass of the lower portion of the Santa Clara 2 core is characterized by strial b-fabric, consisting of thin layers of horizontally oriented clay layers that exhibit a uniform extinction with a speckled pattern (Fig. 7C). The upper horizon (799.22 m to 799.01 m) from the Santa Clara 2 core that was sampled consists of a groundmass that is characterized by parallel striated, cross striated, and granostriated b-fabrics.

The mudstone horizons in the lower portion of the San Francisco 52 core consist of fine-grained groundmass characterized by parallel-striated, cross-striated and granostriated b-fabrics. The upper, longer section of the San Francisco 52 contains horizons (873.18 m, 871.75 m, and 861.96 m to 860.08 m) characterized by speckled b-fabric to parallel-striated b-fabric. The remaining horizons (871.54 m to 871.45m and 867.32 m to 864.28 m) are characterized by parallel striated, cross-striated, and granostriated b-fabrics.

Mineral Accumulations

Mineral accumulations include siderite (primarily in the form of sphaerosiderites), pyrite (primarily framboids), and Fe-oxide accumulations. From the Los Mangos 4 core, sphaerosiderites range from 1 to 2 mm in diameter, have radiating crystallites that range from fibrous to thicker, bladed crystals. Some appear concentrically zoned, suggesting more than one period of crystal growth.

Sphaerosiderites in horizon 959.93 m are particularly cloudy and are enriched in pyrite inclusions relative to the surrounding matrix. These sphaerosiderites often have a thin outer rim of more clear radial crystals. The five samples from the Los Mangos core all have some pyrite framboids and/or pyritized organic material in the fine-grained matrix, and many sphaerosiderites have engulfed these pyrite crystals or have nucleated around pyrite (Fig. 8A). Sphaerosiderites are often oxidized along the rims or along fractures and between crystallites.

Sphaerosiderites approximately 0.2 to 0.7 mm in diameter occur in horizons 799.22 m, 799.15 m, and 799.01 m of the Santa Clara 2 core, and consist of radial-fibrous crystallites. These sphaerosiderites have oxidized rims. Oxidized siderite crystals, less than 0.2 mm in diameter, occur in the sample at horizon 802.50 m. Minor amounts of pyrite occur in these samples, primarily in the lowest sample (802.52 m).

The bottom four samples of the lower portion of the San Francisco 52 core contain small sphaerosiderites approximately 0.2 mm in diameter or smaller with minor oxidation rims. The sample at horizon 894.04 m contains abundant pyrite framboids 0.02 to 0.03 mm in diameter. A few pyrite framboids are much larger approximately 0.2 mm in diameter (Fig. 8B). A sandstone horizon at 893.73 m is cemented by microspar to sparry, subhedral intergranular siderite, chalcedony, and minor amounts of calcite. The largest siderite spar crystals have dimensions of approximately 0.2 by 0.3 mm.

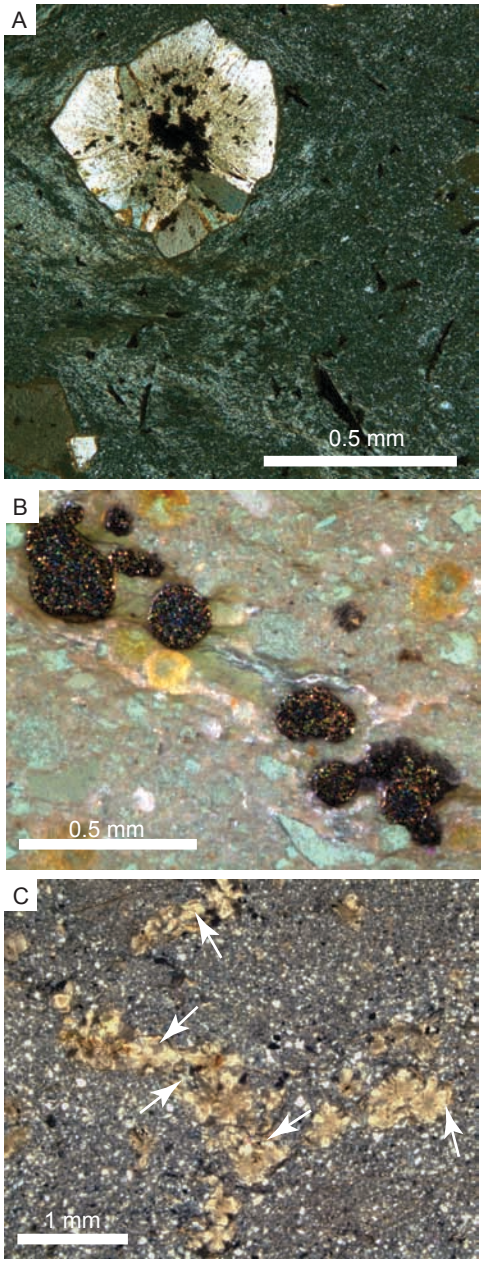

FIGURE 8—Photomicrographs of mineral accumulations. A) Photomicrograph (crossed polarized light) of a sphaerosiderite with pyrite nuclei and flecks of pyritized organic material (opaque material) within the Los Mangos 4 core, horizon at 957.61 m. Note also the granostriated b-fabric. Scale bar = 0.5 mm.
B.) Photomicrograph of large pyrite framboids from the San Francisco 52 core, horizon 894.08 m taken under transmitted and reflected light. Scale bar = 0.5 mm.
C) Photomicrograph (cross polarized light) of a sinuous cluster of sphaerosiderites with thin clay coatings (arrows) at horizon 861.63 m of the San Francisco 52 core. Scale bar = 1 mm.

Sphaerosiderites in the upper section of the San Francisco 52 core generally consist of radial fibrous to bladed crystallites, and have diameters ranging from 0.4 mm to 1.0 mm. Sphaerosiderites often form in clusters, sometimes sinuous clusters (Fig. 8C) associated with roots or burrows. The majority of the samples contain pyrite framboids in the surrounding matrix. Some pyrite framboids are engulfed by the siderites. Sphaerosiderites from 860.08 m consist of microcrystalline cores, surrounded by a band of pyrite framboids, and an outer zone of radial fibrous siderite crystallites. Minor amounts of oxidation occur on rims of sphaerosiderites; however, somewhat more heavily oxidized rims of sphaerosiderites occur in regions where they are associated with iron-oxide preserved burrows. Some sphaerosiderites at 871.54 m and 871.75 m also appear to have a zone of pyrite growth.

Clay Coatings

Clay coatings occur as highly birefringent domains of clay minerals lining voids or grains. In the Los Mangos 4 core thin clay coatings occur around some quartz grains in the sample at 959.77 m, as well as in small voids of the sandy horizon at 957.50 m, and within a vertically oriented sand-filled burrow at 957.38 m (Fig. 9A).

Thicker more developed clay coatings occur along and between sphaerosiderites in the Santa Clara 2 core, at horizons 799.22 m and 799.15 m (Fig. 9B). In addition, thin clay coatings occur along sinuous to irregular subhorizontal partings within the rock.

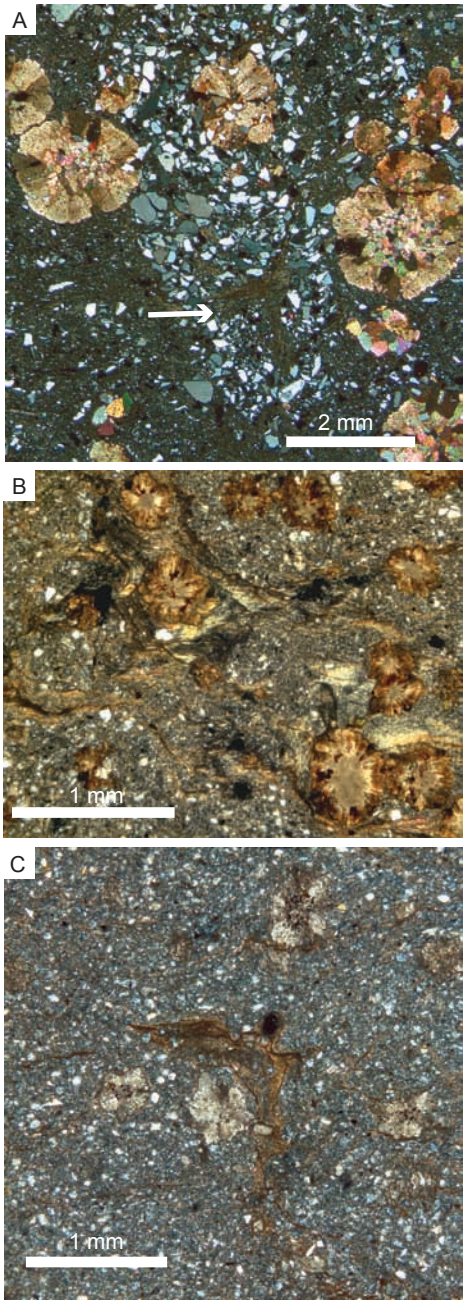

FIGURE 9—Photomicrographs of various forms of clay coatings taken under crossed-polarized light. A) Photomicrograph showing a sand-filled vertical burrow with crescent shaped clay coating (arrow) and sphaerosiderites from the Los Mangos 4 core, horizon 957.38 m. Scale bar = 2 mm. B) Clay coatings along sphaerosiderites and subhorizontal partings in horizon in the Santa Clara 2 core, horizon 799.15 m. Scale bar = 1 mm. C) Photomicrograph of a sinuous, branching parting with clay coating from the San Francisco 52 core, horizon 860.08 m. Photomicrograph taken under cross polarized light. Scale bar = 1 mm.

Mudstones in the lower portion of the San Francisco 52 core contain clay coatings along subhorizontal, sinuous partings within the rock. Sphaerosiderites occasionally occur associated with these partings and also have thin clay coatings. Clay coatings occur in most of the samples through the upper section of the San Francisco 52 core. As in the lower portion of the core, thin clay coatings occur along subhorizontal, sinuous partings within the rock which often branch (Fig. 9C). Sphaerosiderites that occur in clusters or along these sinuous partings often have thin clay coatings (Fig. 8C). These clusters of sphaerosiderites are especially common in horizons 861.96 m to 861.06 m.

Stable Isotopes

Overall, the data for thirteen individual sphaerosiderite-bearing horizons consists of relatively invariant $\delta^{18}O$ values with highly variable $\delta^{13}C$ values, defining 13 MSLs (Table 2 and Fig. 10). The average $\delta^{18}O$ of each of the 13 horizons ranged from -3.91‰ to -5.23‰, with the $\delta^{13}C$ values ranging from -16.02‰ to -2.37‰.

One horizon contained sphaerosiderites whose isotopic compositions did not produce a MSL, and had highly variable $\delta^{18}O$ and $\delta^{13}C$ values, and also had more depleted $\delta^{18}O$ values than all of the other sphaerosiderites horizons. The sphaerosiderites at horizon 959.93 m from the Mangos 4 core are immediately underlain by sandstone approximately 3 m thick. Pore fluids flowing through this sandstone might have been sourced from isotopically lighter, high altitude precipitation and might have caused these sphaerosiderites to be lighter than other

Table 2. Average $\delta^{18}O$, standard deviation, and range of $\delta^{13}C$ of sphaerosiderite lines from the Caballos Formation.

Core	Horizon	$\delta^{18}O$ (average, VPDB)	$\delta^{18}O$ (Standard Deviation)	$\delta^{13}C$ (range, VPDB)
Los Mangos 4	957.38 m (3141.00 ft)	-4.75‰	0.52‰	-14.41‰ to -16.02‰
	957.61 m (3141.75 ft)	-3.91‰	0.47‰	-13.01‰ to -13.90‰
	959.77 m (3148.85 ft)	-3.92‰	0.38‰	-9.51‰ to -12.15‰
Santa Clara 2	799.01 m (2621.42 ft)	-4.32‰	0.12‰	-1.82‰ to -5.72‰
	799.15 m (2621.88 ft)	-4.60‰	0.13‰	-13.79‰ to -15.04‰
	799.22 m (2622.11 ft)	-4.55‰	0.11‰	-10.82‰ to -13.94‰
San Francisco 52	861.82 m (2827.50 ft)	-4.39‰	0.09‰	-5.33‰ to -8.17‰
	864.28 m (2835.58 ft)	-4.70‰	0.48‰	-7.60‰ to -14.01‰
	864.51 m (2836.33 ft)	-5.23‰	0.72‰	-9.64‰ to -12.89‰
	867.23 m (2845.25 ft)	-4.17‰	0.51‰	-2.13‰ to -4.15‰
	867.32 m (2845.54 ft)	-4.32‰	0.80‰	-2.37‰ to -4.62‰
	871.75 m (2860.08 ft)	-4.48‰	0.21‰	-7.80‰ to -8.99‰
	873.18 m (2864.75 ft)	-3.96‰	0.22‰	-2.24‰ to -9.28‰

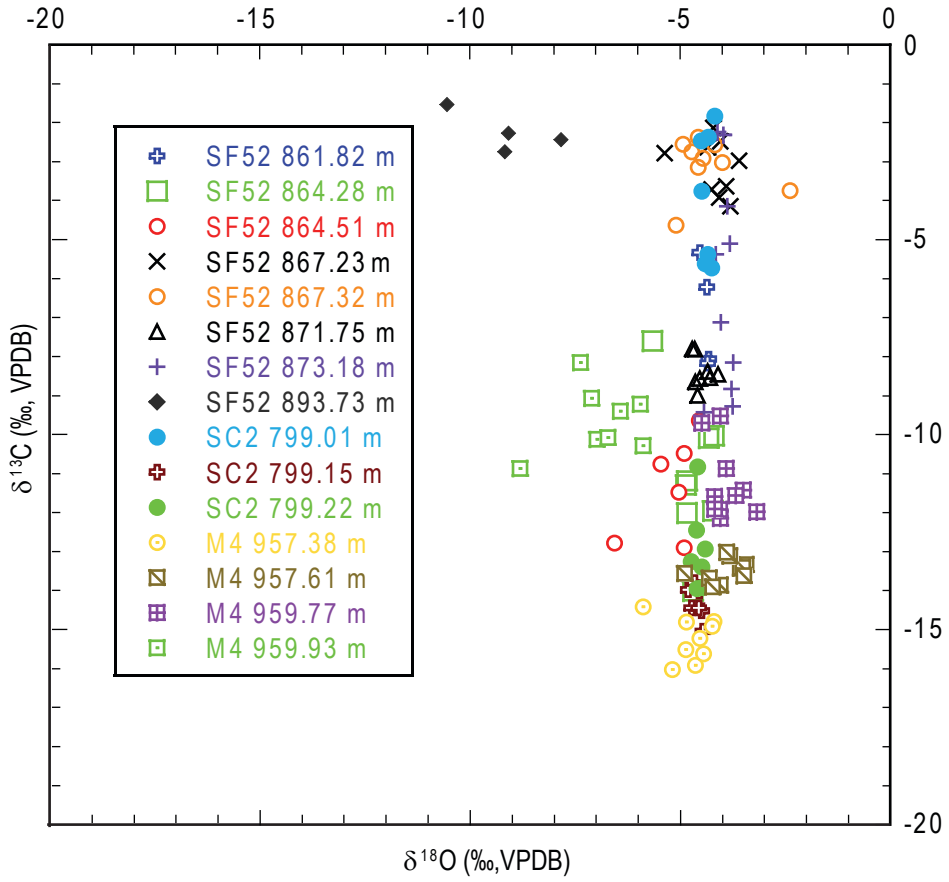

FIGURE 10—Plot of $\delta^{18}O$ vs. $\delta^{13}C$ for sphaerosiderites from the Caballos Formation.

sphaerosiderites which were more distal to channel sandstones (see Discussion). The siderite-cemented sandstone (San Francisco 52 893.73 m) produced variable $\delta^{18}O$ values (ranging from -7.82 to -10.54‰) and variable $\delta^{13}C$ values (ranging from -1.52 to -2.75‰).

INTERPRETATIONS

Depositional Setting and Paleosols

The Caballos Formation in the Upper Magdalena Valley consists of terrestrial strata that, according to ICP core interpretations (1999, 2000a, 2000b), are characterized by fluvial channels, crevasse splays, passive channel fills, and floodplain environments. Petrographic observations provided in this study offer additional important details regarding the ancient conditions of paleosols that formed in floodplains, channel fills, and crevasse splays. Overall, the paleosols are characterized by gleyed colors (N7 to N6, light gray to gray), root traces (Fig. 6A and 6B), and sphaerosiderites. Sphaerosiderites form under reducing conditions in water-saturated soils (Ludvigson et al., 1998). The overall gleyed (chroma <2) appearance of the soils also indicates waterlogged conditions (Birkeland, 1999). The presence of iron-oxide cemented burrows, weak red mottles that represent redoximorphic conditions, and clay coatings suggests, however, that sometime during their formation, the soil conditions were moderately well-drained and above the water table (McCarthy et al., 1999; Birkeland, 1999, Ufnar et al., 2001). In addition, the birefringence fabrics that occur in the fine-grained groundmass occur due to pressure

and tension of the clays often due to wetting and drying of the soil or bioturbation (Brewer, 1960, Fitzpatrick, 1993; Retallack, 1997, Stoops, 2003).

The presence of pyrite framboids suggest the paleosols were occasionally influenced by sulfate-bearing waters. This is consistent with influence by marine or mixed marine-freshwater fluids and with the fluvial-estuarine interpretations by previous authors (Villamil et al., 1999; Acevedo and Pennington, 2003). The addition of sulfate-rich waters to organic rich-sediments where organic matter degradation has evolved to anoxic conditions results in sulfate reduction, releasing sulfide that reacts with available reduced iron and quickly precipitates pyrite (Curtis and Coleman, 1986). Most paleosols are characterized by pyrite that precipitated early during soil formation or before active pedogenesis occurred. This is suggested by siderites that have nucleated around pyrite or engulfed pyrite that was present in the matrix during their growth. Siderite began to precipitate as the source of sulfate was removed or sulfate was depleted and organic matter degradation progressed to the methanogenic phase (Gautier and Claypool, 1984). Some soils appear to have multiple phases of pyrite and siderite precipitation. These alternations between pyrite and siderite growth indicate that either the local base level oscillated, or lateral progradation and retrogradation of the shoreline influenced the pore water chemistry such that sulfate availability was the primary factor in precipitation of either pyrite or siderite (Ludvigson et al., 1996; Ufnar et al., 2001).

Detailed descriptions for paleosols of each core are given below. When possible, paleosols are classified following USDA soil taxonomy nomenclature

(USDA, 1999) and aided by petrographic characteristics as described in Retallack (1997).

Los Mangos 4 Core

The lower fining upward section between 960.12 m and 957.61 m (Fig. 2) are claystones which have parallel-striated, cross striated and granostriated b-fabrics that are indicative of soil development that includes wetting and drying, bioturbation due to roots and soil organisms, and displacement of clay by the well-developed sphaerosiderites (Fig.s 7A, and 8A). The gleyed color (N6) and sphaerosiderites indicate that ancient soil conditions were dominated by water-saturated conditions. Thin clay coatings represent clay illuviation and moderately well-drained conditions. The break in rock recovery just above 959.77 m might suggest that this interval represents two paleosols, both of which resemble weakly developed ultisols, as there are high clay contents (argillic or kandic horizons), and no weatherable minerals such as feldspars. The pyrite is an early diagenetic feature of the parent material in which sulfate-rich water (i.e. seawater) influenced the sediment before it became influenced by pedogenesis and freshwater influence, based on the observation that some sphaerosiderites (e.g. 957.61 m) nucleated around pyrite framboids (Fig. 8A). This might suggest a drop in base level to bring the sedimentary material into the zone of pedogenesis. Well-drained conditions in the paleosol were not prevalent as there are no redoximorphic features associated with the soil. The lowermost sample (horizon 959.93 m) contains sphaerosiderites which may have been influenced by isotopically

lighter water, possibly sourced from higher elevations, flowing through the immediately underlying sandstones. This interpretation would explain the lighter values that do not show a MSL trend.

The paleosol represented by the upper two samples of the Los Mangos 4 core are sandstones or clayey sandstones and have speckled b-fabric to parallel striated b-fabric. Like the lower sample, pyrite occurred as an early diagenetic product of the influence of sulfate-rich water in the parent material. A base level drop would have brought the parent material into the zone of active pedogenesis. Small relict cross-beds are present in the uppermost sample suggesting poorly developed paleosols. Thin clay coatings represent moderately well-drained conditions allowing some translocation of clays (Fig. 9A). Immature soils with some clay accumulation can be interpreted as an inceptisol.

Santa Clara 2 Core

The lower two samples (802.52 m and 802.50 m) (Fig. 3) are silty mudstones to fine sandstones with horizontal bedding and no evidence of pedogenesis suggesting they are not paleosols (Fig. 7C). Alternatively, this lower section could have been truncated and the horizontally bedded section of a C-horizon.

Teichichnus is a marine trace fossil, and *Paleophycus* is often associated with sub-aqueous, often estuarine conditions. The ichnofauna, along with the minor amounts of pyrite would suggest deposition in an estuarine environment that

transitioned to saturated freshwater conditions marked by the formation of small siderite crystals in horizon 802.50 m that are not pedogenic in origin.

The paleosol represented by samples at 799.01 m, 799.15 m, and 799.22 m is characterized by cross striated to granostriated b-fabrics (Fig. 7B) and thicker clay coatings, (Fig. 9B) and does not contain weatherable minerals. These features are suggestive of ultisols. Soil conditions were likely initially saturated (sphaerosiderite formation) and transitioned to more well-drained conditions allowing for translocation of clay minerals forming clay coatings and the slight oxidation of sphaerosiderites (McCarthy and Plint 1998; McCarthy et al., 1999). The soil maintains its overall gleyed (2.5Y6/1 to 2.5Y5/1, gray) appearance throughout, suggesting periods of well-drained conditions were short; however, the paleosol is likely truncated by the overlying fluvial channel, so redoximorphic features that might indicate well-drained conditions, could have been eroded.

San Francisco 52 Core

Within the lower portion of the San Francisco 52 core (Fig. 4), the mudstone horizon from approximately 895.73 m to 894.59 m is characterized by parallel striated b-fabrics and small sphaerosiderites. Thin subhorizontal clay coatings along partings are interpreted as root traces. This paleosol likely represents an immature soil, possibly an inceptisol. A thin mudstone exists between two sandstones that overlie the paleosol (894.08 m). The sample from this mudstone exhibits parallel to cross striated and granostriated b-fabrics, small sphaerosiderites, and thin clay

coatings, and also resembles an inceptisol based on clay coatings and b-fabric. An interesting feature of this horizon is the presence of large pyrite framboids (up to 0.2 mm in diameter) throughout the matrix and smaller ones within some sphaerosiderites (Fig. 8B). Pyrite formed as an early diagenetic mineral from sulfate-rich fluids (marine or mixed freshwater-marine) as a result of anaerobic sulfate reduction.

The lack of significant compaction of the sand grains from the sandstone at 893.73m, with siderite cements filling high intergranular volume (approximately 30%), suggests the siderite cements are early diagenetic cements. The sparry nature of these siderites is different than that of the sphaerosiderites (radial bladed to fibrous crystals) in the paleosols, possibly suggesting a difference in the pore fluids from which these siderites were precipitated.

The upper and longer portion of the San Francisco 52 core contains multiple paleosols (Fig. 5). The lowermost sample (873.18 m) is characterized by speckled b-fabric with small areas containing parallel-striated b-fabrics. This horizon is also characterized by large sphaerosiderites, some of which have coalesced into siderite-cemented patches, and thin clay coatings. The paleosol was likely an inceptisol

The three samples from approximately 871 m are at the base of a much thicker paleosol. The paleosol has an overall gleyed (N6 to N7) appearance suggesting seasonally water saturated conditions were prevalent. The paleosol is characterized by speckled b-fabric at the base, and parallel-striated to granostriated in the upper two samples. Thin clay coatings along sinuous subhorizontal partings are interpreted as root traces. In addition, the siderites at 871.75 m are more abundant and larger than

those of the two samples above. This is most likely a result of these siderites residing in the reduced waters of the saturated zone for longer periods than those above. The overlying samples have better preserved thin clay coatings suggesting slightly more well-drained conditions were more frequent higher in the soil. Sphaerosiderites in the lower two samples (871.75 m and 871.54 m) have a concentric zone in which small pyrite framboids are abundant indicating a temporary incursion of sulfate-rich waters (i.e. marine fluids) leading to pyrite precipitation. The soil represented by this paleosol was likely an inceptisol.

The upper 9 m of mudstone we interpret as cumulative paleosols. The horizon at 864 m contains abundant redoximorphic features represented by reddish iron oxides concentrated within burrows or as mottles and throughout the paleosol (Fig. 6B). These features represent seasonally fluctuating water tables and better drained soil conditions than those in the more hydromorphic soils described above. Clay coatings along sinuous, subhorizontal partings are interpreted as root traces and sphaerosiderites are commonly found along these sinuous partings (Fig. 8C and 9C). The sphaerosiderites also have clay coatings suggesting changes in saturation and drainage. The branching sand-filled burrows (Fig. 6C) and Fe-stained interconnected burrows (Fig. 6B) resemble those attributed to either ants or termites. Both insects produce interconnected chambers and galleries that often form a grid-like lattice, and would have produced the burrows during periods in which soils were above the water table (Hasiotis, 2006). A change in saturation from oxidized to reducing conditions is indicated by the fact that sphaerosiderites cross cut many of the Fe-oxide stains and

concentrations. The dominance of gleyed colors (N6) and the generally un-oxidized state of sphaerosiderites indicate that hydromorphic features subsequently dominated the soils. The lack of weatherable minerals, the abundance of clay coatings, accumulation of redoximorphic features, and the presence of cross striated b-fabrics suggest these paleosols were similar to modern ultisols. Sandier horizons (865.90 m) that are characterized by speckled b-fabrics (861.95 m to 860.08 m) may represent inceptisols. The upper horizon, especially the sample at 860.08 m, contains sphaerosiderites characterized by concentric bands of pyrite framboids within the nodules, recording the temporary influence of sulfate-rich waters.

Estimate of Paleogroundwater Isotopic Composition

The average oxygen isotopic compositions of the sphaerosiderites at each horizon that define unique MSLs can be used to calculate the compositions of the groundwaters from which they were precipitated. To do this, we utilized the temperature-dependent fractionation equation for siderite from Carothers et al. (1988), and a zonal paleotemperature estimate based on Cretaceous leaf physiognomy data of Wolfe and Upchurch (1987) and Spicer and Corfield (1992) as reported by Ufnar et al. (2002).

$$t = 30.25 - 0.2025 \bullet l - 0.0006 \bullet l^2$$

During the Aptian-Albian, northern South America was located just south of the paleoequator (Meschede and Frisch, 1998; Villamil et al., 1999). Using a paleolatitude of 2°S for the Caballos Formation, the mean annual temperature during the formation of sphaerosiderites in paleosols is estimated at approximately 30°C.

The oxygen isotopic compositions of groundwaters calculated from the meteoric sphaerosiderite lines are summarized in Table 3. The average oxygen isotopic composition of groundwater determined by MSLs from the Caballos Formation is -4.56 ± 0.38‰ (VSMOW).

DISCUSSION

According to Guerrero et al. (2000) sediments making up the Caballos Formation were sourced mostly from the emerging highlands to the west of the basin. The paleosol-bearing strata were deposited on a broad coastal deltaic to estuarine complex during the early stages of a major transgression (Villamil et al., 1999). The Cretaceous Colombian Basin was subject to frequent sea level oscillation as indicated by alternating fluvial deposits and shallow marine to estuarine deposits in the Caballos Formation. Numerous paleosols attest to the repeated exposure of these sediments, while the common presence of pyrite in several sequences indicates reducing conditions in phreatic systems dominated by seawater or freshwater-seawater mixed fluids on a coastal plain near sea level.

The micromorphology of some paleosols of the Caballos Formation is characteristic of seasonally saturated soils that we interpret as inceptisols and some ultisols. These soils occur in warm, humid environments (USDA Soil Taxonomy, 1999) and are similar to modern soils that occur in lowlands of Colombia and Venezuela today and various

Table 3. Isotopic compositions of meteoric water calculated from MSLs

Core	Horizon	MSL $\delta^{18}O$ (average VPDB)	Meteoric Water $\delta^{18}O$ (VSMOW)
Los Mangos 4	957.38 m (3141.00 ft)	-4.75‰	-4.90‰
	957.61 m (3141.75 ft)	-3.91‰	-4.06‰
	959.77 m (3148.85 ft)	-3.92‰	-4.07‰
Santa Clara 2	799.01 m (2621.42 ft)	-4.32‰	-4.51‰
	799.15 m (2621.88 ft)	-4.60‰	-4.75‰
	799.22 m (2622.11 ft)	-4.55‰	-4.70‰
San Francisco 52	861.82 m (2827.50 ft)	-4.39‰	-4.54‰
	864.28 m (2835.58 ft)	-4.70‰	-4.85‰
	864.51 m (2836.33 ft)	-5.23‰	-5.38‰
	867.23 m (2845.25 ft)	-4.17‰	-4.32‰
	867.32 m (2845.54 ft)	-4.32‰	-4.47‰
	871.75 m (2860.08 ft)	-4.48‰	-4.63‰
	873.18 m (2864.75 ft)	-3.96‰	-4.11‰

other tropical regions in Africa, Asia, and the southeastern regions of the USA. These soils most likely developed during lowstands in the more distal parts (i.e. farther away from channels or estuary shoreline) of the fluvial-estuarine system where the Caballos sediments accumulated. The paleosols interpreted as entisols and inceptisols were probably developed in the more proximal portions of the system (i.e. closer to fluvial or tidal channels or to the estuary shoreline) where pedogenesis occurred for shorter amounts of time.

The constructional coalesced deltaic system found along the southwestern to west-central coast of present-day Colombia in the Nariño, Cauca, and Valle del Cauca provinces (Martinez et al., 1995), albeit west facing, can serve as a modern analogue for these environments. This modern coalesced deltaic system has developed along a narrow coastal plain with mountains to the east, and receives yearly precipitation in excess of 150 cm/yr and as high as 800 cm/yr, and sediment yields are higher than the larger watersheds of the Magdalena Valley (Restrepo and Kjerfve, 2000). The system is subject to rapid inundation or exposure with minor sea level oscillation and fresh-seawater mixing is common (Murphy 1939). The majority of soils in the areas of this coastal plain are entisols, and inceptisols with minor ultisols and histosols (Anonymous 1983).

The $\delta^{18}O$ values for the Caballos Formation are similar to, though slightly more enriched than, estimated modern values of precipitation falling over fluvial estuarine systems in the western coast of South America in both the northern and southern hemispheres such as the complex deltaic-estuarine system in the Gulf of

Guayaquil, Ecuador (~ 2.2 °S), and the coalesced deltatic system of western Colombia (~ 2-4° N) (Bowen, 2009). Using Oxygen Isotopes in Precipitation Calculator (Bowen, 2009; Bowen and Revenaugh 2003; www.waterisotopes.org) precipitation $\delta^{18}O$ values over these systems are estimated at -5.0 ± 0.6 ‰ VSMOW. Extrapolation of the second-order polynomial regression for the sphaerosiderite $\delta^{18}O$ data presented in Ufnar et al., (2002), predicts sphaerosiderite values of ~ +1.55‰ (VPDB) at 2ºS (Figure 11). These values would require groundwater compositions of approximately +1.4 ‰ (VSMOW). The $\delta^{18}O$ values for Colombia MSLs ranging from -3.91‰ to -5.23‰ (VPDB) are much lighter (Figure 11) than the value extrapolated from the data of Ufnar et al. (2002), and require groundwater $\delta^{18}O$ values for the Caballos Formation of -4.56 ± 0.38 ‰ (VSMOW). The oxygen isotopic composition of precipitation calculated from Caballos Formation sphaerosiderites is slightly more positive than values generated by recent GCM simulations by Poulsen et al. (2007) that calculated precipitation $\delta^{18}O$ values of lower than -5‰ (VSMOW) for this area of Colombia. Of special note, near equatorial $\delta^{18}O$ values of simulated mid-Cretaceous precipitation reported by Poulsen et al. (2007) appear to be quite insensitive to the different temperatures (28-32°C) and precipitation amounts (255-330 cm/year) produced by their different CO_2 concentration scenarios (2-12x modern CO_2).

It has been suggested by Poulsen et al (2007) that high latitude depleted $\delta^{18}O$ values reported by Ufnar et al. (2002) for paleogeographic sites close to orogens

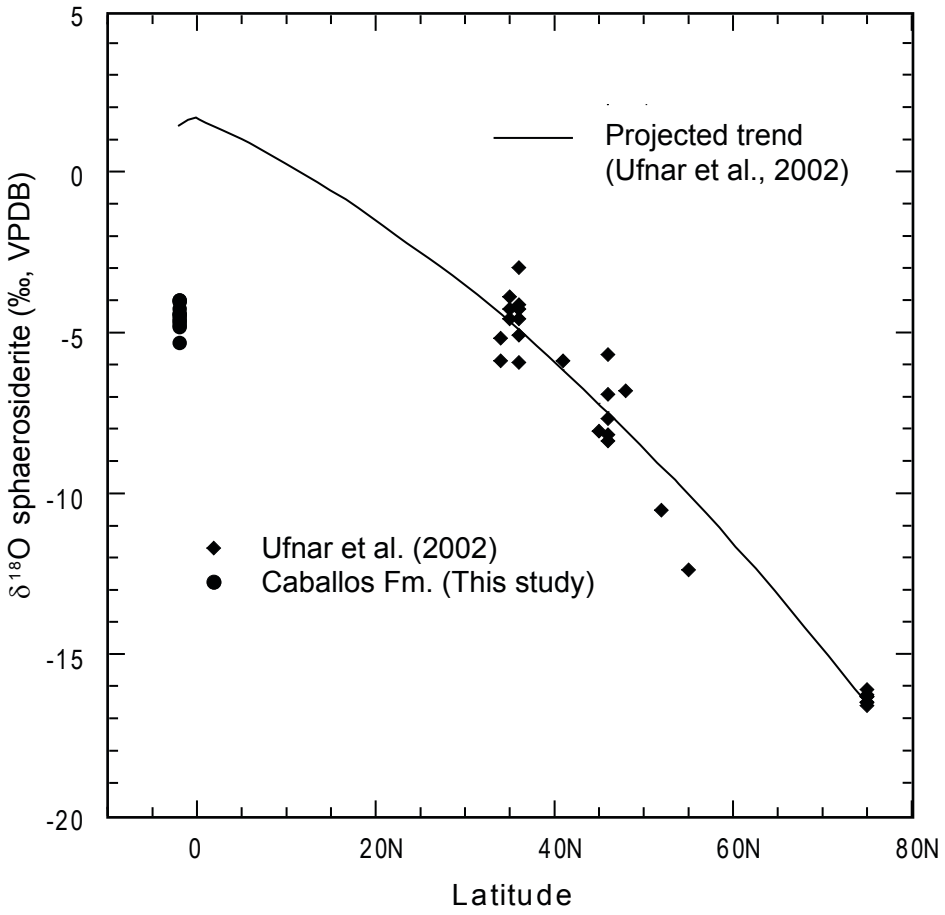

FIGURE 11—Latitudinal gradient of $\delta^{18}O$ composition of sphaerosiderites for the mid-Cretaceous based on paleosols between 35 - 75°N. The line is a second order polynomial fit to this data and extrapolated to the equatorial region. Caballos Formation sphaerosiderites compositions are lighter than values based on the projection.

might have been influenced by orographic effects near high mountain ranges. Altitude as well as distance, and amount effects influence the oxygen isotopic composition of precipitation, with increasing altitude, distance from source waters and intense rainout all causing depletion in the $\delta^{18}O$ values. Because Caballos sediments were being sourced from moderate altitude systems surrounding the Cretaceous Colombian Basin, altitude might be perceived as a possible influence on groundwater $\delta^{18}O$ values; however, study of carbonate cements and sphaerosiderites in the Dakota Formation (Nebraska and Iowa region) and the Boulder Creek Formation (British Columbia) (Phillips et al., 2007; Phillips 2004) suggests that high altitude precipitation runoff only influenced regional aquifers and that this signal was recorded in the isotopic composition of early cemented sandstones. Sphaerosiderites, found in paleosols of the interfluvial portions of the estuary to coastal plain environments captured the local lowland precipitation, and were unaffected by the high altitude and isotopically lighter runoff. The siderite-cemented sandstone at 893.73 m of the San Francisco 52 core has $\delta^{18}O$ values that are ~4‰ lighter than the average of the MSL values for all the paleosol horizons. This difference is of similar magnitude to that observed by Phillips (2004) between siderite-cemented sandstones and MSLs of the Boulder Creek Formation. It is likely that the values from the sandstone at 893.73 m represent cementation from streams draining regional aquifers that were influenced by high altitude precipitation on the ancestral Central Cordillera detrital source rocks (Guerrero et al., 2000, 2002). The sphaerosiderites of the Caballos Formation likely reflects local precipitation and may be one reason the

MSL-based precipitation compositions are slightly more enriched than the regional estimates of Poulsen et al. (2007) as well as the interpolated values of Bowen (2009).

Using a simple Rayleigh fractionation model (under equilibrium conditions) and a mid-Cretaceous seawater isotopic composition of -1.2‰ (Poulsen et al., 2007), approximately 32‰ of the water vapor from the air mass would have to be lost to precipitation to produce the -4.56‰ VSMOW precipitation value calculated from the Caballos MSLs. A loss of 32% of the water vapor seems to be an unreasonable value if air masses were generated only a few tens of kilometers away, solely from the Cretaceous Colombian Basin.

The Cretaceous Colombian Basin was a southwest-northeast trending basin open to the proto-Caribbean (Villamil et al. 1999) with sea surface (i.e. wind driven) currents bringing waters into the basin from the proto-Caribbean (Johnson, 1999). While Johnson (1999) admitted the difficulty of transporting proto-Caribbean waters southward across the equator, it is possible that seasonal deflections of the intertropical convergence zone over the South American continent could have produced wind-driven surface currents that transported proto-Caribbean waters into the basin. This deflection would most likely result in proto-Caribbean sourced air masses moving over the Guyana Shield and the Cretaceous Colombian Basin. Hence, the major source of precipitation over the Guyana Shield, which at this time drained westward (Potter, 1997; Ostos et al., 2005), and over the Cretaceous Colombian Basin, was the proto-Caribbean (Tethys). Thus, the precipitation falling on the fluvio-estuarine depositional settings inferred for the Caballos Formation was most

likely a combination of water vapor sourced from the adjacent sea and the proto-Caribbean.

During the Aptian-Albian, Johnson et al. (1996) proposed that Tethys was superheated and indeed other geologic data suggest intense evaporation in the tropics (Ziegler et al., 2003). Thus, evaporation in the proto-Caribbean would have resulted in localized ^{18}O enrichment of sea surface water to produce values heavier than -1.2‰. Indeed modeled precipitation $\delta^{18}O$ by Poulsen et al. (2007) shows the proto-Caribbean region precipitation as having heavy isotopic compositions ranging from -3 to -4 ‰. These values are only slightly lighter than those of precipitation over modern oceans, which range from -2.5 to -3.0 ‰ (VSMOW) (Gat, 1996), suggesting that surface waters in the superheated Tethys had isotopic compositions only slightly more depleted than those of modern oceans (~ 0 ‰ to 1.0 ‰ VSMOW) but significantly heavier than the estimated -1.2 ‰ estimated for mid-Cretaceous ocean.

Kinetic effects, recycling of water via evaporation, humidity effects, and the evolution of air masses while moving over the ocean all result in precipitation that is lighter than expected from simple equilibrium (Craig and Gordon, 1965; Gat 1996). As Cretaceous air masses from the proto-Caribbean moved southwest approximately 800 km toward the Cretaceous Colombian Basin, precipitation would be expected to become slightly more depleted. Furthermore, surface waters of the Cretaceous Colombian Basin were lower than the -1.2‰ VSMOW of the open oceans due to significant freshwater runoff from the Guyana Shield and ancestral Central Cordillera, producing vapor that was lighter than that arriving from the proto-

Caribbean. Thus, -4.56‰ VSMOW is a reasonable average estimate for the oxygen isotopic composition of precipitation over the Cretaceous Colombian Basin.

CONCLUSIONS

Macroscopic and microscopic features of paleosols in the Caballos Formation in Colombia suggest water-saturated soil conditions during the Aptian-Albian. Paleosols resemble modern entisols, inceptisols, and ultisols which also occur in coastal tropical regions of modern Colombia. Isotopic compositions of sphaerosiderites within the paleosols produce meteoric sphaerosiderite lines (MSLs) in $\delta^{18}O$ vs. $\delta^{13}C$ space. The average oxygen isotopic composition of the MSLs from the Caballos Formation is -4.41 ± 0.37‰ (VPDB), which is much lighter (by ~5‰) than projected values based on data from higher latitudes presented by Ufnar et al. (2002). The latitudinal trend for isotopic compositions of siderites presented by Ufnar et al. (2002), was not necessarily meant to be characteristic of all latitudes, however, the projected difference between the trend of Ufnar et al. (2002) and the revised trend presented here highlights the necessity of having a more complete latitudinal record of oxygen isotopic data. Using mean annual temperature estimates based on leaf physiognomy, the isotopic composition of groundwater, and thus precipitation, is estimated from average MSL values to be -4.56 ± 0.38‰ (VSMOW). These values are slightly more enriched than modern precipitation values at similar latitudes, as well as modeled precipitation values for the mid-Cretaceous. It is likely that more isotopically enriched sea surface waters from the superheated Tethys

Seaway (proto-Caribbean) were a significant source to air masses that produced these precipitation values.

REFERENCES

Anonymous, 1983, Soil map of Colombia: in Selvaradjou, S-K., L. Montanarella, O. Spaargaren and D. Dent, eds. 2005 European Digital Archive of Soil Maps (EuDASM) - Soil Maps of Latin America and Carribean Islands (DVD-Rom version). EUR 21822 EN. Office of the Official Publications of the European Comunities, Luxembourg.

Acevedo, H., and Pennington, W.D., 2003, Porosity and lithology prediction at Caballos Formation at the Puerto Colon oil field in Putumayo (Colombia): The Leading Edge, p. 1135-1141.

Barrero, D., Pardos, A., Vargas, C. A., and Martínez, J. F., 2007, Colombian Sedimentary Basins: Nomenclature, boundaries, and petroleum geology, a new proposal: Agencia Nacional de Hidrocarburos, Bogota, Colombia, 92p.

Barron, E. J., Hay, W. W., and Thompson, S., 1989, The hydrologic cycle: A major variable during Earth History: Palaeogeography, Palaeoclimatology, Palaeoecology, v. 75, p. 157-174.

Barron, E. J., and Moore, G.T., 1994, Climate model application in paleoenvironmental analysis, Short Course No. 33: Tulsa, SEPM 339 p.

Birkeland, P. W., 1999, Soils and Geomorphology: New York, Oxford University Press, 430 p.

Bowen, G. J., 2009, The Online Isotopes in Precipitation Calculator, version 2.2: http://www.waterisotopes.org.

Bowen G. J., and Revenaugh J., 2003) Interpolating the isotopic composition of modern meteoric precipitation: Water Resources Research 39, no. 10, 1299, doi:10.129/2003WR002086.

Bowen, G. J., and Wilkinson, B., 2002, Spatial distribution of $\delta^{18}O$ in meteoric precipitation: Geology, v. 30, no. 4, p. 315-318.

Brewer, R., 1964, Fabric and Mineral Analysis of Soils: New York, John Wiley and Sons, 470 p.

Carothers, W. W., Adami, L.H., and Rosenbauer, R.J., 1988, Experimental oxygen isotope fractionation between siderite-water and phosphoric acid liberated CO2-siderite: Geochimica et Cosmochimica Acta, v. 52, no. 10, p. 2445-2450.

Corrigan, H., 1979, The Geology of the Upper Magdalena Basin (Northern Portion), in Geological Field Trips, Colombia, CSGG: Bogota, p. 221-252.

Craig, H., and Gordon, L. I., 1965, Deuterium and oxygen 18 variations in the ocean and the marine atmosphere, in Tongiorgi, E., ed., Stable isotopes in oceanographic studies and paleotemperatures: Pisa, Consiglio Nazionale delle Ricerche Labratorio di Geologia Nucleare, p. 125.

Curtis, C. D., and Coleman, M. L., 1986, Controls on the precipitation of early diagenetic calcite, dolomite and siderite concretions in complex depositional sequences, in Gautier, D. L., ed., Roles of Organic Matter in Sediment Diagenesis: Tulsa, Society of Economic Paleontologists and Mineralogists.

Dansgaard, W., 1964, Stable isotopes in precipitation: Tellus, v. 16, p. 436-468.

Dansgaard, W., Johnsen, S. J., Clausen, H. B., and Gundestrup, N., 1973, Stable isotope glaciology: Meddelelser om Gronland, v. 197, p. 1-53.

Gautier, D. L., and Claypool, G. E., 1984, Interpretation of methanogenic dagenesis in ancient sediments by analogy with processes in modern diageneic environments, in McDonald, D. A., Surdam, R. C., ed., Clastic Diagenesis: Tulsa, AAPG Memoir 37, p. 111-123.

Guerrero, J., Sarmiento, G., and Navarrete, R., 2000, The stratigraphy of the W side of the Cretaceous Colombian Basin in the Upper Magdalena Valley. Reevaluation of selected areas and type localities including Aipe, Guaduas, Ortega, and Piedras: Geologia Colombia, v. 25, p. 45-110.

Guerrero, J., 2002, A proposal on the classification of systems tracts: Application to the allostratigraphy and sequence stratigraphy of the Cretaceous Colombian Basin. Part 2: Barremian to Maastrichtian: Geologia Colombia, v. 27, p. 27-49.

Gat, J. R., 1996, Oxygen and hydrogen isotopes in the hydrologic cycle: Annual Reviews Earth and Planetary Sciences, v. 24 p. 225-262.

Hay, W. W., and DeConto, R.M., 1999, Comparison of modern and Late Cretaceous meridional energy transport and oceanology, in Barrera, E., and Johnson, C.C., ed., Evolution of the Cretaceous ocean-climate system: Boulder, Geological Society of America Special Paper 332, p. 283-300.

Hasiotis, S. T., 2006, Continental Trace Fossils, SEPM Short Course Notes No. 51: Tulsa, SEPM, 132 p.

ICP, 1999, Registro de Descripción Sedimentologíca y Estratigráfica-Santa Clara 2: Ecopetrol.

-, 2000a, Registro de Descripción Sedimentológica y Estratigráfica-Los Mangos 4: Ecopetrol.

-, 2000b, Registro de Descripción Sedimentológica y Estratigráfica-San Francisco 52: Ecopetrol.

Jenkyns, H. C., Forster, A., Schouten, S., and Sinninghe Damste, J.S., 2004, High temperatures in the Late Cretaceous Arctic Ocean: Nature, v. 432, p. 888-892.

Johnson, C. C., 1999, Evolution of Cretaceous surface current circulation patterns, Caribbean and Gulf of Mexico: in Barrera, E., and Johnson, C. C., eds., Evolution of the Cretaceous Ocean-Climate System: Boulder, Colorado, Geological Society of America Special Paper 332, p. 329-343.

Johnson, C. C, Barron, E. J., Kauffmann, E. G., Arthur, M. A., Fawcett, P. J., and Yasuda, M. K., 1996, Middle Cretaceous reef collapse linked to ocean heat transport; Geology; v. 24; p. 376-380.

Lohmann, K. C., 1988, Geochemical patterns of meteoric diagenetic systems and their application to studies of paleokarst, in James, N. P., and Choquette, P.W., ed., Paleokarst: New York, Springer, p. 58-80.

Ludvigson, G. A., González, L. A., Witzke, B. J., Brenner, R. L., and Metzger, R. A., 1996, Diagenesis of iron minerals in the Dakota Formation, in Witzke, B. J.

and Ludvigson, G. A., *eds*., Mid-Cretaceous fluvial deposits of the eastern margin, Western Interior Basin: Nishnabotna Member, Dakota Formation: Iowa City, Iowa Department of Natural Resources, p. 31-38.

Ludvigson, G., González, L.A., Metzger, R.A., Witzke, B.J., Brenner, R.L., Murillo, A.P., and White, T.S., 1998, Meteoric sphaerosiderite lines and their use for paleohydrology and paleoclimatology: Geology, v. 26, no. 11, p. 1039-1042.

McCarthy, P. J., Faccini, U. F., and Plint, A. G., 1999, Evolution of an ancient coastal plain: paleosols, interfluves, and alluvial architecture in a sequence stratigraphic framework, Cenomanian Dunvagen Formation, NE British Colombia, Canada Sedimentology, v. 46, p. 861-891.

McCarthy, P. J. and Plint, A. G., 1998, Recognition of interfluve sequence boundaries: Integrating paleopedology and sequence stratigraphy: Geology, v. 26, no. 5, p. 387-390.

Munsell Color, 1975, Munsell soil color charts: Baltimore, Macbeth Division, Kollmorgen Corporation.

Meschede, M., and Frisch, W., 1998, A plate-tectonic model for the Mesozoic and Early Cenezoic history of the Caribbean plate: Tectonophysics, v. 296, p. 269-291.

Ostos, M., Yoris, F., and Avé-Lallemant, H. G., 2005, Overview of the southeast Caribbean-South American plate boundary zone: in Avé-Lallemant, H. G., and Sisson, V. B., eds. Caribbean-South American plate interactions, Venezuela: Geological Society of America Special Paper 394, p. 53-89.

Phillips, P. L., Ludvigson, G. A., Joeckel, R. M., González, L. A., Brenner, R. L., and Witzke, B. J., 2007, Sequence stratigraphic controls on synsedimentary cementation and preservation of dinosaur tracks; example from the Lower Cretaceous, (upper Albian) Dakota Formation, southeastern Nebraska, U.S.A: Palaeogeography, Palaeoclimatology, Palaeoecology, v. 246, no. 2-4, p. 367-389.

Potter, P. E., 1997, The Mesozoic and Cenozoic paleodrainage of South America: a natural history: Journal of South American Earth Sciences, v. 10, p. 331-344.

Poulsen, C. J., Pollard, D., and White, T.S., 2007, General circulation model simulation of the $\delta^{18}O$ content of continental precipitation in the middle Cretaceous: a model-proxy comparison: Geology, v. 35, p. 199-202.

Poulsen, C. J., 2004, A balmy arctic: Nature, v. 432, p. 814-815.

Restrepo, J. D., and Kjerfve, B., 2000, Water discharge and sediment load from the western slopes of the Colombian Andes with focus on Rio San Juan: Journal of Geology, v. 108, p. 17-33.

Retallack, G. J., 1997, A colour guide to paleosols: New York, Wiley, 175 p.

Rozanski, K., Araguas-Araguas, L., and Gonfiantini, R. , 1993, Isotopic patterns in modern global precipitation, in Swart, P. K., Lohmann, K.C., McKenzie, J., Savin, S. , ed., Climate Change in Continental Isotope Records, AGU, p. 1-36.

Soil Taxonomy, 1999, Soil Taxonomy: A basic system of soil classification for making and interpreting soil surveys, USDA, 871 p.

Spicer, R. A., and Corfield, R.M., 1992, A review of terrestrial and marine climates in the Cretaceous with implications for modelling the 'Greenhouse Earth': Geology Magazine, v. 2, p. 169-180.

Stoops, G., 2003, Guidelines for Analysis and Description of Soil and Regolith Thin Sections: Madison, Soil Science Society of America, 184 p.

Suarez, M. B., González, L. A., Ludvigson, G. A., Vega, F. J., and Alvarado-Ortega, J. , 2009, Isotopic composition of low-latitude paleoprecipitation during the Early Cretaceous: GSA Bulletin, v. 121, p. 1584-1595.

Ufnar, D. F., González, L.A., Ludvigson, G.A., Brenner, R.L., and Witzke, B.J., 2001, Stratigraphic implications of meteoric sphaerosiderite □18O values in paleosols in the Cretaceous (Albian) Boulder Creek Formation, NE British Colombia Foothills, Canada: Journal of Sedimentary Research, v. 71, no. 6, p. 1017 - 1028.

-, 2002, The mid-Cretaceous water bearer: isotope mass balance quantification of the Albian hydrologic cycle: Palaeogeography, Palaeoclimatology, Palaeoecology, v. 188, p. 51-71.

-, 2004, Evidence for increased latent heat transport during the Cretaceous (Albian) greenhouse warming: Geology, v. 32, no. 12, p. 1049-1052.

Ufnar, D. F., Ludvigson, G. A., González, L. A., Brenner, R. L., Witzke, B. J., and Leckie, D. A. , 2005, Ancient landscape development in the Late Albian Western Canadian Foreland Basin: Journal of Sedimentary Research, v. 75, p. 984-996.

Ufnar, D. F., Ludvigson, G. A., González, L., and Grocke, D. R., 2008, Precipitation rates and atmospheric heat transport during the Cenomanian greenhouse warming in North America: Estimates from a stable isotope mass-balance model: Palaeogeography, Palaeoclimatology, Palaeoecology, v. 266, p. 28-38.

Vegara S, L., 1995, Organic geochemical data from the Caballos Formation, Upper Magdalena Valley, Colombia: Revista Latino-Americana de Geoquímica Orgánica-ALAGO, v. 1, no. 1, p. 46-52.

Villamil, T., 1994, High-resolution stratigraphy, chronology and relative sea level of the Albian-Santonian (Cretaceous) of Colombia: University of Colorado, 473 p.

Villamil, T., Arango, C, and Hay, W.W., 1999, Plate tectonic paleoceanographic hypothesis for Cretaceous source rocks and cherts of northern South America, in Barrera, E., and Johnson, C.C., ed., Evolution of the Cretaceous Ocean Climate System: Boulder, GSA, Special Paper 332, p. 191-202

White, T., González, L., Ludvigson, G., and Poulsen, C. , 2001, Middle Cretaceous greenhouse hydrologic cycle of North America: Geology, v. 29, no. 4, p. 363-366.

White, T. S., Witzke, B.J., Ludvigson, G.A., Brenner, R.L., González, L.A., and Ravn, R.L., 2000, The paleoclimatological significance of Albian (mid-Cretaceous) sphaerosiderites from eastern Saskatchewan and western Manitoba, summary of investigations 2000: Saskatchewan Geological Survey Miscellaneous Report 2000-4.1, v. 1, p. 63-75.

Wolfe, J. A., and Upchurch, G.J.R., 1987, North American nonmarine climates and vegetation during the Late Cretaceous: Palaeogeography, Palaeoclimatology, Palaeoecology, v. 61, p. 31-77.

Ziegler, A. M., Eshel, G., McAllister Rees, P., Rothfus, T. A., Rowley, D. B., and Sunderlin, B., 2003, Tracing the tropics across land and sea: Permian to present: Lethia, v. 36, p. 227-254.

CHAPTER 4. THE MID-CRETACEOUS WATER BEARER REVISITED: QUANTIFICATION OF A GREENHOUSE HYDROLOGIC CYCLE IN THE AMERICAS

ABSTRACT

The response of the hydrologic cycle to global warmth is vital to understanding the global climate system during greenhouse conditions. Investigation of the Cretaceous greenhouse climate allows us to generate important data that can be utilized to constrain models used in forecasting future greenhouse conditions. This study builds on the Aptian-Albian sphaerosiderite $\delta^{18}O$ data set, a groundwater $\delta^{18}O$ proxy, presented by Ufnar et al. (2002) to include new and additional low latitude data including pedogenic and early meteoric diagenetic calcite $\delta^{18}O$. Ufnar et al (2002) used the proxy data derived from the North American Cretaceous Western Interior Basin (KWIB) in a mass balance model to estimate precipitation-evaporation fluxes. We have revised this mass balance model to handle sphaerosiderite and calcite proxies and to account for longitudinal travel by tropical air masses. We use empirical and GCM modeled temperature gradients for the mid-Cretaceous, and the empirically derived $\delta^{18}O$ composition of groundwater as constraints in our mass balance model. Precipitation flux, evaporation flux, relative humidity, seawater composition, and continental feedback are adjusted to generate model calculated groundwater $\delta^{18}O$ compositions (proxy for precipitation $\delta^{18}O$) that match the

empirically-derived groundwater $\delta^{18}O$ compositions to within ± 0.5‰. The model is calibrated against modern precipitation data sets.

Four different Cretaceous temperature estimates were used: the leaf physiognomy estimates of Wolfe and Upchurch (1987) and Spicer and Corfield (1992), the cool and warm Cretaceous GCM derived curves of Barron (1983) and data for the eastern KWIB margin derived from Poulsen's (1999) GCM simulations, presented in White et al. (2001). Precipitation fluxes for all the Cretaceous temperature gradients utilized in the model, are greater than modern precipitation fluxes. As expected calculated precipitation rates are all greater than modern precipitation rates. Calculated global average precipitation rates range from 371 mm/year to 1154 mm/year greater than modern precipitation rates. Our model results continue to support our research group's finding that increased rainout produces $\delta^{18}O$-depleted precipitation, and that locally derived recharge, not high altitude precipitation, is responsible for depleted pedogenic carbonate compositions.

Sensitivity testing of the model indicates that temperature, and air mass origin and pathways, significantly affect the oxygen isotopic composition of precipitation. Relative humidity is important in the tropical dry belt and significant reductions in relative humidity are required. Seawater ^{18}O enrichments are necessary in the tropical ocean to simulate proxy data, and are consistent with fossil and geologic evidence for a warmer and evaporatively enriched Tethys. Our results indicate that use of constant seawater $\delta^{18}O$ composition is not appropriate for mid-Cretaceous simulations.

INTRODUCTION

The vital role that water plays in the evolution of life on the planet, biogeochemical cycles, and global temperature regulation warrants detailed studies of the hydrologic cycle, especially in light of impending global warming. Barron et al. (1989) posited that a warmer global climate should cause an intensification of the hydrologic cycle. Knowledge of the functioning of the hydrologic cycle under warmer and higher atmospheric CO_2 concentrations can be gained by the study of ancient greenhouse worlds. Given that current atmospheric pCO_2 already exceeds the range of pCO_2 values estimated for the more recent thermal maxima of the Pleistocene and Holocene (Ruddiman, 2005; Soreghan et al., 2003) study of much older systems with higher CO_2 concentrations are necessary to gain the much needed insights into future climate change and to validate climate models. The mid Cretaceous (Aptian-Albian) greenhouse world with its high pCO_2, shallow temperature gradients, warm high latitudes, absence of polar ice, and an intensified hydrologic cycle (Ludvigson et al., 1998; Jenkyns et al., 2004; Poulsen, 2004; Ufnar et al., 2004) have the extreme conditions needed to validate climate models and to provide valuable knowledge to help us ascertain the impact of increased atmospheric CO_2 concentrations.

Our knowledge of the mid-Cretaceous greenhouse world, and particularly the hydrologic cycle response to increased global warmth has seen significant advances over the past two decades (Barron et al., 1989; Ludvigson et al., 1998; Hay and DeConto, 1999; Ufnar et al., 2002; Ufnar et al., 2004; Poulsen et al., 2007; Suarez et

al., 2009). This improved knowledge has led to the recognition that there are significant differences between climate model outputs and data inferred or extrapolated from geological and paleontological data. An important goal of recent studies has been to reconcile the known differences between climate models and climate proxies (e.g. Poulsen et al., 2007) and to generate large proxy data sets and derived climate data (e.g. White et al., 2001; Ufnar et al, 2002, 2004; Sorensen et al., 2002; Ludvigson et al., 2004). All of the research to date suggest some degree of intensified evaporation and precipitation during the mid-Cretaceous.

Ufnar et al. (2002) utilized Stella® Systems Modeling software to develop an oxygen isotope mass balance model to estimate the precipitation and evaporation fluxes needed to reproduce the observed $\delta^{18}O$ values of pedogenic sphaerosiderites collected from paleosols between 35°N to 75°N paleolatitude. The sphaerosiderite $\delta^{18}O$ data exhibits a pronounced depletion at high latitudes and model results suggest that this depletion requires overall increases in precipitation. Increases in precipitation are particularly high in the mid to high latitudes. For example, at 45°N paleolatitude, the mass balance model indicates precipitation rates of 2618 mm/year, which is more than three times the modern precipitation rate (Ufnar et al., 2002, Table 3). While the Ufnar et al. (2002) model lacked the complexity of a general circulation model (GCM), its importance resides in the ability to utilize empirical data to quantify the hydrologic cycle as well as to provide new insights for improving the more complex GCMs as has been demonstrated by Poulsen et al. (2007).

An obvious limitation of the Ufnar et al. (2002) model is that the data used to constrain precipitation and evaporation fluxes were limited to mid to high latitudes. The goal of this study is to incorporate new data from tropical and equatorial localities (Mexico and Colombia) to improve constraints on the mass balance model. To do so, the sphaerosiderite proxy data set is expanded to include isotope data from pedogenic calcites found in more evaporative settings as well as sphaerosiderite data from near equatorial settings. In addition to the expanded isotope constraints, the model has been modified to include adjustable air mass origin and initial $\delta^{18}O$ compositions, as well as adjustable air mass pathways (particularly along longitude in the subtropics). In the revised model marine $\delta^{18}O$ and continental feedback are varied with latitude.

METHODS

Proxy Data

The premise of using pedogenic carbonates as a proxy for the oxygen isotopic composition of precipitation stems from the recognition that exposure surface interaction with meteoric water results in calcite with narrow $\delta^{18}O$ compositions that reflect the oxygen isotopic composition of meteoric water and variable $\delta^{13}C$ compositions that are the result of the original parent rock carbon compositions and soil CO_2 compositions (Allen and Matthews, 1977; Lohmann, 1988). Plotting these values in $\delta^{18}O$ vs. $\delta^{13}C$ space defines vertical trends called meteoric calcite lines

(MCLs) (Lohmann, 1988), which were also recognized in pedogenic sphaerosiderites by Ludvigson et al. (1998) and termed meteoric sphaerosiderite lines (MSLs).

The majority of the data comes from American northern hemisphere localities. Mid to high latitude data was presented by White et al. (2001) and Ufnar et al. (2002) and consists of sphaerosiderite data from Aptian-Albian wetland or seasonally saturated soils from the Dakota Formation of Iowa, Nebraska, Kansas, and Utah, U.S.A.; the Swan River Formation of Manitoba and Saskatchewan, Canada; the Mattagami Formation of Ontario, Canada; the Mannville Group of Alberta, Canada; the Boulder Creek Formation of British Colombia, Canada (Ufnar et al., 2001); the Paddy Member of the Peace River Formation of Alberta, Canada (Ufnar et al., 2005); and the Nanushuk Formation of Alaska, U.S.A. (Figure 1). Pedogenic calcites were sampled from the Cedar Mountain Formation of Utah, U.S A., and were presented by Ludvigson et al., (2003). Ludvigson et al. (2004) presented data from paleosols and exposure surfaces of the Antlers Formation of Oklahoma, U.S.A., and the Glen Rose and Walnut Formations of Texas, U.S.A. Suarez et al. (2009) reported isotopic data from exposure surfaces and paleosols from the Tlayua Formation in Puebla, Mexico. Equatorial data comes from sphaerosiderite-bearing paleosols from coastal wetland deposits of the Caballos Formation in the Upper Magdalena Valley of Colombia, which provides our only southern hemisphere locality (Chapter 3).

Model Description

The original model of Ufnar et al. (2002) attempted to recreate the precipitation and evaporation fluxes that would simulate the empirical siderite oxygen

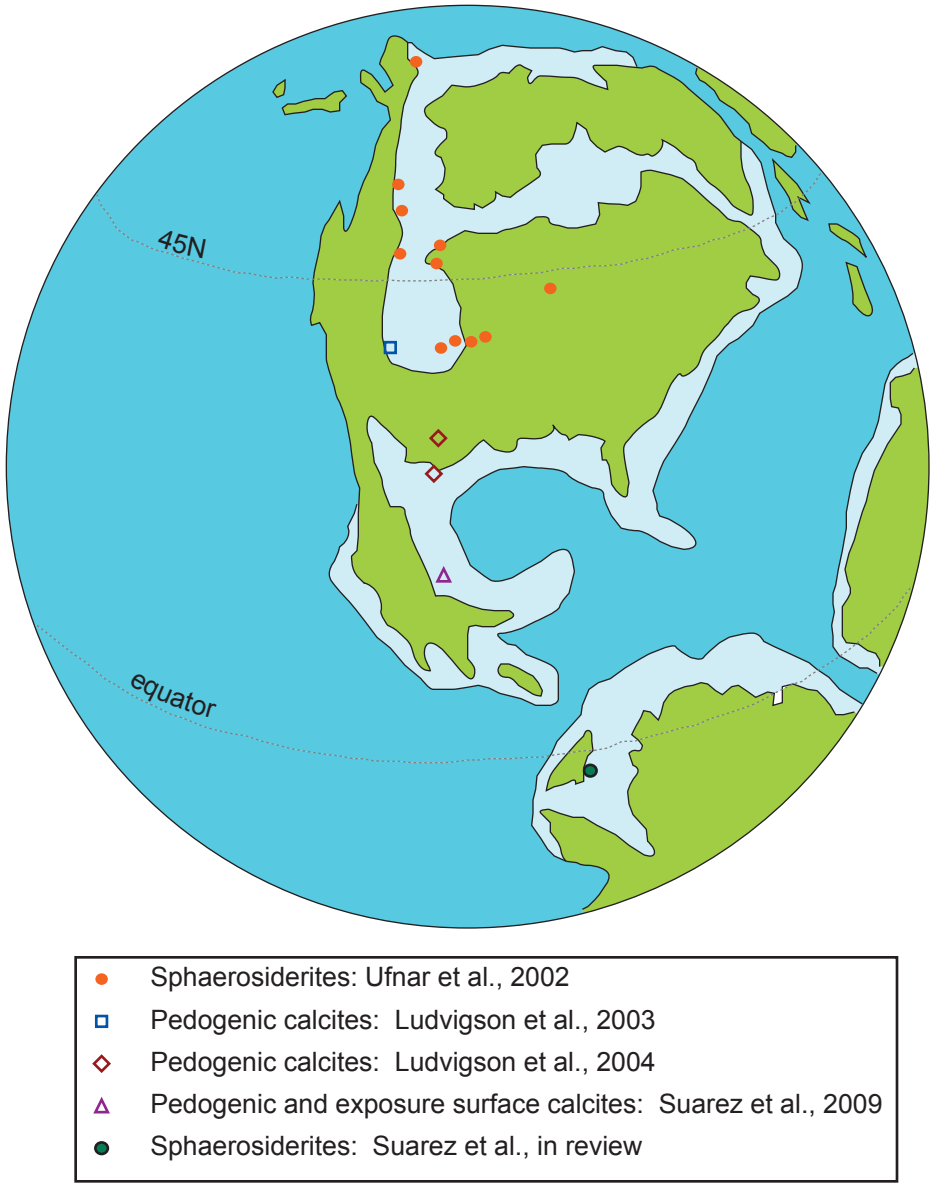

Figure 1—Global paleogeographic reconstruction for the mid-Cretaceous (105 Ma) showing the distribution of carbonate data localities. Sphaerosiderite-bearing localities are marked by solid symbols. Calcite-bearing localities are marked by open symbols. Paleogeographic reconstruction from Dr. Ron Blakey, Northern Arizona University.

isotopic compositions. The revised model also uses Stella® System Modeling software (version 9). Precipitation and evaporation fluxes along with relative humidity are graphical inputs that can be changed based on latitude. Readers are referred to Ufnar et al. (2002) for a description of the basic mass balance model, however, improvements to the model for this study warrant further explanation.

First, by including subtropical data from calcites, a different means of matching modeled data to empirical data was needed. To do this the oxygen isotopic composition of waters (presented relative to Standard Mean Ocean Water) precipitating the pedogenic carbonates were calculated from respective temperature-dependant fractionation factors (Friedman and O'Neil, 1977 for calcite and Carothers et al., 1988 for siderite). As in Ufnar et al. (2002) the model functionality was initially tested by simulation of a modern data set. While Ufnar et al. (2002) utilized theoretical sphaerosiderite $\delta^{18}O$ compositions derived from precipitation $\delta^{18}O$ values reported in Rosanzki et al (1993), this study uses the latitudinal precipitation $\delta^{18}O$ gradient directly from the same study.

For the Cretaceous models we tested the range of hypothesized temperatures for the Cretaceous (Barron, 1983; Wolfe and Upchurch, 1987; Spicer and Corfield, 1992; Poulsen et al., 1999a). These temperature gradients were used in combination with the above temperature-dependant fractionation factors to determine latitudinal gradients for the oxygen isotopic composition of groundwater (Table 1). The $\delta^{18}O$ composition of groundwater approximates the composition of precipitation (Lohmann, 1988) and, thus, the goal is to match the modeled rain compositions with

Table 1. Temperature gradients and corresponding groundwater gradients utilized in the mass balance model

	Temperature	$\delta^{18}O$ groundwater
Modern Rozanski et al., 1993	$= -0.003 \bullet lat^2 - 0.2514 \bullet lat + 30.113$	$= -0.003 \bullet lat^2 + 0.0595 \bullet lat - 3.699$
Leaf physiognomy Wolfe and Upchurch, 1987; Spicer and Corfield, 1992	$= -0.0006 \bullet lat^2 - 0.2025 \bullet lat + 30.25$	$= -0.004 \bullet lat^2 + 0.0523 \bullet lat - 4.154$
Cool Cretaceous Barron, 1983	$= -0.004 \bullet lat^2 - 0.0586 \bullet lat + 25.662$	$= -0.005 \bullet lat^2 + 0.0854 \bullet lat - 5.065$
Warm Cretaceous Barron, 1983	$= -0.003 \bullet lat^2 + 0.0538 \bullet lat + 28.534$	$= -0.004 \bullet lat^2 + 0.1015 \bullet lat - 4.372$
Western Interior Seaway-Eastern Margin Poulsen et al., 1999a	$= -0.002 \bullet lat^2 - 0.4356 \bullet lat + 36.273$	$= -0.005 \bullet lat^2 + 0.0181 \bullet lat - 2.988$

the groundwater compositions calculated from siderites and calcites. In addition, the mean oxygen isotopic compositions of groundwater are used as the compositions of water fed back from the continents. If we extrapolate to the equator using the regression presented by Ufnar et al. (2002) for the compiled latitudinal sphaerosiderite data, a much heavier tropical oxygen isotopic composition is calculated than that obtained from the empirical data presented by Ludvigson et al. (2004), Suarez et al. (2009), and in Chapter 3. It is evident that low latitude data are necessary to better constrain our model (Figure 2).

The original mass balance model traced the evolution of an air mass isotopic composition and that of resultant precipitation as it traveled from the equator to pole. Along its trajectory the air mass loses water vapor through precipitation, and is replenished via evaporation either from the ocean or both ocean and land (Figure 3). A significant modification in the new model is the addition of a westward travel path along the subtropical region. This westward travel path is more realistic than a strict equator to pole trajectory because it accounts for the westward airflow that characterizes the trade winds. The model allows the user to select the latitude along which the air mass travels westward as well as the distance traveled by the air mass before it flows north toward the pole or south toward the equator.

Lastly, the revised model allows for latitudinal changes in the oxygen isotopic composition of seawater, and for changes in the fraction of continental freshwater feedback. These two variables are also included as graphical inputs. Latitudinally variable $\delta^{18}O$ of seawater, rather than a constant -1.2‰ VSMOW, is consistent with

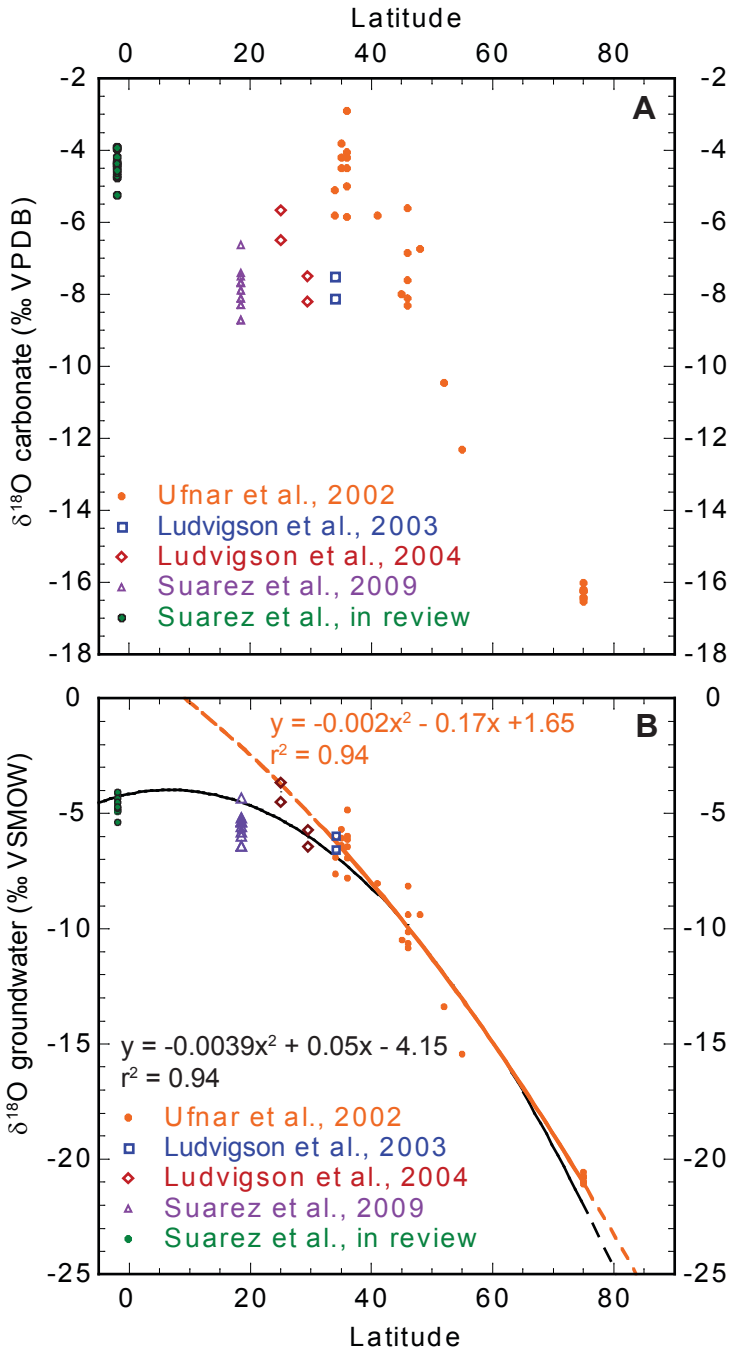

Figure 2—$\delta^{18}O$ of carbonate and groundwater data utilized in the mass balance model. A) Latitudinal distribution of carbonate data. Calcite data is shown as open symbols and sphaerosiderite data is shown as closed symbols. B) $\delta^{18}O$ of groundwater latitudinal gradient derived from carbonate data in (A) using temperature dependent fractionation factors for calcite from water and siderite from water. Temperature was determined based on leaf physiognomy data from Wolfe and Upchurch (1987) and compiled by Spicer and Corfield (1992).

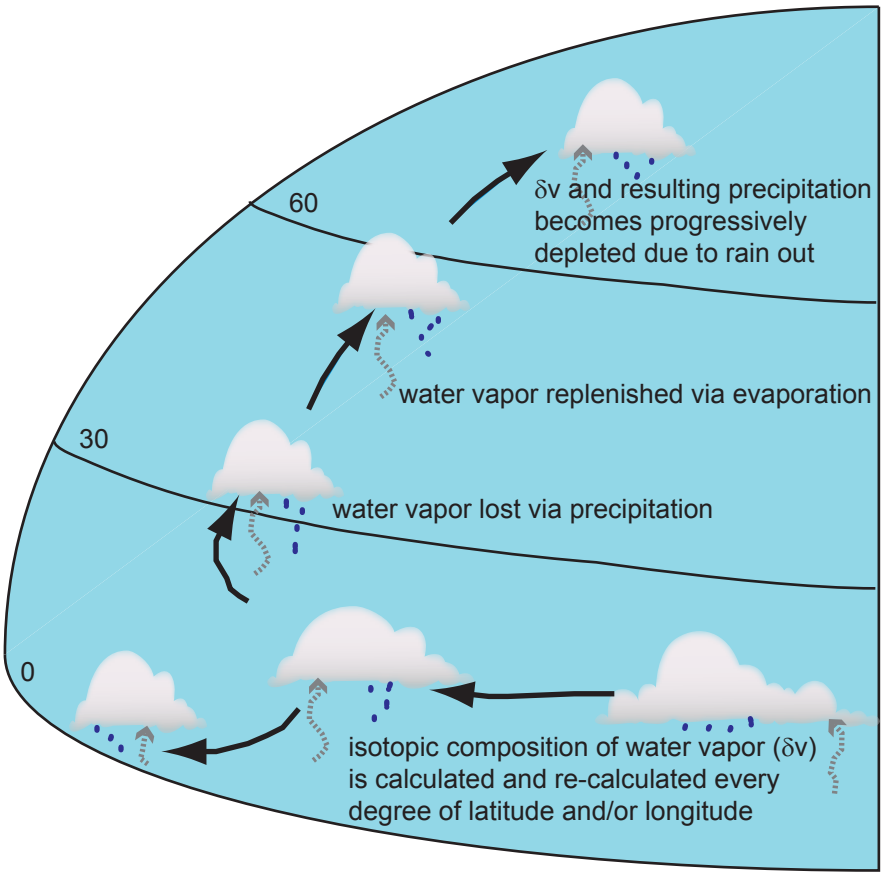

Figure 3—Conceptual illustration of the mass balance model. As the model progresses for each step the oxygen isotopic composition of water vapor is calculated based on inputs defined by the user that change latitudinally. Precipitation removes water from the air mass and evaporation replenishes it. To simplify the model precipitation and evaporation are set as dimensionless fluxes. The oxygen isotopic composition of water vapor is determined by the depletion due to precipitation and the composition of water replenishing the air mass through evaporation.

the geologic data that suggest evaporative conditions in the tropics (Woo et al., 1992; Johnson et al., 1996) and freshwater input at northerly reaches of the Western Interior Seaway (Hay and DeConto, 1999; Poulsen et al., 1999b; Huber et al., 2002). In the original modeling continental freshwater feedback was used in a scenario that maintained a constant 40% feedback over the entire latitudinal range, regardless of the presence of landmass. This revised model allows for user defined variations over the full latitudinal range.

MODEL CALIBRATION

As in the Ufnar et al. (2002) study, the model was first calibrated to match precipitation $\delta^{18}O$ compositions with those reported from International Atomic Energy Association/ World Meteorological Organization (IAEA/WMO) stations (Rozanski et al., 1993). These data were filtered to include only coastal stations less than 300 m in elevation to eliminate significant altitude and continental effects. This is consistent with the hypothesized depositional settings of the Cretaceous pedogenic data. The temperature gradient used in the modern model was also derived from Rozanski et al. (1993). The model was started at 10°N latitude and the air mass was tracked west for 50° before deflecting north or south. This distance was chosen because it is approximates the longitudinal distance that modern storm tracks take as they originate off the coast of Africa. The initial isotopic composition of the water vapor in the air mass was set at -10.50 ‰ VSMOW which is based on observational data presented in Craig and Gordon (1965) for mast height vapor compositions. The

$\delta^{18}O$ of seawater was defined based on a global gridded data set presented in LeGrande and Schmidt (2006). Latitudinal relative humidity variations were set according to inputs of the original Ufnar et al. (2002) model and adjusted where necessary. Peak continental feedback was set to reflect the peak percentage of land mass distribution at approximately 60°N (Barron et al., 1989). The peak continental feedback was kept low (19%) because we attempt to simulate coastal rain compositions, and it has been suggested that continental feedback affects the oxygen isotopic compositions of precipitation to a greater extent much farther inland (Nijitchoua, 1999).

The primary adjustments of the model to match the observed precipitation compositions were those made to precipitation and evaporation fluxes. Precipitation flux variations attempted to simulate the modern precipitation distributions with a precipitation high in the tropics, a low in the subtropics, a secondary peak in precipitation in the mid-latitudes, and low precipitation in the polar regions. The peak precipitation flux for the model occurs at 6°N latitude, where observational data of Alder et al. (2003) indicate peak precipitation rate occurs. Likewise, the distribution of evaporation fluxes attempted to reflect estimated evaporation rates in which evaporation is high in the tropics with a peak between approximately 20° and 30° and then a significant decline poleward. In attempting to match the observed rain composition data, it was necessary to increase the evaporation flux over that of the precipitation flux between 0 and 10°N. This is a reasonable modification because despite high amounts of precipitation in the tropics, high amounts of evaporation are

necessary to sustain the water vapor in the air mass. Using these parameters, the model was able to reproduce observational precipitation compositions within ± 0.5‰ VSMOW between 4°N and 90°N and within -0.6‰ VSMOW between 0 and 3°N The model produces rain compositions slightly too light between these latitudes. The input parameters used to reproduce the observed $\delta^{18}O$ of modern precipitation are graphed and summarized in Figure 4.

MODEL RESULTS

After testing model functionality using the modern oxygen isotopic compositions of precipitation, a variety of model scenarios were run using four different Cretaceous latitudinal temperature gradients. A Cretaceous temperature gradient based on leaf physiognomy data of Wolf and Upchurch (1987) and Spicer and Corfield (1992) has been used in previous data presented by our research group. We favor this temperature gradient because it is based on empirical paleoclimatic data rather than modeled data, and it is representative of a terrestrial-based temperature proxy. The model was also run with warm and cool Cretaceous temperature gradients presented by Barron (1983), and the model-derived Western Interior Basin eastern margin temperature gradient generated by Poulsen et al. (1999a).

Cretaceous models were started at 5°N rather than 10°N because it has been suggested that the seasonal migration of the Cretaceous ITCZ was in a more southerly position than the modern ITCZ (Hay and DeConto, 1999). The modeled air mass was tracked west for 50° before it deflected either to the north or south. The initial $\delta^{18}O$

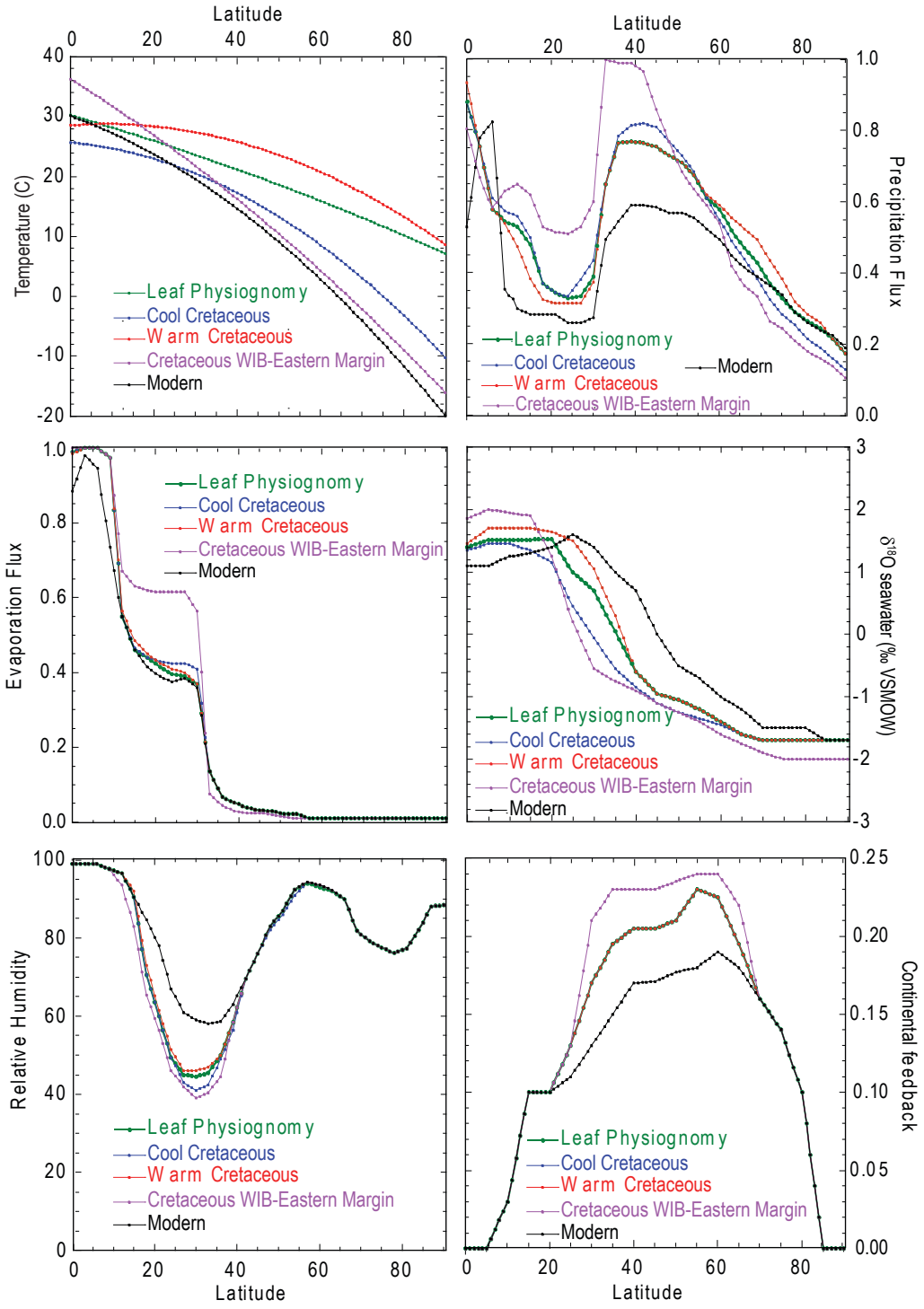

Figure 4—Graphical inputs for the mass balance model that produced precipitation compositions that closely match empirically derived compositions.

of the water vapor in the air mass (Table 2) for each temperature gradient model was calculated based on an average seawater composition of -1.2‰ VSMOW (Poulsen et al., 2007), the temperature at 5°N, and kinetic effects due to relative humidity (Gonfiantini, 1986). While the average oxygen isotopic composition of sea water for the ice-free mid-Cretaceous has been estimated to be -1.2‰ (Poulsen et al., 2007), Woo et al. (1992) suggested that the salinity and oxygen isotopic composition of seawater was elevated in what is now the Gulf of Mexico. Using the most enriched $\delta^{18}O$ values of calcite presented by Woo et al. (1992), we calculate that the heaviest $\delta^{18}O$ values of seawater were as high as 2‰ (VSMOW). In the northern hemisphere where freshwater runoff was high seawater could have been depleted to as low as -4‰ VSMOW (Woo et al., 1992; Hay and Deconto, 1999; Poulsen et al., 1999b; Huber et al., 2002). Using these constraints, the graphical inputs were adjusted to produce modeled rain compositions that were within ± 0.5‰ VSMOW of empirically-derived Cretaceous groundwater compositions (Figure 4 and 5). Precipitation fluxes for the simulations for Cretaceous temperature gradients are generally greater than the modern precipitation flux, with the exception of (1) a small area between 3 and 8°N, (2) the high latitudes when utilizing the Poulsen et al. (1999a) temperature gradient scenario, and (3) the high latitudes when utilizing the Barron (1983) cool Cretaceous scenario. Evaporation fluxes are also greater with the exception of slightly lower evaporation flux for the Poulsen et al. (1999a) temperature gradient scenario between about 30° and 55°N. Because our carbonates were obtained from low elevation fluvial systems, evaporative feedback from the landmass

Table 2. Initial isotopic compositions of water vapor

Temperature gradient	$\delta^{18}O_v$ =
Modern	-10.50‰
Leaf physiognomy	-10.53‰
Cool Cretaceous	-10.84‰
Warm Cretaceous	-10.60‰
Western Interior Seaway-Eastern Margin	-10.15‰

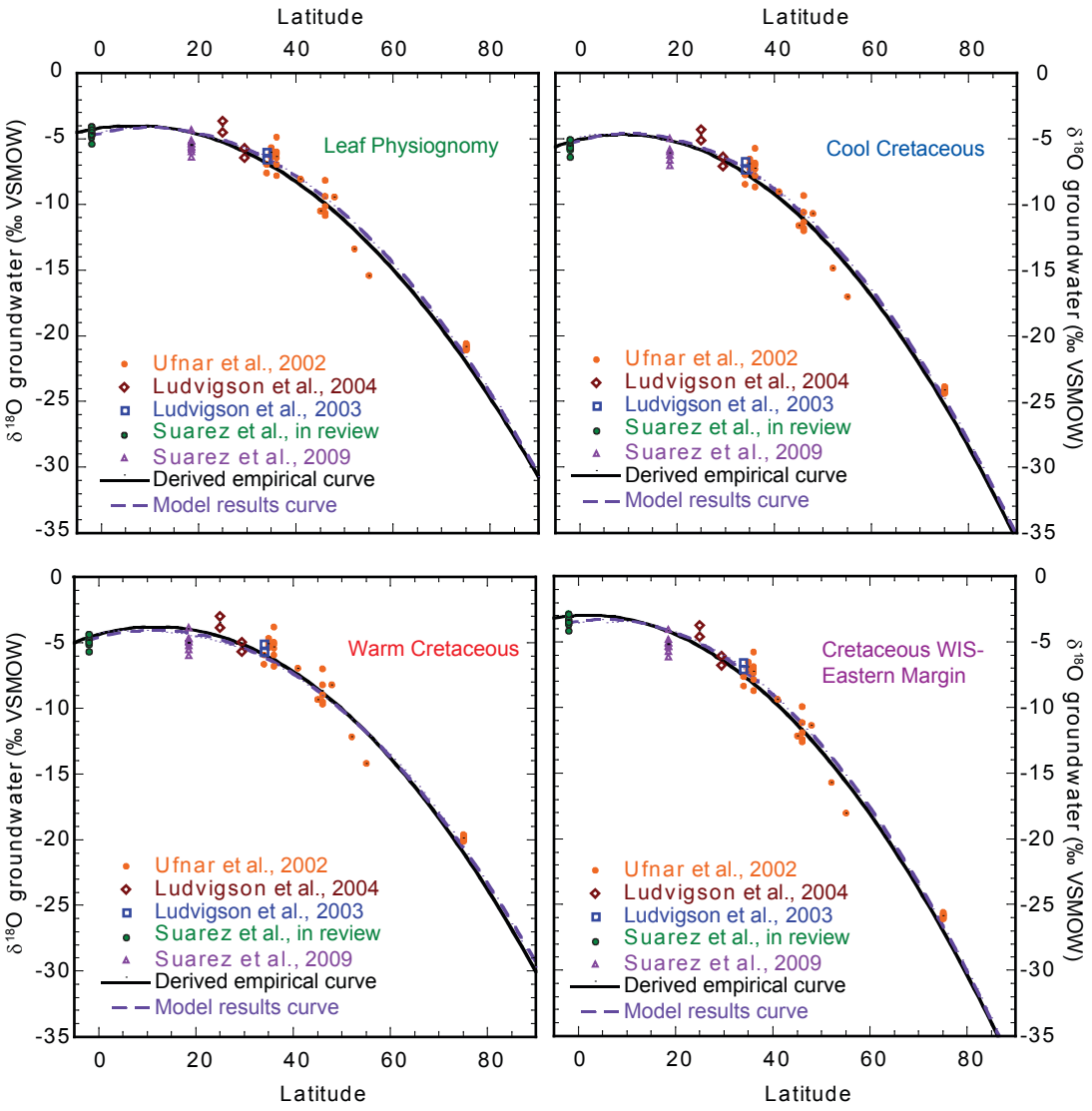

Figure 5—Empirically-derived $\delta^{18}O$ of groundwater gradients for four different latitudinal temperature gradients scenarios compared with model-produced precipitation compositions (dashed-line).

to the airmass must be considered. Vegetation, paleosols, and sedimentology hypothesized for the mid-latitudes suggest terrestrial evaporative feedback similar to that of modern rainforest systems.

For all scenarios, the $\delta^{18}O$ of seawater was enriched in the low latitudes (1.45‰ to 2.00‰) and depleted in the high latitudes (-2.00‰ to -1.70‰). The temperature equation of Poulsen et al. (1999a) requires the most extreme changes in $\delta^{18}O$ values with seawater composition of 2‰ VSMOW in the low latitudes and -2‰ VSMOW in the high latitudes.

Relative humidity must be significantly decreased between 20°N and 40°N. This was required because the model would otherwise produce precipitation $\delta^{18}O$ values that are too enriched relative to the empirically derived precipitation compositions, requiring high precipitation rates to deplete the air mass compositions. However, the sedimentologic evidence (pedogenic calcites and evaporites) indicates precipitation deficits and reduced precipitation rates. Reducing relative humidity causes a greater kinetic effect on the $\delta^{18}O$ of atmospheric moisture during evaporation, resulting in depletion of the oxygen isotopic composition of subtropical rainwater.

SENSITIVITY AND ALTERNATE SCENARIOS

A number of sensitivity tests were presented in the original model iterations by Ufnar et al. (2002). In the sensitivity analysis, changes to the seawater composition, continental water composition, relative humidity, evaporation flux, and

precipitation flux were made to determine the relative impact of each of these variables on model results. These tests indicated that the model is primarily sensitive to changes in precipitation and evaporation flux. The model is also somewhat sensitive to changes in the isotopic composition of continental water as well as relative humidity.

Sensitivity of the revised model to seawater composition is re-evaluated because unlike the previous model, the seawater composition is changed to reflect hypothesized compositions of seawater (Woo et al., 1992; Johnson et al., 1996; Poulsen et al., 1999b; Huber et al., 2002). For these sensitivity tests, the model scenario tuned using the leaf physiognomy temperature gradient was changed to reflect (a) a constant seawater $\delta^{18}O$ composition of -1.2‰ VSMOW and b) a constant heavy tropical seawater $\delta^{18}O$ composition of 1.4‰ VSMOW with a constant light Western Interior Seaway (WIS) $\delta^{18}O$ value of -1.2‰ VSMOW (Figure 6). A constant -1.2‰ VSMOW of seawater causes precipitation to become lighter over the full range of latitudes, but especially in the low latitudes. A heavy tropical composition with a constant light Western Interior Seaway has little effect, and precipitation compositions remain within ±0.5‰ of the derived empirical data. Changes to graphical inputs that are required to simulate the derived empirical data with the changes made to seawater compositions are shown in Figure 7. To balance the scenario with a constant -1.2‰ VSMOW seawater composition, precipitation flux must be decreased between 0 and 12°N increased significantly north of 12° to values that are inconsistent with geologic and paleontologic data.

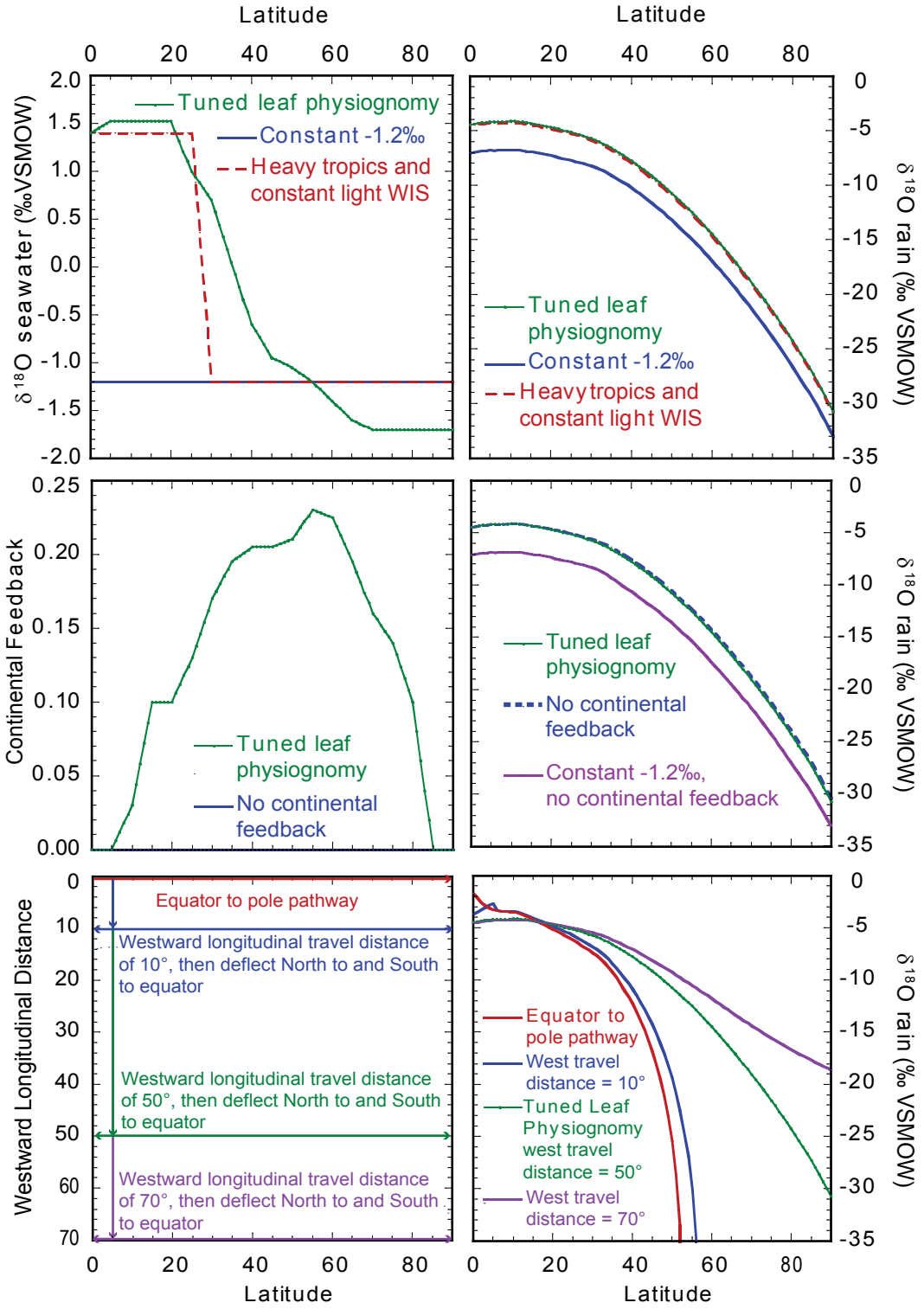

Figure 6—Sensitivity tests of the model. The graphs in the left column indicate changes to input parameters. The graphs in the right column are the corresponding changes in modeled $\delta^{18}O$ of precipitation to the change in input parameters.

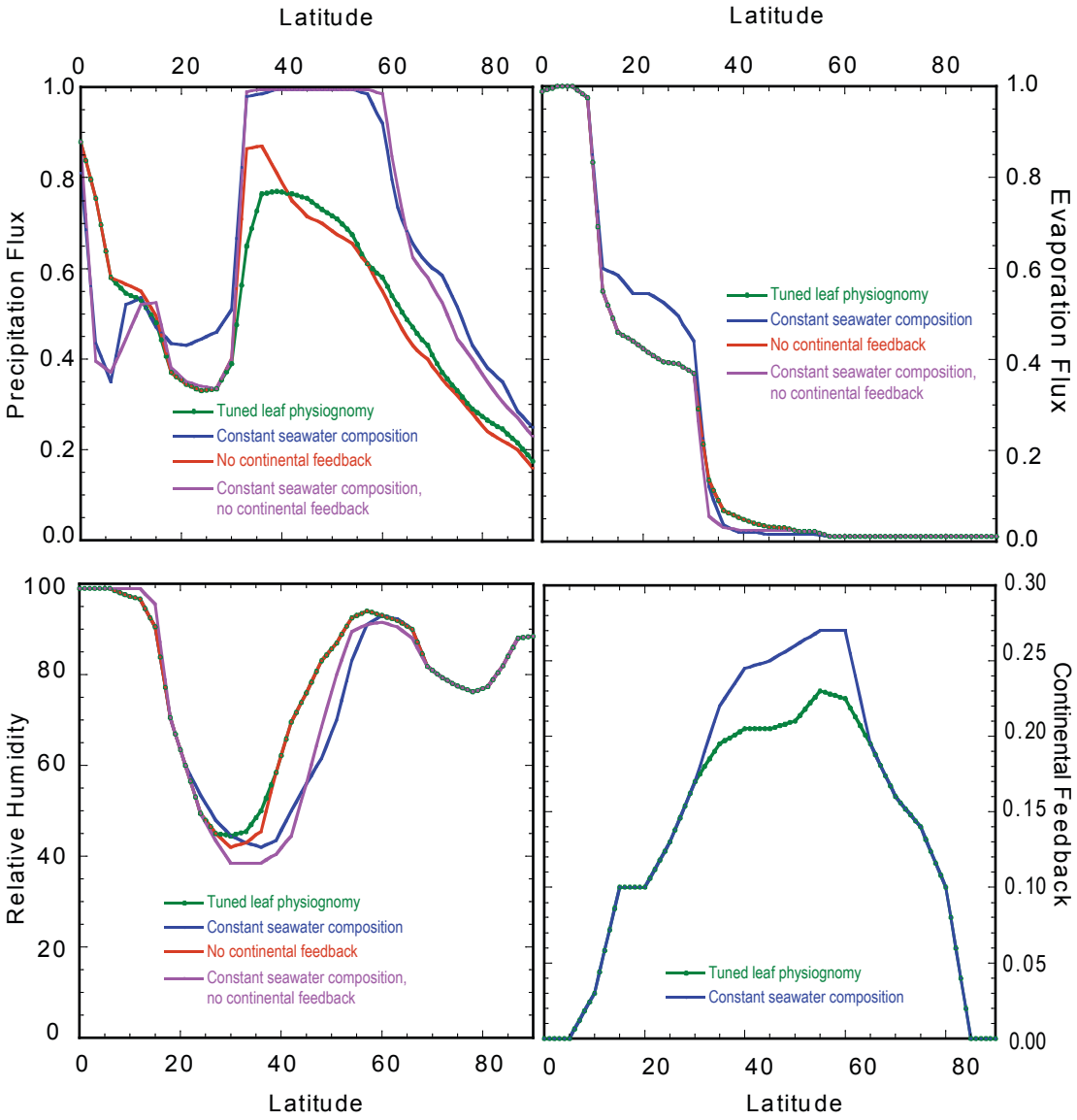

Figure 7—Input parameters necessary to produce modeled precipitation compositions for alternative scenarios including a constant -1.2‰ VSMOW seawater composition, no continental feedback, and a combined no continental feedback with constant seawater composition simulation.

A zero continental feedback scenario was run to test the impact of the continental feedback on the isotopic composition of precipitation. Eliminating continental feedback has a very minor effect on the $\delta^{18}O$ of precipitation. The lack of continental feedback causes a maximum 0.8‰ enrichment, which requires a slight increase in precipitation flux to match the empirical data (Figure 7). A scenario with no continental feedback and a constant -1.2‰ VSMOW seawater composition results in precipitation compositions that are lighter over the full range of latitudes.

A significant change to the revised model is the addition of westward vapor transport in the tropics, which is more realistic than a strictly equator-to-pole track that was presented in Ufnar et al. (2002). For the tuned leaf physiognomy scenario, the air mass traveled westward for 50° before diverting north or south as in the modern simulation. This distance it is kept the same as in the modern calibration runs. Changing the westward travel distance has significant effects on modeled rain compositions. With longer longitudinal travel distance, the air mass is maintained by high evaporation of enriched seawater, so that a westward distance of 70° results in $\delta^{18}O$ precipitation values that are more enriched than in the tuned leaf physiognomy model. With a shorter westward travel distance (10°) or only a simple equator-to-pole transect, the water vapor in the air mass is exhausted and the rain compositions become too depleted. Another effect of the westward air mass track is to stabilize the oxygen isotopic composition of precipitation. During the model run spin-up, initial precipitation compositions are almost always too heavy and become lighter as the run progresses to the point that $\delta^{18}O$ values become more stable. With a strict equator-to-

pole transect, the precipitation composition fails to stabilize before becoming too depleted. This spin-up problem in the tropics is common to all of the Ufnar et al. (2002) simulations, in which the oxygen isotopic compositions of siderite have a short, but steep depletion between 0 and 10°N before becoming more stable.

PRECIPITATION RATES

To provide more useful estimates for comparisons, Ufnar et al. (2002) utilized temperature-dependent saturation vapor density curves (Craig and Fritz, 1997) and the following algebraic equations to calculate precipitation rates for the four Cretaceous temperature gradient models:

$$VD = 0.002 \bullet T^3 + 0.0111 \bullet T^2 + 0.321 \bullet T + 4.8$$
$$\Delta VD_{k-m} = (VD_k - VD_m)/(VD_m)$$
$$H_m = P_m / F_m$$
$$H_k = (1 + \Delta VD_{k-m}) \bullet H_m$$
$$P_k = H_k \bullet F_k$$
$$P_k = (1 + \Delta VD_{k-m}) \bullet (P_m / F_m) \bullet F_k$$

where VD = saturation vapor density (g/m^3), T = temperature in degrees Celsius, P = precipitation rate, F = precipitation flux, H = height of an infinitesimally small water column, ΔVD is the change in potential vapor density, and subscripts m refers to modern and k to Cretaceous. It is assumed that the fractional change in vapor density due to temperature change is proportional to the change in amount of precipitation. In order to solve for the Cretaceous precipitation rate (P_k), modern zonal mean average precipitation rates (P_m) calculated from combined rain gauge and satellite data from1979 to 2003 presented by Alder et al. (2003) were used.

The precipitation rates (Figure 8) calculated for each of the Cretaceous temperature gradient scenarios are greater than modern precipitation rates with the exception of a narrow range between 2°N and 8°N. In addition, north of 66°N the precipitation rate calculated using the temperature gradient scenario of Poulsen et al. (1999a) for the eastern margin of the North American Western Interior Seaway (WIS), is slightly lower than the modern precipitation rate. For all but the warm Cretaceous temperature gradient (Barron, 1983) scenario, the peak precipitation occurs at 9°N. In the warm Cretaceous scenario maximum precipitation is manifested as a broad peak at ~ 62°N. The lowest precipitation rates occur in the subtropics at 20°N to 21°N, however, these rates are still greater than the modern precipitation rates. Peaks in precipitation (at the equator, at 9°N, and between about 45°N and 46°N) vary significantly between the four temperature gradient scenarios. For example, at 55°N, the temperature gradient scenario of Poulsen et al. (1999a) yields an estimated precipitation rate of 1090 mm/year, the cool Cretaceous scenario of Barron (1983) yields an estimated precipitation rate of 1496 mm/year, the leaf physiognomy scenario yields an estimated precipitation rate of 2146 mm/year, and the warm Cretaceous scenario of Barron (1983) yields an estimated precipitation rate of 2881 mm/year. The total range in estimated precipitation rates at this latitude is 1791 mm/year.

The precipitation rate estimates of this revised model are lower than the estimates of Ufnar et al. (2002). For example, at 45°N, the leaf physiognomy temperature gradient of the original model produced a precipitation rate of 2618

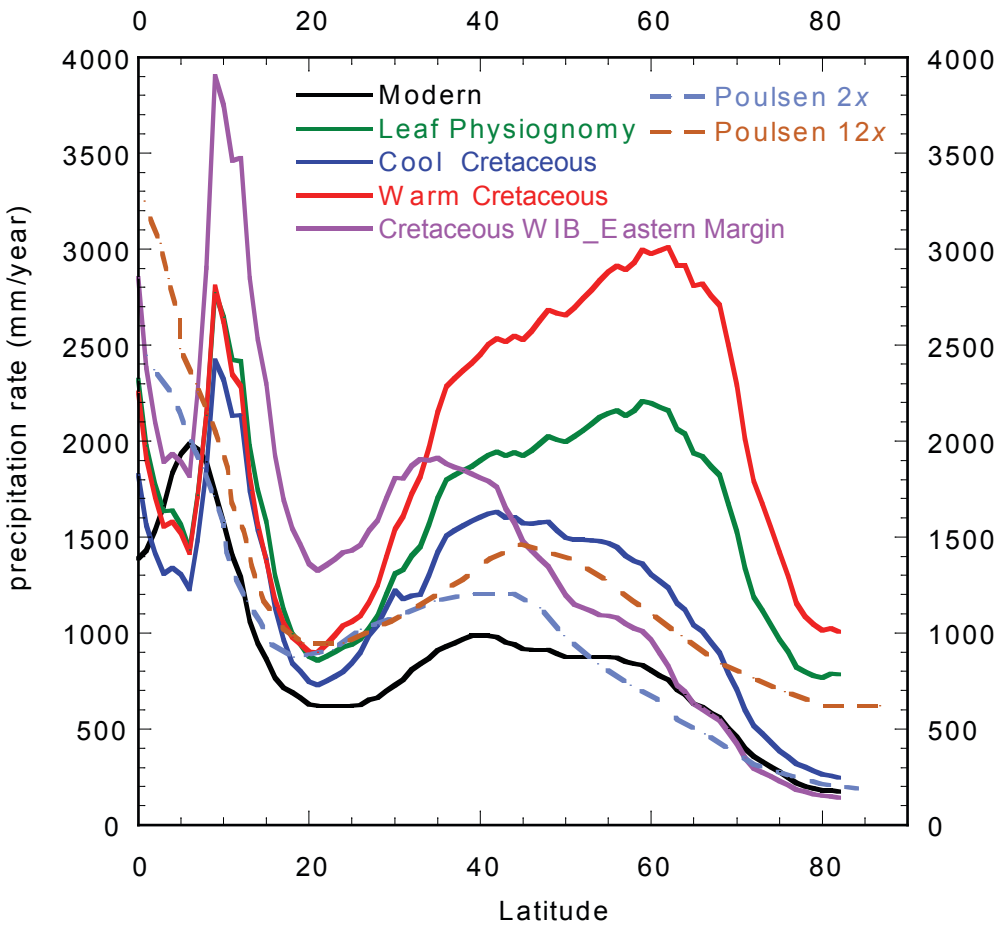

Figure 8—Annual precipitation rates calculated for each temperature gradient scenario. Dashed lines are precipitation rates produced by GENESIS GCM simulations based on 2*x* modern CO2 concentrations and 12*x* modern CO2 concentrations. These rates are based on data presented in Poulsen et al. (2007).

mm/year, whereas the revised model indicates a precipitation rate of 1922 mm/year. Precipitation rates for the other temperature gradient models are also lower. Recently, Poulsen et al. (2007) generated precipitation rates and oxygen isotopic compositions using the GENESIS atmospheric general circulation model (GCM) for various CO_2 concentrations. Precipitation rates increased with increased CO_2 concentrations. The lowest (2*x* modern CO_2) and highest (12*x* modern CO_2) precipitation rate curves for these model simulations are also depicted in Figure 8. Their precipitation rate patterns are different than those produced by the mass balance model. The GCM precipitation rates are symmetrical about the equator with peak precipitation at the equator. Like the mass balance model results, the low in precipitation rates occurs at approximately 20°N to 21° N and a secondary peak in precipitation occurs in the mid-latitudes. Global precipitation rates for the mass balance models and for the GCM simulations of 2*x* and *12x* modern CO_2 concentrations are summarized in Table 3. The leaf physiognomy scenario and warm Cretaceous (Barron, 1983) scenario suggest precipitation rates that are greater than the extreme *12x* CO_2 simulation. The cool Cretaceous scenario is less than the least extreme (*2x* CO_2) model output. The WIS eastern margin scenario (Poulsen et al., 1999a) produces global precipitation rates that are slightly greater than the *12x* CO_2 simulation.

Table 3. Average global precipitation rates

	Precipitation rate (mm/year)
Modern (Alder et al., 2003)	851
Leaf physiognomy (this study)	1629
Cool Cretaceous (this study)	1198
Warm Cretaceous (this study)	2005
Western Interior Seaway-Eastern Margin (this study)	1428
2X modern CO2 simulation (Poulsen et al., 2007)	1241
12X modern CO2 simulation (Poulsen et al., 2007)	1424

DISCUSSION

The mass balance model presented here, while not as complex as a GCM, provides important insights into the variables that need to be considered for improvements of climate models. An obvious variable that receives attention in climate models is that of temperature. The different temperature gradients utilized in the mass balance models result in very different precipitation rates, suggesting that current uncertainties concerning Cretaceous temperatures must be reconciled in order to improve precipitation estimates. Recent advances in temperature proxies such as clumped isotope methods (Eiler et al., 2007) and utilization of organic molecules (Schouten et al., 2003) may aid in providing better constrained paleotemperature gradients.

Sensitivity testing indicates that the origin and pathway that air masses travel significantly affects $\delta^{18}O$ of precipitation values. As the water vapor in the air mass evolves during westward transport over isotopically-enriched seawater, the water vapor composition significantly affects the precipitation compositions when the air mass eventually deflects either north or south. In modeling air mass pathways, the mass balance model lacks the sophistication of a general circulation model, which can simulate air circulation better than the mass balance model. A related variable is that of paleogeography and paleotopography. Barron et al. (1989) indicated that the distribution of landmasses plays a significant role in the availability of moisture for the atmosphere as well as the distribution of rainfall. In addition, differences in heating of land compared to sea affects air circulation. In the high mountain

GENESIS GCM simulation of, Poulsen et al. (2007), topography played a significant role in the oxygen isotopic composition of simulated rainfall in a site bordering the ancestral Brooks Range in North Slope Alaska. The increased topography caused depletion of compositions due to altitude and rainout effects as air masses travelled across high mountains. Poulsen et al. (2007) argued that these orographic effects caused the local isotopic depletion of sphaerosiderite compositions and not the zonally increased rainout effects on polar paleoprecipitation of the global hydrologic cycle. In first presenting the Alaskan data from the Cretaceous Nanushuk Group, Ufnar et al. (2004) noted similarities between their estimates of depleted polar Cretaceous paleoprecipitation to those presented by Ferguson et al. (1999) from polar sites of southern Australia. Because all sphaerosiderites sampled by our research group were precipitated in interfluvial settings of coastal environments we suggest that groundwater was dominated by local coastal paleoprecipitation, as opposed to regional fluvial runoff which is influenced by topographic effects (Dutton et al., 2005; Phillips et al., 2007; Chapter 3). Having established this however, topography is an important factor in the distribution of oxygen isotopic composition of precipitation today (Bowen and Wilkinson, 2002), and was likely an important factor in the Cretaceous. There is no doubt that greater spatial sampling resolution of continental oxygen isotopic composition proxies would help elucidate the importance of local topographic or more regional "catchment effects" (Dutton et al., 2005) during the Cretaceous.

Large reduction of relative humidity was necessary for the Cretaceous simulations in the subtropics in order to cause sufficient depletion without increasing precipitation over evaporation flux. The resulting contrast in humidity along with overall increased water vapor content, suggest that these conditions allowed for a more efficient poleward latent heat transport during the Cretaceous (Hay and DeConto, 1999).

Sensitivity testing presented in Ufnar et al. (2002) as well as those presented here suggest that the oxygen isotopic composition of seawater, particularly in the low latitudes, is an important factor to consider. It is probably unreasonable to model the Cretaceous hydrologic cycle with a constant -1.2‰ VSMOW seawater composition. Increased evaporation in the tropics and subtropics would have caused enrichment of seawater (Woo et al., 1992; Johnson et al., 1996; Poulsen et al., 1999b; Ziegler et al., 2003) to $\delta^{18}O$ values greater than the average -1.2‰ VSMOW. Conversely, isotopic compositions in the high latitudes were much lighter (as light as -4‰ VSMOW) as result of increased continental runoff, an effect of greater precipitation (Woo et al., 1992; Poulsen et al., 1999b; Huber et al., 2002). The more enriched isotopic composition of seawater in the tropics to subtropics was an important change in the mass model because, when modeled with a -1.2‰ VSMOW constant seawater composition, the $\delta^{18}O$ of precipitation became too light between 0 and 10°N and required a geologically unreasonable reduction in precipitation flux in the low latitudes.

CONCLUSIONS

Understanding the dynamics of the hydrologic cycle is an important aspect to providing insight into the global climate system. This revised mass balance model utilizes the oxygen isotopic composition of pedogenic carbonates as a proxy for the oxygen isotopic composition of precipitation. The model simulates discrete components of the hydrologic cycle that produced these compositions. This paper updates a previous version of a similar mass balance model by Ufnar et al. (2002) by adding new low latitude derived empirical data. The revised model more realistically simulates air mass origins and pathways. The model also provides for compositional changes with respect to latitude, and latitudinal variations in the $\delta^{18}O$ of seawater and continental feedback. Graphical inputs (precipitation flux, evaporation flux, seawater composition, relative humidity, and continental feedback) were successfully manipulated to produce modeled oxygen isotopic compositions of modern and mid-Cretaceous precipitation that are within ± 0.5‰ VSMOW of derived-empirical data.

Calculated global average precipitation rates are between 371 mm/year to 1154 mm/year greater than modern precipitation rates and provide further support to the hypothesis that the hydrologic cycle was more active during the mid-Cretaceous greenhouse climate. The precipitation rates calculated in this study are less than those reported from by Ufnar et al. (2002), but are generally greater than those presented by GENESIS GCM simulations of Poulsen et al. (2007). Sensitivity and alternative scenario tests indicate that persistent uncertainty in temperature gradients and the sites of origin and pathways of air masses greatly affect the $\delta^{18}O$ values of

precipitation. The oxygen isotopic compositions of seawater and relative humidity also affect the modeled precipitation $\delta^{18}O$ values. Greater constraints for these variables will significantly improve our ability to accurately model ancient and future hydrologic cycles.

REFERENCES

Alder, R. F., Huffmann, G. J., Chang, A., Ferraro, R., Xie, P., Janowiak, J., Rudolf, B., Schneider, U., Curtis, S., Bolvin, D., Gruber, A., Susskind, J., Arkin, P., Nelkin, E., 2003, The Version 2- Global Precipitation Climatology Project (GPCP) monthly precipitation analysis (1979-present): Journal of Hydrometeorology, v. 4, p. 1147-1167.

Allen, J. R., and Matthews, R.K., 1977, Carbon and oxygen isotopes as diagenetic and stratigraphic tools: Surface and subsurface data, Barbados, West Indies: Geology, v. 5, p. 16-20.

Barron, E. J., 1983, Warm equable Cretaceous, The nature of the problem: Earth Science Reviews, v. 19, p. 305-338.

Barron, E. J., Hay, W. W., and Thompson, S., 1989, The hydrologic cycle: A major variable during Earth History: Palaeogeography, Palaeoclimatology, Palaeoecology, v. 75, p. 157-174.

Bowen, G. J., and Wilkinson, B., 2002, Spatial distribution of d18o in meteoric precipitation: Geology, v. 30, no. 4, p. 315-318.

Carothers, W. W., Adami, L.H., Rosenbauer, R.J., 1988, Experimental oxygen isotope fractionation between siderite-water and phosphoric acid liberated CO_2-siderite: Geochimica et Cosmochimica Acta, v. 52, no. 10, p. 2445-2450.

Craig, H., Gordon, L. I., 1965, Deuterium and oxygen 18 variations in the ocean and the marine atmosphere, *in* Tongiorgi, E., ed., Stable isotopes in oceanographic

studies and paleotemperatures: Pisa, Consiglio Nazionale delle Ricerche Labratorio di Geologia Nucleare, 125 p.

Dutton, A., Wilkinson, B.H., Welker, J.M., Bowen, G.J., and K.C. Lohmann, 2005, Spatial distribution of seasonal variation in $^{18}O/^{16}O$ of modern precipitation and river water across the conterminous USA: Hydrological Processes, v. 19, p. 4121-4146.

Eiler, J. M., 2007, "Clumped-isotope" geochemistry--The study of naturally-occuring, multiply substituting isotopologues: Earth and Planetary Science Letters, v. 262, p. 309-327.

Ferguson, K. M., Gregory, R.T., and Contantine, A., 1999, Lower Cretaceous (Aptian-Albian) secular changes in the oxygen and carbon isotope record from high paleolatitude,fluvial sediments, southeast Australia: Comparisons to the marine record, *in* Barrera, E., and Johnson, C.C., eds., Evolution of the Cretaceous ocean climate system: Boulder, Geological Society of America, Special Paper 332, p. 59-72.

Friedman, I., and O'Neil, J. R., 1977, Compilation of stable isotope fractionation factors of geochemical interest, *in* Fleisher, N. ed., Data of geochemistry. USGS Professional Paper 440-KK: Washington, D.C., 110 p.

Gonfiantini, R., 1986, Environmental isotopes in lake studies, *in* Fritz, P. a. F., J.-Ch., ed., Handbook of Environmental Isotope Geochemistry, Vol. 2, The Terrestrial Environment: Amsterdam, Elsevier, p. 113-168.

Hay, W. W. and DeConto, R.M., 1999, Comparison of modern and Late Cretaceous meridional energy transport and oceanology, *in* Barrera, E., and Johnson, C.C., eds., Evolution of the Cretaceous ocean-climate system: Boulder, Geological Society of Americica Special Paper 332, p. 283-300.

Huber, B. T., Norris, R. D., and MacLeod, K. G., 2002, Deep-sea paleotemperature record of extreme warmth during the Cretaceous: Geology, v. 30, p. 123-126.

Johnson, C. C., Barron, E. J., Kauffmann, E. G., Arthur, M. A., Fawcett, P. J., Yasuda, M. K., 1996, Middle Cretaceous reef collapse linked to ocean heat transport: Geology, v. 24, p. 376-380.

LeGrande, A. N., and Schmidt, G. A., 2006, Global gridded data set of the oxygen isotopic composition in seawater: Geophysical Research Letters, v. 33, p. L12604.

Lohmann, K. C., 1988, Geochemical patterns of meteoric diagenetic systems and their application to studies of paleokarst, *in* James, N. P., and Choquette, P.W., ed., Paleokarst: New York, Springer, p. 58-80.

Ludvigson, G., González, L.A., Metzger, R.A., Witzke, B.J., Brenner, R.L., Murillo, A.P., White, T.S., 1998, Meteoric sphaerosiderite lines and their use for paleohydrology and paleoclimatology: Geology, v. 26, no. 11, p. 1039-1042.

Ludvigson, G. A., González, L.A., Kirkland, J.I., and Joeckel, R.M, 2003, A mid-Cretaceous record of carbon isotope excursions in palustrine carbonates of the Cedar Mountain Formation of Utah: Marine-terrestrial correlations of Aptian-Albian oceanic anoxic events 1a, 1b, and 1d: The 3rd International

Limnogeology Congress, March 29-April 2, Tucson, Arizona, Abstract Volume, p. 169.

Ludvigson Greg, A., Ufnar David, F., González Luis, A., Carpenter Scott, J., Witzke Brian, J., Brenner Robert, L., Davis, J., 2004, Terrestrial paleoclimatology of the Mid-Cretaceous greenhouse; I, Cross-calibration of pedogenic siderite & calcite $\delta^{18}O$ proxies at the Hadley Cell boundary.; Geological Society of America, 2004 annual meeting: Abstracts with Programs Geological Society of America, v. 36, no. 5, p. 305.

Nijitchoua, R., 1999, Variations of the stable isotopic compositions of rainfall events from the Cameroon rainforest, Central Africa: Journal of Hydrology, v. 223, no. 1, p. 17-26.

Phillips, P., L. Jr., Ludvigson, G. A., Joeckel, R. M., González, L. A., Brenner, R. L., and Witzke, B. J., 2007, Sequence stratigraphic controls on synsedimentary cementation and preservation of dinosaur tracks; example from the Lower Cretaceous, (upper Albian) Dakota Formation, southeastern Nebraska, U.S.A: Palaeogeography, Palaeoclimatology, Palaeoecology, v. 246, no. 2-4, p. 367-389.

Poulsen, C. J., Barron, E.J., Johnson, C., Fawcett, P., , 1999a, Links between major climatic factors and regional oceanic circulation in the mid-Cretaceous, *in* Barrera, E., and Johnson, C.C., ed., Evolution of the Cretaceous Ocean-Climate system: Boulder, Geological Society of America, p. 73-90.

Poulsen, C. J., Barron, E.J., Peterson, W. H., Wilson, P. A., 1999b, A reinterpretation of mid-Cretaceous shallow water temperatures through model-data comparison: Paleoceanography, v. 14, p. 679-697.

Poulsen, C. J., Pollard, D., and White, T.S., 2007, General circulation model simulation of the $\delta^{18}O$ content of continental precipitation in the middle Cretaceous: a model-proxy comparison: Geology, v. 35, p. 199-202.

Rozanski, K., Araguas-Araguas, L., Gonfiantini, R. , 1993, Isotopic patterns in modern global precipitation, *in* Swart, P. K., Lohmann, K.C., McKenzie, J., Savin, S. , ed., Climate Change in Continental Isotope Records, AGU, p. 1-36.

Schouten, S., Hopmans, E. C., Forster, A., van Bruegal, Y., Kuypers, M. M. M., and Sinninghe Damste, J. S., 2003, Extremely high sea surface temperatures at low latitudes during the middle Cretaceous as revealed by archaeal membrane lipids: Geology, v. 31, p. 1069-1072.

Sorensen, A. C., 2002, Petrography and diagenesis of palustrine carbonate beds in the Early Cretaceous Cedar Mountain Formation, eastern Utah, *in* Ludvigson, G. A., González, L. A., Carpenter, S. J., Joeckel, R. M., and Kirkland, J. I., eds., Abstracts with Programs - Geological Society of America: United States, Geological Society of America (GSA) : Boulder, CO, United States, p. 17-18.

Spicer, R. A., and Corfield, R.M., 1992, A review of terrestrial and marine climates in the Cretaceous with implications for modelling the 'Greenhouse Earth': Geology Magazine, v. 2, p. 169-180.

Suarez, M. B., González, L. A., Ludvigson, G. A., Vega, F. J., and Alvarado-Ortega, J. , 2009, Isotopic composition of low-latitude paleoprecipitation during the Early Cretaceous: GSA Bulletin, v. 121, p. 1584-1595.

Ufnar, D. F., González, L.A., Ludvigson, G.A., Brenner, R.L., Witzke, B.J., 2001, Stratigraphic implications of meteoric sphaerosiderite $\delta^{18}O$ values in paleosols in the Cretaceous (Albian) Boulder Creek Formation, NE British Colombia Foothills, Canada: Journal of Sedimentary Research, v. 71, no. 6, p. 1017 - 1028.

-., 2002, The mid-Cretaceous water bearer: isotope mass balance quantification of the Albian hydrologic cycle: Palaeogeography, Palaeoclimatology, Palaeoecology, v. 188, p. 51-71.

-, 2004, Evidence for increased latent heat transport during the Cretaceous (Albian) greenhouse warming: Geology, v. 32, no. 12, p. 1049-1052.

Ufnar, D. F., Ludvigson, G. A., González, L. A., Brenner, R. L., Witzke, B. J., and Leckie, D. A. , 2005, Ancient landscape development in the Late Albian Western Canadian Foreland Basin: Journal of Sedimentary Research, v. 75, p. 984-996.

Wolfe, J. A., Upchurch, G.J.R., 1987, North American nonmarine climates and vegetation during the Late Cretaceous: Palaeogeography, Palaeoclimatology, Palaeoecology, v. 61, p. 31-77.

Woo, K. S., Anderson, T. F., Railsback, L. B., and Sandberg, P. A. , 1992, Oxygen isotopic evidence for high salinity surface seawater in the mid-Cretaceous

Gulf of Mexico: Implications for warm, saline deepwater formation: Paleoceanography, v. 7, p. 673-685.

Ziegler, A. M., Eshel, G., McAllister Rees, P., Rothfus, T. A., Rowley, D. B., Sunderlin, B., 2003, Tracing the tropics across land and sea: Permian to present: Lethia, v. 36, p. 227-254.

CHAPTER 5. CONCLUSIONS

The research presented in this dissertation provides new stable isotopic constraints from pedogenic carbonate compositions in the low latitudes and are utilized to improve mass-balance modeling of the Cretaceous hydrologic cycle. The addition of this data results in a more complete equator-to-pole proxy data set of the oxygen isotopic composition of precipitation.

Data from supratidal and paleosol deposits of the Tlayua Formation at ~ 18.5°N paleolatitude produced meteoric calcite lines that allowed estimation of groundwater $\delta^{18}O$ values. Meteoric calcite lines were characterized by average $\delta^{18}O$ values of -7.78‰ VPDB, and were used to calculate meteoric water compositions of -5.46 ± 0.56‰ VSMOW. *Positive linear covariant trends* in oxygen and carbon isotopic values were used to estimate evaporative losses of vadose groundwater that range from 8% to 12%. However, the presence of evaporite mineral molds indicates more extensive evaporation likely occurred during the deposition of the Tlayua Formation.

Sphaerosiderites from wetland paleosols of the Caballos Formation in Colombia produced meteoric sphaerosiderite lines that allowed estimation of precipitation $\delta^{18}O$ for the equatorial region around 2°S paleolatitude. The gleyed appearance and presence of sphaerosiderites themselves indicate that soils were primarily water-saturated. The presence of pyrite suggests occasional incursions of marine-influenced water which constrains the ancient soils to a coastal setting. Well-formed sphaerosiderites produce MSLs with an average oxygen isotopic composition

of -4.41 ± 0.37‰ (VPDB). The average oxygen isotopic composition of meteoric waters precipitating the sphaerosiderites is estimated at -4.56 ± 0.38‰ (VSMOW).

The additional isotopic data from the Tlayua Formation and the Caballos Formation are much lighter than what would be expected by extrapolation from the mid to high latitudes MSL data. The differences between extrapolations from a limited data set and the more complete data set presented in this study highlights the importance of greater spatial coverage for proxy data. This additional data is incorporated into a revised mass balance model that attempts to reproduce the components of the hydrologic cycle (precipitation, evaporation, relative humidity and terrestrial feedback) that influence the oxygen isotopic composition of precipitation. The simulated precipitation compositions are matched to within ±0.5‰ VSMOW of the empirically-derived meteoric water compositions. Model results suggest that precipitation fluxes and precipitation rates for the range of temperature gradients hypothesized for the Cretaceous are greater than modern fluxes and rates. The global average precipitation rate for the Cretaceous ranges between 371 mm/year to 1154 mm/year greater than modern precipitation rates. Precipitation rates are less than those initially proposed by Ufnar et al. (2002), but still greater (with the exception of the model based on cool Cretaceous temperature estimates of Barron, 1983) than GENESIS GCM precipitation rates (Poulsen et al., 2007). In addition to providing precipitation rate estimates, the model was tested to determine the sensitivity of different variables on the oxygen isotopic composition of rain water. These tests suggest that temperature and air mass origin and pathways have greatest impact on

model results, while relative humidity appears to play a greater role at low latitudes (subtropics). Enrichment of tropical and subtropical seawater $\delta^{18}O$ compositions was critical in matching oxygen isotopic compositions of precipitation in those latitudes. This supports other researchers' hypotheses that the Tethys Seaway was superheated and resulted in enriched and hypersaline waters (Woo et al., 1992; Johnson et al., 1996). The results of the research presented in this dissertation should be incorporated into GCMs to constrain boundary conditions and improve modeling of the Cretaceous hydrologic cycle, as well as forecasting future changes in the hydrologic cycle.

REFERENCES

Barron, E. J., 1983, Warm equable Cretaceous, The nature of the problem: Earth Science Reviews, v. 19, p. 305-338.

Johnson, C. C., Barron, E. J., Kauffmann, E. G., Arthur, M. A., Fawcett, P. J., Yasuda, M. K., 1996, Middle Cretaceous reef collapse linked to ocean heat transport: Geology, v. 24, p. 376-380.

Poulsen, C. J., Pollard, D., and White, T.S., 2007, General circulation model simulation of the $\delta^{18}O$ content of continental precipitation in the middle Cretaceous: a model-proxy comparison: Geology, v. 35, p. 199-202.

Ufnar, D. F., González, L.A., Ludvigson, G.A., Brenner, R.L., Witzke, B.J., 2002, The mid-Cretaceous water bearer: isotope mass balance quantification of the

Albian hydrologic cycle: Palaeogeography, Palaeoclimatology, Palaeoecology, v. 188, p. 51-71.

Woo, K. S., Anderson, T. F., Railsback, L. B., and Sandberg, P. A. , 1992, Oxygen isotopic evidence for high salinity surface seawater in the mid-Cretaceous Gulf of Mexico: Implications for warm, saline deepwater formation: Paleoceanography, v. 7, p. 673-685.

APPENDIX A. STABLE ISOTOPE DATA

The following tables contain stable carbon and oxygen isotopic compositions of calcite from the Tlayua Formation and siderite from the Caballos Formation. All data is given relative to VPDB.

Formation	Sample	$\delta^{18}O$	$\delta^{13}C$
Tlayua Formation	TXLA-1A-1	-10.98	-7.94
	TXLA-1B-2	-10.81	-7.82
	TXLA-1C-3	-9.94	-3.31
	TXLA-1D-4	-10.06	-5.06
	TXLA-2A-1	-10.12	-7.65
	TXLA-2A-2	-12.62	-9.09
	TXLA-2A-3	-9.30	-7.49
	TXLA-2B-4	-11.67	-8.45
	TXLA-2B-5	-9.12	-7.90
	TXLA-3-1	-7.61	-6.15
	TXLA-3-2	-6.36	-5.85
	TXLA-3-3	-5.79	-5.91
	TXLA-3-4	-6.07	-6.02
	TXLA-4-1	-9.68	-6.18
	TXLA-4-2	-9.32	-6.19
	TXLA-4-3	-8.14	-6.95
	TXLA-4-4	-6.49	-6.41
	TXLA-4-5	-7.05	-6.93
	TXLA-4RA-1	-7.13	-6.57
	TXLA-4RA-2	-7.09	-6.61
	TXLA-4R-4	-7.30	-6.61
	TXLA-4R-6	-7.14	-6.71
	TXLA-4R-7	-6.99	-6.66
	TXLA-4R-17a	-7.16	-6.68
	TXLA-4R-19a	-7.07	-6.60
	TXLA-4R-29a	-7.51	-6.74
	TXLA-4R-30a	-6.85	-6.53
	TXLA-4R-31a	-7.39	-6.67
	TXLA-4RB-1	-7.41	-6.41
	TXLA-4R-8	-7.49	-6.59
	TXLA-4R-9	-7.37	-6.57
	TXLA-4R-10	-7.18	-6.43
	TXLA-4R-20b	-7.54	-6.56
	TXLA-4R-21b	-7.56	-6.49
	TXLA-4R-22b	-7.30	-6.46
	TXLA-4RB-2	-7.44	-6.64
	TXLA-4R-11	-7.36	-6.65
	TXLA-4R-12	-7.34	-6.62
	TXLA-4R-13	-7.04	-6.51
	TXLA-4R-23c	-8.10	-6.78
	TXLA-4R-24c	-7.23	-6.49
	TXLA-4R-25c	-7.60	-6.87
	TXLA-4R-35c	-7.23	-6.61

Formation	Sample	$\delta^{18}O$	$\delta^{13}C$
	TXLA-4R-36c	-7.11	-6.54
	TXLA-4R-37c	-7.40	-6.56
	TXLA-4RB-3	-7.51	-6.77
	TXLA-4R-14	-7.33	-6.63
	TXLA-4R-15	-7.61	-6.83
	TXLA-4R-16	-7.16	-6.56
	TXLA-4R-26d	-7.227	-6.56
	TXLA-4R-27d	-7.186	-6.53
	TXLA-4R-28d	-7.625	-6.8
	TXLA-4R-32d	-7.163	-6.85
	TXLA-4R-33d	-7.258	-6.483
	TXLA-4R-34d	-7.473	-6.69
	TXLA-5-3	-5.71	-6.73
	TXLA-5-4	-5.49	-6.81
	TXLA-5-5	-11.37	-4.01
	TXLA-5-7	-4.95	-6.82
	TXLA-5-8	-4.81	-6.90
	TXLA-5-9	-5.70	-7.38
	TXLA-5-10	-6.18	-7.39
	TXLA-5-12	-5.54	-6.74
	TXLA-5-13	-5.52	-6.78
	TXLA-5-14	-5.69	-6.78
	TXLA-5-15	-5.41	-6.80
	TXLA-5-16	-5.43	-6.78
	TXLA-5-17	-5.37	-6.84
	TXLA-5R-1	-8.61	-5.83
	TXLA-5R-2	-8.40	-6.33
	TXLA-5R-3	-8.10	-6.53
	TXLA-5R-4	-8.34	-6.61
	TXLA-5R-5	-9.86	-5.24
	TXLA-5R-6	-8.54	-5.95
	TXLA-5R-7	-8.59	-5.91
	TXLA-5R-9	-7.85	-6.39
	TXLA-5R-10	-8.45	-6.39
	TXLA-5R-11	-8.45	-6.30
	TXLA-5R-13	-7.92	-6.45
	TXLA-5R-14	-8.23	-6.53
	TXLA-5R-15	-8.05	-6.47
	TXLA-5R-16	-8.03	-6.43
	TXLA-5R-17	-8.02	-6.46
	TXLA-6-1	-7.14	-7.21
	TXLA-6-3	-9.46	-7.85
	TXLA-7-1	-8.44	-7.43
	TXLA-7-2	-8.25	-7.50
	TXLA-7-3	-8.03	-7.56
	TXLA-8-1	-8.47	-8.22
	TXLA-8-2	-7.65	-8.27

Formation	Sample	$\delta^{18}O$	$\delta^{13}C$
	TXLA-8-3	-7.85	-7.94
	TXLA-8-4	-7.13	-8.05
	TXLA-8-5	-8.22	-8.13
	TXLA-8-6	-8.31	-8.08
	TXLA-9-1	-7.53	-7.34
	TXLA-9-2	-7.59	-7.62
	TXLA-9-3	-7.64	-7.66
	TXLA-9-4	-7.70	-7.18
	TXLA-9-5	-7.65	-7.13
	TXLA-9-6	-7.65	-7.18
	TXLA-9-7	-7.75	-7.33
	TXLA-9-8	-7.76	-7.33
	TXLA-9-9	-7.74	-7.33
	TXLA-9-10	-7.67	-7.57
	TXLA-9-11	-7.56	-7.52
	TXLA-9-12	-7.72	-7.57
	TXLA-9-13	-7.77	-7.70
	TXLA-9-14	-7.62	-7.61
	TXLA-9-15	-7.51	-7.63
	TXLA-9-16	-7.71	-7.82
	TXLA-9-17	-7.58	-7.65
	TXLA-10-2	-3.89	-6.09
	TXLA-10-3	-7.41	-6.70
	TXLA-10-4	-6.64	-6.76
	TXLA-10-5	-11.45	-6.88
	TXLA-11-1	-9.82	-5.47
	TXLA-11-2	-7.81	-6.40
	TXLA-11-3	-9.30	-5.62
	TXLA-11-4	-4.14	-4.80
	TXLA-11-5	-7.37	-6.48
	TXLA-12-1	-7.83	-6.61
	TXLA-12-7	-7.92	-6.58
	TXLA-12-8	-7.86	-6.62
	TXLA-12-9	-7.95	-6.59
	TXLA-12-10	-7.73	-6.56
	TXLA-12-23a	-7.72	-6.44
	TXLA-12-24a	-7.80	-6.48
	TXLA-12-25a	-8.24	-6.32
	TXLA-12-26a	-8.00	-6.66
	TXLA-12-27a	-7.77	-6.49
	TXLA-12-2	-7.68	-5.68
	TXLA-12-11	-7.58	-5.82
	TXLA-12-12	-7.76	-5.85
	TXLA-12-13	-7.94	-5.85
	TXLA-12-14	-8.16	-6.11
	TXLA-12-28b	-8.62	-6.26
	TXLA-12-29b	-7.88	-5.77

Formation	Sample	$\delta^{18}O$	$\delta^{13}C$
	TXLA-12-30b	-8.24	-5.90
	TXLA-12-31b	-8.29	-5.99
	TXLA-12-3	-8.75	-6.48
	TXLA-12-6	-8.54	-7.64
	TXLA-12-4	-7.35	-6.60
	TXLA-12-15	-7.31	-6.59
	TXLA-12-16	-7.13	-6.48
	TXLA-12-17	-7.33	-6.55
	TXLA-12-33c	-7.62	-6.56
	TXLA-12-34c	-7.24	-6.56
	TXLA-12-35c	-7.72	-6.69
	TXLA-12-36c	-7.27	-6.44
	TXLA-12-37c	-8.42	-7.16
	TXLA-12-5	-9.04	-6.46
	TXLA-12-19	-7.80	-6.79
	TXLA-12-20	-7.68	-6.63
	TXLA-12-21	-7.64	-6.77
	TXLA-12-22	-7.64	-6.75
	TXLA-12-38d	-7.58	-6.702
	TXLA-12-39d	-7.715	-6.664
	TXLA-12-40d	-7.647	-6.845
	TXLA-12-41d	-7.75	-6.726
	TXLA-12-42d	-7.568	-6.833
	TXLA-12C_mold2	-8.65	-6.06
	TXLA-12C_mold5	-8.32	-6.72
	TXLA-12C_lg_mold2	-7.96	-6.33
	TXLA-13-1	-7.24	-6.02
	TXLA-13-2	-9.69	-7.57
	TXLA-13-3	-7.27	-5.92
	TXLA-13-4	-7.09	-5.88
	TXLA-13-5	-7.50	-6.15
	TXLA-13-6	-7.27	-6.12
	TXLA-13-7	-7.37	-6.07
	TXLA-13-9	-7.39	-6.03
	TXLA-13-11	-7.37	-6.06
	TXLA-13-13	-7.04	-5.76
	TXLA-13-14	-6.96	-5.74
	TXLA-13-15	-7.05	-5.80
	TXLA-13-16	-7.09	-5.82
	TXLA-13-17a	-7.42	-6.15
	TXLA-13-18a	-7.10	-5.97
	TXLA-13-19a	-7.34	-6.02
	TXLA-13-20a	-7.56	-6.18
	TXLA-13-21a	-7.43	-6.04
	TXLA-13-22b	-7.42	-6.02
	TXLA-13-23b	-7.95	-6.43

Formation	Sample	$\delta^{18}O$	$\delta^{13}C$
	TXLA-13-24b	-7.32	-5.99
	TXLA-13-25b	-7.44	-6.01
	TXLA-13-26b	-7.43	-5.99
	TXLA-13-27c	-7.05	-5.72
	TXLA-13-28c	-7.24	-6.02
	TXLA-13-29c	-7.08	-5.82
	TXLA-13-30c	-7.06	-5.76
	TXLA-13-31c	-7.16	-5.81
	TXLA-13-32c	-7.03	-5.80
	TXLA-14B-1	-6.99	-6.04
	TXLA-14B-2	-6.72	-6.03
	TXLA-14B-3	-7.15	-5.97
	TXLA-16-1	-6.84	-5.13
	TXLA-16-3	-6.85	-5.03
	TXLA-16-4	-7.08	-5.10
	TXLA-16-5	-6.81	-5.18
	TXLA-16-6	-6.82	-5.08
	TXLA-16-7	-6.78	-5.15
	TXLA-16-8	-6.90	-5.21
	TXLA-16-10	-7.88	-5.14
	TXLA-16-11	-7.06	-5.06
	TXLA-16-12	-7.00	-5.08
	TXLA-16-13	-6.74	-5.04
	TXLA-16-14	-6.87	-5.03
	TXLA-16-15	-6.80	-5.04
	TXLA-17-1	-7.41	-5.15
	TXLA-17-2	-7.03	-4.88
	TXLA-17-3	-7.16	-4.97
	TXLA-17-5	-7.32	-5.11
	TXLA-17-6	-7.40	-5.24
	TXLA-17-7	-7.25	-4.94
	TXLA-17-8	-7.41	-5.07
	TXLA-17-9	-7.00	-4.80
	TXLA-17-10	-7.08	-4.75
	TXLA-17-11	-7.07	-4.92
	TXLA-17-12	-7.16	-4.94
	TXLA-17-13	-7.29	-5.09
	TXLA-17-14	-7.40	-5.39
	TXLA-17-15	-7.31	-5.09
	TXLA-18A-12	-7.38	-4.20
	TXLA-18A-17	-6.77	-4.76
	TXLA-18A-19	-7.39	-4.64
	TXLA-18A-15R	-7.43	-5.08
	TXLA-18A-23	-8.11	-4.34
	TXLA-18B-2	-6.99	-5.88
	TXLA-19-1	-6.84	-5.16

Formation	Sample	$\delta^{18}O$	$\delta^{13}C$
	TXLA-19-2	-6.53	-5.00
	TXLA-19-3	-7.10	-5.30
	TXLA-20-1	-5.95	-4.53
	TXLA-20-2	-4.42	-4.28
	TXLA-20-3	-9.66	-4.16
	TXLA-21A-1	-2.56	-4.21
	TXLA-21A-2	-3.60	-4.38
	TXLA-21A-3	-9.92	-5.29
	TXLA-21B-4	-2.25	-3.98
	TXLA-21a-6.1	-2.69	-4.21
	TXLA-21a-7.2	-3.39	-4.17
	TXLA-21a-8.2	-3.43	-4.30
	TXLA-21b-9.3	-2.57	-4.06
	TXLA-21b-10.3	-3.38	-4.30
	TXLA-21b-11.3	-2.35	-3.94
	TXLA-22B-1	-6.14	-3.66
	TXLA-22B-2	-6.37	-4.05
	TXLA-22B-3	-6.49	-4.17
	TXLA-22B-4	-7.37	-4.04
	TXLA-22b-6	-6.35	-3.91
	TXLA-22b-7	-6.29	-4.02
	TXLA-22b-8	-5.86	-3.83
	TXLA-22b-9	-6.63	-4.11
	TXLA-22b-10	-6.11	-3.84
	TXLA-22b-11	-6.37	-3.83
	TXLA-22b-12	-6.46	-4.07
	TXLA-22b-13	-6.34	-4.02
	TXLA-22b-14	-5.84	-3.70
	TXLA-22b-15	-5.99	-3.74
	TXLA-23-1	-7.01	-3.99
	TXLA-23-2	-6.40	-4.01
	TXLA-23-3	-6.25	-4.17
	TXLA-23-4	-6.70	-4.40
	TXLA-23-5	-6.43	-4.25
	TXLA-24-1	-9.04	-5.94
	TXLA-24-2	-9.28	-6.35
	TXLA-24-3	-9.02	-6.27
	TXLA-24-4	-6.60	-4.26
	TXLA-24-5	-8.80	-5.74
	TXLA-24-6	-8.88	-5.63
	TXLA-24-7	-9.60	-6.38
	TXLA-24-8	-9.33	-6.16
	TXLA-24-9	-9.10	-6.33
	TXLA-24-11	-9.45	-6.38
	TXLA-24-12	-9.02	-6.17
	TXLA-24-13	-9.12	-6.24
	TXLA-24-14	-6.43	-4.02

Formation	Sample	$\delta^{18}O$	$\delta^{13}C$
	TXLA-24-15	-6.45	-4.02
	TXLA-24-16	-6.62	-4.08
	TXLA-24-17	-8.77	-5.68
	TXLA-24-18	-8.75	-5.67
	TXLA-24-19	-8.63	-5.71
	TXLA-24-20	-9.04	-5.76
	TXLA-24-21	-8.81	-5.78
	TXLA-24-22	-8.89	-5.80
	TXLA-25A-1	-0.86	-2.64
	TXLA-25A-2	-0.68	-2.56
	TXLA-25A-3	-0.72	-2.52
	TXLA-25A-4	-9.46	-4.50
	TXLA-25a-5.1	-1.36	-2.83
	TXLA-25a-6.1	-0.85	-2.57
	TXLA-25a-7.2	-0.44	-2.68
	TXLA-25a-8.2	-0.86	-2.87
	TXLA-25a-9.3	-0.97	-2.55
	TXLA-25a-10.3	-0.97	-2.54
	TXLA-25a-11.3	-1.31	-2.86
	TXLA-26-1	-1.32	-1.31
	TXLA-26-2	-0.41	-1.00
	TXLA-26-3	-1.02	-1.21
	TXLA-26-4	-1.91	-2.69
	TXLA-26-5	-11.20	-4.83
	TXLA-26-6	-10.79	-7.07
	TXLA-26-8.1	-0.43	-0.89
	TXLA-26-9.1	-0.39	-0.88
	TXLA-26-10.2	-1.83	-2.69
	TXLA-26-11.2	-2.17	-2.39
	TXLA-26-12.2	-1.23	-2.11
	TXLA-27A-1	-8.59	-6.21
	TXLA-27A-2	-8.54	-6.83
	TXLA-27A-3	-8.74	-7.13
	TXLA-27B-4	-10.53	-5.61
	TXLA-27B-5	-8.88	-5.09
	TXLA-27A-6	-8.66	-6.19
	TXLA-27A-8	-8.77	-6.20
	TXLA-27A-9	-8.62	-7.33
	TXLA-27A-10	-8.98	-7.18
	TXLA-27A-11	-8.36	-6.75
	TXLA-27A-13	-8.68	-6.66
	TXLA-27A-14	-8.69	-6.71
	TXLA-27B-15	-10.56	-5.54
	TXLA-27B-16	-10.57	-5.31
	TXLA-27B-17	-10.38	-5.48
	TXLA-27B-18	-8.87	-5.22

Formation	Sample	$\delta^{18}O$	$\delta^{13}C$
	TXLA-27B-19	-8.94	-5.08
	TXLA-27B-20	-8.70	-5.25

Formation/Core	Sample	Depth (feet)	Depth (meters)	$\delta^{18}O$	$\delta^{13}C$
Caballos Formation/ San Francisco 52	SF-52 2864.75	2864.75	873.18	-4.02	-7.12
	SF-52 2864.75	2864.75	873.18	-3.77	-8.82
	SF-52 2864.75	2864.75	873.18	-4.15	-5.37
	SF-52 2864.75	2864.75	873.18	-3.82	-5.10
	SF-52 2864.75	2864.75	873.18	-3.87	-4.14
	SF-52 2864.75	2864.75	873.18	-3.73	-8.15
	SF-52 2864.75	2864.75	873.18	-4.43	-9.43
	SF-52 2864.75	2864.75	873.18	-3.97	-2.31
	SF-52 2864.75	2864.75	873.18	-4.11	-2.24
	SF-52 2864.75	2864.75	873.18	-3.74	-9.28
	SF-52 2845.54	2845.54	867.32	-2.38	-3.73
	SF-52 2845.54	2845.54	867.32	-4.56	-3.13
	SF-52 2845.54	2845.54	867.32	-4.56	-2.37
	SF-52 2845.54	2845.54	867.32	-4.18	-2.57
	SF-52 2845.54	2845.54	867.32	-3.99	-3.02
	SF-52 2845.54	2845.54	867.32	-4.72	-2.75
	SF-52 2845.54	2845.54	867.32	-4.93	-2.55
	SF-52 2845.54	2845.54	867.32	-5.09	-4.62
	SF-52 2845.54	2845.54	867.32	-4.46	-2.91
Los Mangos 04	M-04 3141	3141	957.38	-5.87	-14.41
	M-04 3141	3141	957.38	-4.84	-14.81
	M-04 3141	3141	957.38	-4.52	-15.22
	M-04 3141	3141	957.38	-4.64	-15.91
	M-04 3141	3141	957.38	-4.19	-14.79
	M-04 3141	3141	957.38	-5.17	-16.02
	M-04 3141	3141	957.38	-4.23	-14.91
	M-04 3141	3141	957.38	-4.86	-15.51
	M-04 3141	3141	957.38	-4.44	-15.61
	M-04 3141	3141	957.38		
	M-04 3141.75	3141.75	957.61	-3.57	-13.42
	M-04 3141.75	3141.75	957.61	-4.04	-13.86
	M-04 3141.75	3141.75	957.61	-3.43	-13.33
	M-04 3141.75	3141.75	957.61	-4.30	-13.67
	M-04 3141.75	3141.75	957.61	-3.50	-13.40
	M-04 3141.75	3141.75	957.61	-4.22	-13.90
	M-04 3141.75	3141.75	957.61	-3.48	-13.61
	M-04 3141.75	3141.75	957.61	-4.89	-13.56
	M-04 3141.75	3141.75	957.61	-3.82	-13.11
	M-04 3141.75	3141.75	957.61	-3.88	-13.01

Formation/Core	Sample	Depth (feet)	Depth (meters)	$\delta^{18}O$	$\delta^{13}C$
	M- 04 3148.85	3148.85	959.77	-4.48	-9.70
	M-04 3148.85	3148.85	959.77	-4.17	-11.59
	M-04 3148.85	3148.85	959.77	-3.49	-11.42
	M-04 3148.85	3148.85	959.77	-3.18	-11.98
	M-04 3148.85	3148.85	959.77	-4.03	-12.15
	M-04 3148.85	3148.85	959.77	-4.04	-9.51
	M-04 3148.85	3148.85	959.77	-3.67	-11.55
	M-04 3148.85	3148.85	959.77	-4.05	-11.91
	M-04 3148.85	3148.85	959.77	-3.89	-10.87
	M-04 3148.85	3148.85	959.77	-4.18	-11.90
	M-04 3149.38	3149.38	959.93	-5.94	-9.21
	M-04 3149.38	3149.38	959.93	-6.98	-10.11
	M-04 3149.38	3149.38	959.93	-8.80	-10.86
	M-04 3149.38	3149.38	959.93	-5.88	-10.28
	M-04 3149.38	3149.38	959.93	-6.42	-9.39
	M-04 3149.38	3149.38	959.93	-7.36	-8.15
	M-04 3149.38	3149.38	959.93	-6.71	-10.07
	M-04 3149.38	3149.38	959.93	-7.10	-9.06
San Francisco 52	SF52_2827.50-1	2827.50	861.82	-4.32	-8.06
	SF52_2827.50-2	2827.50	861.82	-4.35	-8.17
	SF52_2827.50-3	2827.50	861.82	-4.36	-6.22
	SF52_2827.50-4	2827.50	861.82	-4.52	-5.33
	SF52_2835.58-1	2835.58	864.28	-4.31	-10.08
	SF52_2835.58-10	2835.58	864.28	-5.65	-7.60
	SF52_2835.58-3	2835.58	864.28	-4.86	-11.29
	SF52_2835.58-4	2835.58	864.28	-4.19	-10.03
	SF52_2835.58-5	2835.58	864.28	-4.22	-11.94
	SF52_2835.58-6	2835.58	864.28	-4.69	-14.01
	SF52_2835.58-7	2835.58	864.28	-4.83	-11.18
	SF52_2835.58-9	2835.58	864.28	-4.83	-12.01
	SF52_2836.33-10	2836.33	864.51	-4.90	-12.89
	SF52_2836.33-4	2836.33	864.51	-6.56	-12.78
	SF52_2836.33-6	2836.33	864.51	-4.90	-10.47
	SF52_2836.33-7	2836.33	864.51	-4.54	-9.64
	SF52_2836.33-8	2836.33	864.51	-5.02	-11.46
	SF52_2836.33-9	2836.33	864.51	-5.45	-10.75
	SF52_2845.25-10	2845.25	867.23	-3.89	-3.63
	SF52_2845.25-2	2845.25	867.23	-4.21	-2.13
	SF52_2845.25-3	2845.25	867.23	-4.03	-2.47

Formation/Core	Sample	Depth (feet)	Depth (meters)	$\delta^{18}O$	$\delta^{13}C$
	SF52_2845.25-4	2845.25	867.23	-3.59	-2.97
	SF52_2845.25-5	2845.25	867.23	-5.36	-2.77
	SF52_2845.25-6	2845.25	867.23	-4.34	-2.62
	SF52_2845.25-7	2845.25	867.23	-3.80	-4.15
	SF52_2845.25-8	2845.25	867.23	-4.06	-3.92
	SF52_2845.25-9	2845.25	867.23	-4.24	-3.70
	SF52_2860.08-1	2860.08	871.75	-4.58	-8.99
	SF52_2860.08-2	2860.08	871.75	-4.64	-8.65
	SF52_2860.08-5	2860.08	871.75	-4.52	-8.56
	SF52_2860.08-6	2860.08	871.75	-4.29	-8.54
	SF52_2860.08-7	2860.08	871.75	-4.65	-7.80
	SF52_2860.08-8	2860.08	871.75	-4.10	-8.45
	SF52_2860.08-9	2860.08	871.75	-4.35	-8.37
	SF52_2860.08-10	2860.08	871.75	-4.71	-7.81
Santa Clara 2	SC2_2621.42-1	2621.42	799.01	-4.33	-2.37
	SC2_2621.42-2	2621.42	799.01	-4.18	-1.82
	SC2_2621.42-3	2621.42	799.01	-4.50	-2.46
	SC2_2621.42-4	2621.42	799.01	-4.48	-3.75
	SC2_2621.42-5	2621.42	799.01	-4.35	-5.38
	SC2_2621.42-6	2621.42	799.01	-4.25	-5.72
	SC2_2621.42-8	2621.42	799.01	-4.40	-5.62
	SC2_2621.88-2	2621.88	799.15	-4.80	-13.97
	SC2_2621.88-3	2621.88	799.15	-4.53	-14.01
	SC2_2621.88-5	2621.88	799.15	-4.48	-14.52
	SC2_2621.88-6	2621.88	799.15	-4.72	-14.45
	SC2_2621.88-7	2621.88	799.15	-4.55	-14.44
	SC2_2621.88-8	2621.88	799.15	-4.45	-15.04
	SC2_2621.88-10	2621.88	799.15	-4.65	-13.79
	SC2_2622.11-1	2622.11	799.22	-4.47	-13.91
	SC2_2622.11-2	2622.11	799.22	-4.74	-13.26
	SC2_2622.11-3	2622.11	799.22	-4.48	-13.39
	SC2_2622.11-4	2622.11	799.22	-4.59	-13.94
	SC2_2622.11-5	2622.11	799.22	-4.58	-10.82
	SC2_2622.11-7	2622.11	799.22	-4.40	-12.93
	SC2_2622.11-8	2622.11	799.22	-4.61	-12.45
San Francisco 52	SF52_2932.17-1	2932.17	893.73	-9.07	-2.26
	SF52_2932.17-2	2932.17	893.73	-7.82	-2.43
	SF52_2932.17-3	2932.17	893.73	-10.54	-1.52
	SF52_2932.17-4	2932.17	893.73	-9.16	-2.75

APPENDIX B. MSL, MCL, AND METEORIC WATER COMPOSITONS

The following tables provide the average oxygen isotopic compositions of meteoric sphaerosiderite lines and meteoric calcite lines relative to VPDB, and meteoric water compositions relative to VSMOW. Meteoric water compositions are calculated based on latitudinal temperature gradients.

Lat.	locality	$\delta^{18}O_{CO3}$	$\delta^{18}O_w$(leaf physiognomy)	$\delta^{18}O_w$ (cool Cretaceous)	$\delta^{18}O_w$ (warm Cretaceous)	$\delta^{18}O_w$ (KWI B-EM)
-2	Caballos Fm. (SF52_2864.75)	-3.96	-4.11	-5.10	-4.39	-2.90
-2	Caballos Fm. (SF52_2845.54)	-4.32	-4.47	-5.46	-4.75	-3.26
-2	Caballos Fm.(M4_3141)	-4.75	-4.90	-5.89	-5.17	-3.69
-2	Caballos Fm. (M4_3141.75)	-3.91	-4.06	-5.05	-4.34	-2.85
-2	Caballos Fm. (SF52_2827.50)	-4.39	-4.54	-5.53	-4.81	-3.33
-2	Caballos Fm. (SF52_2835.58)	-4.70	-4.85	-5.83	-5.12	-3.64
-2	Caballos Fm. (SF52_2836.33)	-5.23	-5.38	-6.36	-5.65	-4.17
-2	Caballos Fm. (SF52_2845.25)	-4.17	-4.32	-5.31	-4.59	-3.11
-2	Caballos Fm. (SF52_2860.08)	-4.48	-4.63	-5.62	-4.90	-3.42
-2	Caballos Fm. (SC2_2621.42)	-4.36	-4.51	-5.50	-4.78	-3.30
-2	Caballos Fm. (SC2_2621.88)	-4.60	-4.75	-5.73	-5.02	-3.54
-2	Caballos Fm. (SC2_2622.11)	-4.55	-4.70	-5.69	-4.98	-3.49
-2	Caballos Fm. (M4_3148.85)	-3.92	-4.07	-5.06	-4.35	-2.86
18.5	Tlayua Fm. (txla-9)	-7.66	-5.34	-5.97	-4.90	-5.06
18.5	Tlayua Fm. (txla-17/18)	-7.40	-5.09	-5.71	-4.64	-4.81
18.5	Tlayua Fm. (txla-27)	-8.71	-6.40	-7.03	-5.95	-6.12
18.5	Tlayua Fm. (txla-4r)	-8.10	-5.79	-6.42	-5.34	-5.51
18.5	Tlayua Fm. (txla-12b)	-8.29	-5.98	-6.61	-5.53	-5.70
18.5	Tlayua Fm. (txla-13)	-7.95	-5.64	-6.27	-5.19	-5.36
18.5	Tlayua Fm. (txla-22)	-6.63	-4.31	-4.94	-3.87	-4.03
18.5	Tlayua Fm. (txla-12a)	-7.88	-5.57	-6.20	-5.12	-5.29
18.5	Tlayua Fm. (txla-12c)	-7.49	-5.18	-5.81	-4.73	-4.90
18.5	Tlayua Fm. (txla-12d)	-7.67	-5.36	-5.98	-4.91	-5.08
25	Glen Rose Fm.	-5.66	-3.65	-4.28	-3.00	-3.74
25	Walnut Fm.	-6.50	-4.49	-5.12	-3.84	-4.58
29.5	Antlers Fm.	-8.20	-6.42	-7.08	-5.65	-6.79
29.5	Antlers Fm.	-7.50	-5.72	-6.38	-4.95	-6.09
34	Jones (Dak)	-5.10	-6.91	-7.73	-5.94	-7.67

Lat.	locality	$\delta^{18}O_{CO3}$	$\delta^{18}O_w$(leaf physiognomy)	$\delta^{18}O_w$ (cool Cretaceous)	$\delta^{18}O_w$ (warm Cretaceous)	$\delta^{18}O_w$ (KWI B-EM)
34	Jones (Dak)	-5.80	-7.61	-8.43	-6.63	-8.36
34	Cedar Moutain Fm.	-8.10	-6.55	-7.28	-5.68	-7.21
34	Cedar Moutain Fm.	-7.50	-5.95	-6.68	-5.08	-6.61
35	Dakota Fm.	-3.80	-5.68	-6.52	-4.67	-6.51
35	Dakota Fm.	-4.20	-6.07	-6.92	-5.07	-6.90
35	Dakota Fm.	-4.50	-6.37	-7.22	-5.37	-7.20
36	Dakota Fm.	-2.90	-4.84	-5.70	-3.81	-5.75
36	Dakota Fm.	-4.05	-5.98	-6.85	-4.96	-6.89
36	Dakota Fm.	-4.20	-6.13	-7.00	-5.11	-7.04
36	Dakota Fm.	-4.50	-6.43	-7.30	-5.41	-7.34
36	Dakota Fm.	-5.00	-6.93	-7.80	-5.91	-7.84
36	Dakota Fm.	-5.85	-7.78	-8.64	-6.76	-8.69
41	Mattagami Fm.	-5.80	-8.03	-9.03	-6.92	-9.35
45	Swan River Fm.	-8.00	-10.48	-11.62	-9.31	-12.14
46	Mannville Grp.	-6.85	-9.39	-10.58	-8.22	-11.15
46	Mannville Grp.	-7.60	-10.14	-11.32	-8.96	-11.89
46	Mannville Grp.	-8.10	-10.64	-11.82	-9.46	-12.39
46	Mannville Grp.	-8.30	-10.84	-12.02	-9.66	-12.59
46	Swan River Fm.	-5.60	-8.15	-9.33	-6.97	-9.90
48	Bow Island Fm.	-6.73	-9.40	-10.67	-8.21	-11.34
52	Boulder Ck Fm.	-10.45	-13.37	-14.83	-12.16	-15.69
52	Boulder Ck Fm.	-10.45	-13.37	-14.83	-12.16	-15.69
55	Dunvegan Fm.	-12.30	-15.42	-17.04	-14.20	-18.03
75	Nanushuk Grp.	-16.43	-20.98	-24.26	-20.02	-25.98
75	Nanushuk Grp.	-16.25	-20.80	-24.07	-19.83	-25.79
75	Nanushuk Grp.	-16.25	-20.80	-24.08	-19.84	-25.80
75	Nanushuk Grp.	-16.24	-20.79	-24.07	-19.83	-25.79
75	Nanushuk Grp.	-16.52	-21.07	-24.35	-20.11	-26.07
75	Nanushuk Grp.	-16.02	-20.57	-23.85	-19.60	-25.57
75	Nanushuk Grp.	-16.41	-20.96	-24.24	-20.00	-25.96
75	Nanushuk Grp.	-16.19	-20.74	-24.02	-19.78	-25.74
75	Nanushuk Grp.	-16.23	-20.78	-24.06	-19.82	-25.78

APPENDIX C. MODEL INPUTS AND RESULTS

These tables contain input variables and resulting isotopic compositions of precipitation from model outputs.

Lat.	MAT (modern)	Rel. hum.	$\delta^{18}O_{sw}$	Terr. Fdbck.	Evap. flux	Precip. Flux	$\delta^{18}O_{precip}$
0	30.11	99.00	1.10	0.00	0.89	0.53	-4.31
1	29.86	99.00	1.10	0.00	0.92	0.61	-4.27
2	29.60	99.00	1.10	0.00	0.95	0.70	-4.19
3	29.33	99.00	1.10	0.00	0.98	0.78	-4.09
4	29.05	99.00	1.10	0.00	0.97	0.80	-3.97
5	28.77	99.00	1.10	0.00	0.96	0.81	-3.84
6	28.48	99.00	1.13	0.01	0.95	0.83	-3.69
7	28.19	98.53	1.16	0.01	0.88	0.67	-3.58
8	27.89	98.07	1.19	0.02	0.81	0.51	-3.51
9	27.58	97.60	1.22	0.02	0.74	0.36	-3.48
10	27.26	97.28	1.25	0.03	0.67	0.34	-3.44
11	26.94	96.95	1.26	0.04	0.60	0.33	-3.88
12	26.61	96.63	1.27	0.06	0.55	0.30	-3.87
13	26.27	94.59	1.28	0.07	0.52	0.30	-3.85
14	25.93	92.54	1.29	0.09	0.49	0.29	-3.85
15	25.58	90.50	1.30	0.10	0.46	0.29	-3.86
16	25.22	88.56	1.32	0.10	0.45	0.29	-3.87
17	24.86	86.61	1.34	0.10	0.43	0.29	-3.89
18	24.49	84.67	1.36	0.10	0.42	0.29	-3.92
19	24.12	82.45	1.38	0.10	0.41	0.29	-3.95
20	23.73	80.22	1.40	0.10	0.40	0.29	-3.98
21	23.34	78.00	1.44	0.10	0.39	0.29	-4.02
22	22.95	74.33	1.48	0.10	0.39	0.28	-4.06
23	22.54	70.67	1.52	0.11	0.38	0.27	-4.11
24	22.13	67.00	1.56	0.11	0.38	0.26	-4.15
25	21.71	65.00	1.60	0.11	0.38	0.26	-4.21
26	21.29	63.00	1.56	0.11	0.38	0.26	-4.26
27	20.86	61.00	1.52	0.12	0.39	0.26	-4.32
28	20.42	60.33	1.48	0.12	0.38	0.27	-4.38
29	19.98	59.67	1.44	0.13	0.37	0.27	-4.44
30	19.53	59.00	1.40	0.13	0.36	0.28	-4.51
31	19.07	58.70	1.32	0.13	0.29	0.35	-4.57
32	18.61	58.40	1.24	0.14	0.21	0.42	-4.66
33	18.13	58.10	1.16	0.14	0.14	0.50	-4.78
34	17.66	58.30	1.08	0.15	0.11	0.51	-4.92

Lat.	MAT (modern)	Rel. hum.	$\delta^{18}O_{sw}$	Terr. Fdbck.	Evap. flux	Precip. Flux	$\delta^{18}O_{precip}$
35	17.17	58.50	1.00	0.15	0.09	0.53	-5.07
36	16.68	58.70	0.94	0.15	0.07	0.55	-5.22
37	16.18	60.13	0.88	0.16	0.06	0.56	-5.39
38	15.68	61.57	0.82	0.16	0.06	0.58	-5.56
39	15.17	63.00	0.76	0.17	0.05	0.59	-5.74
40	14.65	65.19	0.70	0.17	0.05	0.59	-5.93
41	14.12	67.39	0.56	0.17	0.04	0.59	-6.13
42	13.59	69.58	0.42	0.17	0.04	0.59	-6.33
43	13.05	71.72	0.28	0.17	0.04	0.59	-6.54
44	12.51	73.86	0.14	0.17	0.03	0.59	-6.76
45	11.95	76.00	0.00	0.17	0.03	0.59	-6.98
46	11.39	78.33	-0.10	0.17	0.03	0.58	-7.20
47	10.83	80.67	-0.20	0.17	0.03	0.58	-7.43
48	10.26	83.00	-0.30	0.17	0.03	0.57	-7.67
49	9.68	84.33	-0.40	0.18	0.03	0.57	-7.91
50	9.09	85.67	-0.50	0.18	0.02	0.57	-8.16
51	8.50	87.00	-0.54	0.18	0.02	0.57	-8.41
52	7.90	88.83	-0.58	0.18	0.02	0.57	-8.68
53	7.29	90.67	-0.62	0.18	0.02	0.56	-8.96
54	6.68	92.50	-0.66	0.18	0.02	0.56	-9.24
55	6.06	93.10	-0.70	0.18	0.02	0.55	-9.53
56	5.43	93.70	-0.76	0.18	0.01	0.54	-9.83
57	4.80	94.30	-0.82	0.18	0.01	0.53	-10.14
58	4.16	94.03	-0.88	0.19	0.01	0.52	-10.45
59	3.51	93.77	-0.94	0.19	0.01	0.51	-10.77
60	2.86	93.50	-1.00	0.19	0.01	0.50	-11.09
61	2.20	93.10	-1.04	0.19	0.01	0.48	-11.43
62	1.53	92.70	-1.08	0.19	0.01	0.47	-11.76
63	0.85	92.30	-1.12	0.18	0.01	0.45	-12.10
64	0.17	91.53	-1.16	0.18	0.01	0.44	-12.44
65	-0.51	90.77	-1.20	0.18	0.01	0.43	-12.79
66	-1.21	90.00	-1.26	0.18	0.01	0.42	-13.14
67	-1.91	87.27	-1.32	0.17	0.01	0.41	-13.50
68	-2.62	84.53	-1.38	0.17	0.01	0.40	-13.86
69	-3.33	81.80	-1.44	0.16	0.01	0.39	-14.23
70	-4.05	80.97	-1.50	0.16	0.01	0.38	-14.62
71	-4.78	80.13	-1.50	0.16	0.01	0.37	-15.01

Lat.	MAT (modern)	Rel. hum.	$\delta^{18}O_{sw}$	Terr. Fdbck.	Evap. flux	Precip. Flux	$\delta^{18}O_{precip}$
72	-5.52	79.30	-1.50	0.15	0.01	0.37	-15.41
73	-6.26	78.70	-1.50	0.15	0.01	0.36	-15.82
74	-7.01	78.10	-1.50	0.14	0.01	0.35	-16.25
75	-7.76	77.50	-1.50	0.14	0.01	0.34	-16.68
76	-8.52	77.07	-1.50	0.13	0.01	0.32	-17.12
77	-9.29	76.63	-1.50	0.12	0.01	0.31	-17.57
78	-10.07	76.20	-1.50	0.12	0.01	0.29	-18.00
79	-10.85	76.60	-1.50	0.11	0.01	0.28	-18.43
80	-11.64	77.00	-1.50	0.10	0.01	0.27	-18.87
81	-12.44	77.40	-1.54	0.08	0.01	0.26	-19.31
82	-13.24	78.93	-1.58	0.06	0.01	0.25	-19.75
83	-14.05	80.47	-1.62	0.04	0.01	0.25	-20.20
84	-14.86	82.00	-1.66	0.02	0.01	0.24	-20.66
85	-15.69	84.00	-1.70	0.00	0.01	0.24	-21.13
86	-16.52	86.00	-1.70	0.00	0.01	0.23	-21.61
87	-17.35	88.00	-1.70	0.00	0.01	0.23	-22.11
88	-18.19	88.17	-1.70	0.00	0.01	0.21	-22.63
89	-19.04	88.33	-1.70	0.00	0.01	0.20	-23.14
90	-19.90	88.50	-1.70	0.00	0.01	0.19	-23.64

Lat.	MAT (leaf phys.)	Rel. hum.	$\delta^{18}O_{sw}$	Terr. Fdbck	Evap. flux	Precip. Flux	$\delta^{18}O_{precip}$
0	30.25	99.00	1.40	0.00	0.99	0.88	-4.48
1	30.05	99.00	1.42	0.00	0.99	0.84	-4.39
2	29.84	99.00	1.45	0.00	1.00	0.80	-4.32
3	29.64	99.00	1.47	0.00	1.00	0.76	-4.26
4	29.43	99.00	1.50	0.00	1.00	0.70	-4.22
5	29.22	99.00	1.52	0.00	1.00	0.64	-4.20
6	29.01	99.00	1.52	0.01	1.00	0.58	-4.22
7	28.80	98.53	1.52	0.01	0.99	0.57	-4.19
8	28.59	98.07	1.52	0.02	0.98	0.56	-4.16
9	28.38	97.60	1.52	0.02	0.98	0.55	-4.14
10	28.17	97.28	1.52	0.03	0.83	0.54	-4.12
11	27.95	96.95	1.52	0.04	0.69	0.54	-4.13
12	27.73	96.63	1.52	0.06	0.55	0.53	-4.16
13	27.52	94.59	1.52	0.07	0.52	0.51	-4.21
14	27.30	92.54	1.52	0.09	0.49	0.50	-4.27
15	27.08	90.50	1.52	0.10	0.46	0.48	-4.33
16	26.86	83.83	1.52	0.10	0.45	0.44	-4.40
17	26.63	77.17	1.52	0.10	0.45	0.41	-4.47
18	26.41	70.50	1.52	0.10	0.44	0.37	-4.54
19	26.19	67.00	1.52	0.10	0.43	0.36	-4.62
20	25.96	63.50	1.52	0.10	0.42	0.35	-4.70
21	25.73	60.00	1.42	0.11	0.42	0.35	-4.78
22	25.50	56.50	1.31	0.11	0.41	0.34	-4.87
23	25.28	53.00	1.21	0.12	0.40	0.34	-4.96
24	25.04	49.50	1.10	0.12	0.40	0.33	-5.06
25	24.81	48.00	1.00	0.13	0.39	0.33	-5.16
26	24.58	46.50	0.94	0.14	0.39	0.33	-5.27
27	24.35	45.00	0.88	0.15	0.39	0.34	-5.38
28	24.11	44.83	0.82	0.15	0.38	0.35	-5.50
29	23.87	44.67	0.76	0.16	0.38	0.37	-5.61
30	23.64	44.50	0.70	0.17	0.37	0.39	-5.74
31	23.40	44.83	0.57	0.18	0.29	0.48	-5.87
32	23.16	45.17	0.44	0.18	0.21	0.56	-6.02
33	22.91	45.50	0.31	0.19	0.14	0.65	-6.19
34	22.67	47.00	0.18	0.19	0.11	0.69	-6.38
35	22.43	48.50	0.05	0.20	0.09	0.73	-6.58
36	22.18	50.00	-0.08	0.20	0.07	0.77	-6.80

Lat.	MAT (leaf phys.)	Rel. hum.	$\delta^{18}O_{sw}$	Terr. Fdbck	Evap. flux	Precip. Flux	$\delta^{18}O_{precip}$
37	21.94	52.83	-0.21	0.20	0.06	0.77	-7.04
38	21.69	55.67	-0.34	0.20	0.06	0.77	-7.28
39	21.44	58.50	-0.47	0.20	0.05	0.77	-7.53
40	21.19	62.19	-0.60	0.21	0.05	0.77	-7.78
41	20.94	65.89	-0.67	0.21	0.04	0.77	-8.04
42	20.69	69.58	-0.74	0.21	0.04	0.77	-8.31
43	20.43	71.72	-0.81	0.21	0.04	0.76	-8.58
44	20.18	73.86	-0.88	0.21	0.03	0.76	-8.86
45	19.92	76.00	-0.95	0.21	0.03	0.76	-9.15
46	19.67	78.33	-0.97	0.21	0.03	0.75	-9.45
47	19.41	80.67	-0.99	0.21	0.03	0.74	-9.76
48	19.15	83.00	-1.01	0.21	0.03	0.73	-10.07
49	18.89	84.33	-1.03	0.21	0.03	0.72	-10.39
50	18.63	85.67	-1.05	0.21	0.02	0.72	-10.72
51	18.36	87.00	-1.08	0.21	0.02	0.71	-11.06
52	18.10	88.83	-1.11	0.22	0.02	0.70	-11.41
53	17.83	90.67	-1.14	0.22	0.02	0.69	-11.77
54	17.57	92.50	-1.17	0.23	0.02	0.68	-12.13
55	17.30	93.00	-1.20	0.23	0.02	0.65	-12.51
56	17.03	93.50	-1.24	0.23	0.01	0.63	-12.89
57	16.76	94.00	-1.28	0.23	0.01	0.61	-13.27
58	16.49	93.67	-1.32	0.23	0.01	0.60	-13.66
59	16.21	93.33	-1.36	0.23	0.01	0.59	-14.07
60	15.94	93.00	-1.40	0.23	0.01	0.58	-14.48
61	15.66	92.67	-1.44	0.22	0.01	0.56	-14.91
62	15.39	92.33	-1.48	0.21	0.01	0.54	-15.34
63	15.11	92.00	-1.52	0.21	0.01	0.52	-15.78
64	14.83	91.33	-1.56	0.20	0.01	0.50	-16.22
65	14.55	90.67	-1.60	0.20	0.01	0.49	-16.67
66	14.27	90.00	-1.62	0.19	0.01	0.47	-17.12
67	13.99	87.27	-1.64	0.18	0.01	0.46	-17.59
68	13.71	84.53	-1.66	0.17	0.01	0.44	-18.06
69	13.42	81.80	-1.68	0.17	0.01	0.43	-18.54
70	13.14	80.97	-1.70	0.16	0.01	0.41	-19.04
71	12.85	80.13	-1.70	0.16	0.01	0.39	-19.54
72	12.56	79.30	-1.70	0.15	0.01	0.37	-20.03
73	12.27	78.70	-1.70	0.15	0.01	0.36	-20.53
74	11.98	78.10	-1.70	0.14	0.01	0.34	-21.04
75	11.69	77.50	-1.70	0.14	0.01	0.33	-21.55

Lat.	MAT (leaf phys.)	Rel. hum.	$\delta^{18}O_{sw}$	Terr. Fdbck	Evap. flux	Precip. Flux	$\delta^{18}O_{precip}$
76	11.39	77.07	-1.70	0.13	0.01	0.32	-22.08
77	11.10	76.63	-1.70	0.12	0.01	0.30	-22.60
78	10.80	76.20	-1.70	0.12	0.01	0.29	-23.14
79	10.51	76.60	-1.70	0.11	0.01	0.28	-23.68
80	10.21	77.00	-1.70	0.10	0.01	0.27	-24.23
81	9.91	77.40	-1.70	0.08	0.01	0.27	-24.80
82	9.61	78.93	-1.70	0.06	0.01	0.26	-25.39
83	9.31	80.47	-1.70	0.04	0.01	0.25	-26.00
84	9.01	82.00	-1.70	0.02	0.01	0.25	-26.62
85	8.70	84.00	-1.70	0.00	0.01	0.24	-27.27
86	8.40	86.00	-1.70	0.00	0.01	0.23	-27.94
87	8.09	88.00	-1.70	0.00	0.01	0.22	-28.62
88	7.78	88.17	-1.70	0.00	0.01	0.20	-29.31
89	7.47	88.33	-1.70	0.00	0.01	0.19	-30.01
90	7.17	88.50	-1.70	0.00	0.01	0.18	-30.70

Lat.	MAT (Cool Cret.)	Rel hum.	$\delta^{18}O_{sw}$	Terr. Fbck.	Evap. Flux	Precip. Flux	$\delta^{18}O_{precip}$
0	25.66	99.00	1.35	0.00	0.99	0.88	-4.86
1	25.60	99.00	1.37	0.00	0.99	0.84	-4.79
2	25.53	99.00	1.39	0.00	1.00	0.80	-4.73
3	25.45	99.00	1.41	0.00	1.00	0.76	-4.68
4	25.37	99.00	1.43	0.00	1.00	0.71	-4.65
5	25.27	99.00	1.45	0.00	1.00	0.66	-4.64
6	25.17	99.00	1.45	0.01	1.00	0.61	-4.67
7	25.07	98.53	1.45	0.01	0.99	0.60	-4.65
8	24.95	98.07	1.45	0.02	0.98	0.59	-4.63
9	24.83	97.60	1.45	0.02	0.98	0.58	-4.62
10	24.70	97.28	1.45	0.03	0.83	0.57	-4.61
11	24.56	96.95	1.43	0.04	0.69	0.57	-4.62
12	24.42	96.63	1.41	0.06	0.55	0.56	-4.66
13	24.26	94.59	1.39	0.07	0.52	0.54	-4.73
14	24.10	92.54	1.37	0.09	0.49	0.52	-4.80
15	23.93	90.50	1.35	0.10	0.47	0.50	-4.88
16	23.76	83.83	1.31	0.10	0.46	0.46	-4.96
17	23.58	77.17	1.27	0.10	0.45	0.41	-5.04
18	23.39	70.50	1.23	0.10	0.44	0.37	-5.12
19	23.19	67.00	1.19	0.10	0.44	0.36	-5.20
20	22.98	63.50	1.15	0.10	0.43	0.35	-5.29
21	22.77	60.00	1.01	0.11	0.43	0.35	-5.37
22	22.55	56.50	0.87	0.11	0.43	0.34	-5.47
23	22.32	53.00	0.73	0.12	0.43	0.34	-5.57
24	22.08	49.50	0.59	0.12	0.43	0.34	-5.67
25	21.84	47.33	0.45	0.13	0.43	0.35	-5.78
26	21.59	45.17	0.35	0.14	0.43	0.37	-5.91
27	21.33	43.00	0.25	0.15	0.43	0.38	-6.04
28	21.07	42.33	0.15	0.15	0.42	0.40	-6.18
29	20.79	41.67	0.05	0.16	0.42	0.42	-6.33
30	20.51	41.00	-0.05	0.17	0.41	0.44	-6.48
31	20.22	41.50	-0.15	0.18	0.32	0.51	-6.64
32	19.93	42.00	-0.25	0.18	0.23	0.58	-6.81
33	19.62	42.50	-0.35	0.19	0.14	0.65	-6.99
34	19.31	44.67	-0.45	0.19	0.11	0.70	-7.19
35	18.99	46.83	-0.55	0.20	0.09	0.74	-7.41
36	18.67	49.00	-0.61	0.20	0.07	0.79	-7.65

Lat.	MAT (Cool Cret.)	Rel hum.	$\delta^{18}O_{sw}$	Terr. Fbck.	Evap. Flux	Precip. Flux	$\delta^{18}O_{precip}$
37	18.33	51.50	-0.67	0.20	0.06	0.80	-7.90
38	17.99	54.00	-0.73	0.20	0.06	0.81	-8.16
39	17.64	56.50	-0.79	0.20	0.05	0.82	-8.44
40	17.29	60.86	-0.85	0.21	0.05	0.82	-8.72
41	16.92	65.22	-0.90	0.21	0.04	0.82	-9.02
42	16.55	69.58	-0.95	0.21	0.04	0.82	-9.32
43	16.17	71.72	-1.00	0.21	0.04	0.82	-9.63
44	15.79	73.86	-1.05	0.21	0.03	0.81	-9.96
45	15.39	76.00	-1.10	0.21	0.03	0.81	-10.30
46	14.99	78.00	-1.13	0.21	0.03	0.80	-10.65
47	14.58	80.00	-1.16	0.21	0.03	0.78	-11.00
48	14.16	82.00	-1.19	0.21	0.03	0.77	-11.37
49	13.74	83.33	-1.22	0.21	0.03	0.76	-11.74
50	13.31	84.67	-1.25	0.21	0.02	0.74	-12.13
51	12.87	86.00	-1.27	0.21	0.02	0.73	-12.52
52	12.42	87.67	-1.29	0.22	0.02	0.72	-12.93
53	11.97	89.33	-1.31	0.22	0.02	0.70	-13.35
54	11.51	91.00	-1.33	0.23	0.02	0.69	-13.78
55	11.04	92.10	-1.35	0.23	0.02	0.66	-14.22
56	10.56	93.20	-1.37	0.23	0.01	0.64	-14.66
57	10.07	94.30	-1.39	0.23	0.01	0.61	-15.12
58	9.58	94.03	-1.41	0.23	0.01	0.59	-15.58
59	9.08	93.77	-1.43	0.23	0.01	0.57	-16.05
60	8.57	93.50	-1.45	0.23	0.01	0.55	-16.53
61	8.06	93.10	-1.48	0.22	0.01	0.53	-17.02
62	7.54	92.70	-1.51	0.21	0.01	0.51	-17.51
63	7.01	92.30	-1.54	0.21	0.01	0.49	-18.02
64	6.47	91.53	-1.57	0.20	0.01	0.47	-18.53
65	5.93	90.77	-1.60	0.20	0.01	0.46	-19.06
66	5.37	90.00	-1.62	0.19	0.01	0.44	-19.59
67	4.81	87.27	-1.64	0.18	0.01	0.42	-20.14
68	4.25	84.53	-1.66	0.17	0.01	0.40	-20.70
69	3.67	81.80	-1.68	0.17	0.01	0.39	-21.26
70	3.09	80.97	-1.70	0.16	0.01	0.37	-21.84
71	2.50	80.13	-1.70	0.16	0.01	0.35	-22.42
72	1.90	79.30	-1.70	0.15	0.01	0.33	-23.00
73	1.29	78.70	-1.70	0.15	0.01	0.31	-23.58
74	0.68	78.10	-1.70	0.14	0.01	0.30	-24.17
75	0.06	77.50	-1.70	0.14	0.01	0.29	-24.77

Lat.	MAT (Cool Cret.)	Rel hum.	$\delta^{18}O_{sw}$	Terr. Fbck.	Evap. Flux	Precip. Flux	$\delta^{18}O_{precip}$
76	-0.57	77.07	-1.70	0.13	0.01	0.28	-25.38
77	-1.20	76.63	-1.70	0.12	0.01	0.27	-26.01
78	-1.84	76.20	-1.70	0.12	0.01	0.26	-26.66
79	-2.49	76.60	-1.70	0.11	0.01	0.24	-27.33
80	-3.15	77.00	-1.70	0.10	0.01	0.23	-28.00
81	-3.82	77.40	-1.70	0.08	0.01	0.22	-28.68
82	-4.49	78.93	-1.70	0.06	0.01	0.21	-29.36
83	-5.17	80.47	-1.70	0.04	0.01	0.20	-30.06
84	-5.86	82.00	-1.70	0.02	0.01	0.19	-30.78
85	-6.56	84.00	-1.70	0.00	0.01	0.18	-31.52
86	-7.26	86.00	-1.70	0.00	0.01	0.17	-32.26
87	-7.97	88.00	-1.70	0.00	0.01	0.16	-33.02
88	-8.69	88.17	-1.70	0.00	0.01	0.15	-33.77
89	-9.41	88.33	-1.70	0.00	0.01	0.14	-34.53
90	-10.15	88.50	-1.70	0.00	0.01	0.13	-35.29

Lat.	MAT (Warm Cret.)	Rel. hum.	$\delta^{18}O_{sw}$	Terr. Fdbck.	Evap. Flux	Precip. Flux	$\delta^{18}O_{precip}$
0	28.53	99.00	1.45	0.00	0.99	0.94	-4.28
1	28.58	99.00	1.50	0.00	0.99	0.88	-4.19
2	28.63	99.00	1.55	0.00	1.00	0.82	-4.13
3	28.67	99.00	1.60	0.00	1.00	0.76	-4.08
4	28.70	99.00	1.65	0.00	1.00	0.70	-4.06
5	28.73	99.00	1.70	0.00	1.00	0.64	-4.06
6	28.75	99.00	1.70	0.01	1.00	0.58	-4.09
7	28.76	98.53	1.70	0.01	0.99	0.57	-4.08
8	28.77	98.07	1.70	0.02	0.98	0.55	-4.07
9	28.77	97.60	1.70	0.02	0.98	0.54	-4.06
10	28.77	97.28	1.70	0.03	0.84	0.52	-4.05
11	28.76	96.95	1.70	0.04	0.70	0.50	-4.06
12	28.74	96.63	1.70	0.06	0.57	0.48	-4.09
13	28.72	95.09	1.70	0.07	0.54	0.45	-4.13
14	28.69	93.54	1.70	0.09	0.51	0.42	-4.18
15	28.65	92.00	1.70	0.10	0.49	0.39	-4.22
16	28.61	85.67	1.69	0.10	0.47	0.37	-4.27
17	28.57	79.33	1.68	0.10	0.46	0.35	-4.32
18	28.51	73.00	1.67	0.10	0.45	0.33	-4.38
19	28.45	69.17	1.66	0.10	0.44	0.32	-4.44
20	28.39	65.33	1.65	0.10	0.43	0.32	-4.51
21	28.32	61.50	1.62	0.11	0.43	0.32	-4.59
22	28.24	58.17	1.59	0.11	0.42	0.32	-4.68
23	28.16	54.83	1.56	0.12	0.42	0.32	-4.76
24	28.07	51.50	1.53	0.12	0.41	0.32	-4.86
25	27.97	49.67	1.50	0.13	0.41	0.32	-4.96
26	27.87	47.83	1.41	0.14	0.40	0.32	-5.06
27	27.76	46.00	1.32	0.15	0.40	0.32	-5.16
28	27.65	46.00	1.23	0.15	0.39	0.34	-5.27
29	27.53	46.00	1.14	0.16	0.38	0.36	-5.38
30	27.40	46.00	1.05	0.17	0.37	0.38	-5.50
31	27.27	46.33	0.90	0.18	0.29	0.47	-5.62
32	27.13	46.67	0.75	0.18	0.21	0.56	-5.76
33	26.98	47.00	0.60	0.19	0.14	0.65	-5.92
34	26.83	48.00	0.45	0.19	0.11	0.69	-6.10
35	26.68	49.00	0.30	0.20	0.09	0.73	-6.30
36	26.51	50.00	0.12	0.20	0.07	0.77	-6.51

Lat.	MAT (Warm Cret.)	Rel. hum.	$\delta^{18}O_{sw}$	Terr. Fdbck.	Evap. Flux	Precip. Flux	$\delta^{18}O_{precip}$
37	26.34	52.83	-0.06	0.20	0.06	0.77	-6.73
38	26.17	55.67	-0.24	0.20	0.06	0.77	-6.96
39	25.99	58.50	-0.42	0.20	0.05	0.77	-7.20
40	25.80	62.19	-0.60	0.21	0.05	0.77	-7.44
41	25.61	65.89	-0.67	0.21	0.04	0.77	-7.68
42	25.41	69.58	-0.74	0.21	0.04	0.77	-7.93
43	25.20	71.72	-0.81	0.21	0.04	0.76	-8.18
44	24.99	73.86	-0.88	0.21	0.03	0.76	-8.45
45	24.77	76.00	-0.95	0.21	0.03	0.76	-8.71
46	24.55	78.33	-0.97	0.21	0.03	0.75	-8.99
47	24.32	80.67	-0.99	0.21	0.03	0.74	-9.27
48	24.08	83.00	-1.01	0.21	0.03	0.73	-9.55
49	23.84	84.33	-1.03	0.21	0.03	0.72	-9.85
50	23.59	85.67	-1.05	0.21	0.02	0.72	-10.14
51	23.33	87.00	-1.08	0.21	0.02	0.71	-10.45
52	23.07	88.83	-1.11	0.22	0.02	0.70	-10.77
53	22.81	90.67	-1.14	0.22	0.02	0.69	-11.09
54	22.53	92.50	-1.17	0.23	0.02	0.68	-11.42
55	22.25	93.10	-1.20	0.23	0.02	0.66	-11.75
56	21.97	93.70	-1.24	0.23	0.01	0.64	-12.09
57	21.68	94.30	-1.28	0.23	0.01	0.62	-12.44
58	21.38	94.03	-1.32	0.23	0.01	0.61	-12.79
59	21.08	93.77	-1.36	0.23	0.01	0.60	-13.15
60	20.77	93.50	-1.40	0.23	0.01	0.59	-13.52
61	20.45	93.10	-1.44	0.22	0.01	0.58	-13.90
62	20.13	92.70	-1.48	0.21	0.01	0.57	-14.29
63	19.80	92.30	-1.52	0.21	0.01	0.56	-14.69
64	19.47	91.53	-1.56	0.20	0.01	0.55	-15.10
65	19.13	90.77	-1.60	0.20	0.01	0.54	-15.52
66	18.78	90.00	-1.62	0.19	0.01	0.53	-15.96
67	18.43	87.27	-1.64	0.18	0.01	0.52	-16.41
68	18.07	84.53	-1.66	0.17	0.01	0.51	-16.88
69	17.70	81.80	-1.68	0.17	0.01	0.50	-17.36
70	17.33	80.97	-1.70	0.16	0.01	0.48	-17.87
71	16.96	80.13	-1.70	0.16	0.01	0.46	-18.38
72	16.57	79.30	-1.70	0.15	0.01	0.44	-18.90
73	16.19	78.70	-1.70	0.15	0.01	0.42	-19.42
74	15.79	78.10	-1.70	0.14	0.01	0.40	-19.96
75	15.39	77.50	-1.70	0.14	0.01	0.39	-20.51

Lat.	MAT (Warm Cret.)	Rel. hum.	$\delta^{18}O_{sw}$	Terr. Fdbck.	Evap. Flux	Precip. Flux	$\delta^{18}O_{precip}$
76	14.98	77.07	-1.70	0.13	0.01	0.36	-21.06
77	14.57	76.63	-1.70	0.12	0.01	0.34	-21.62
78	14.15	76.20	-1.70	0.12	0.01	0.32	-22.18
79	13.72	76.60	-1.70	0.11	0.01	0.31	-22.73
80	13.29	77.00	-1.70	0.10	0.01	0.30	-23.30
81	12.85	77.40	-1.70	0.08	0.01	0.29	-23.88
82	12.41	78.93	-1.70	0.06	0.01	0.28	-24.47
83	11.96	80.47	-1.70	0.04	0.01	0.27	-25.08
84	11.50	82.00	-1.70	0.02	0.01	0.26	-25.72
85	11.04	84.00	-1.70	0.00	0.01	0.25	-26.38
86	10.57	86.00	-1.70	0.00	0.01	0.23	-27.04
87	10.10	88.00	-1.70	0.00	0.01	0.22	-27.71
88	9.62	88.17	-1.70	0.00	0.01	0.20	-28.37
89	9.13	88.33	-1.70	0.00	0.01	0.19	-29.04
90	8.64	88.50	-1.70	0.00	0.01	0.18	-29.70

Lat.	MAT (KWIB-EM)	Rel. hum.	$\delta^{18}O_{sw}$	Terr. Fdbck.	Evap. Flux	Precip. Flux	$\delta^{18}O_{precip}$
0	36.27	99.00	1.85	0.00	1.00	0.81	-3.54
1	35.84	99.00	1.88	0.00	1.00	0.76	-3.46
2	35.40	99.00	1.91	0.00	1.00	0.72	-3.40
3	34.95	99.00	1.94	0.00	1.00	0.67	-3.35
4	34.50	99.00	1.97	0.00	1.00	0.64	-3.30
5	34.05	99.00	2.00	0.00	1.00	0.61	-3.26
6	33.60	99.00	1.99	0.01	1.00	0.58	-3.54
7	33.14	98.53	1.98	0.01	0.99	0.60	-3.50
8	32.68	98.07	1.97	0.02	0.98	0.61	-3.47
9	32.22	97.60	1.96	0.02	0.98	0.63	-3.45
10	31.76	96.23	1.95	0.03	0.87	0.64	-3.43
11	31.29	94.87	1.94	0.04	0.77	0.64	-3.45
12	30.81	93.50	1.93	0.06	0.67	0.65	-3.49
13	30.34	90.00	1.92	0.07	0.66	0.64	-3.55
14	29.86	86.50	1.91	0.09	0.64	0.63	-3.62
15	29.37	83.00	1.90	0.10	0.63	0.62	-3.71
16	28.89	77.17	1.77	0.10	0.63	0.59	-3.80
17	28.40	71.33	1.64	0.10	0.62	0.56	-3.90
18	27.91	65.50	1.51	0.10	0.62	0.53	-4.01
19	27.41	62.50	1.38	0.10	0.62	0.53	-4.13
20	26.91	59.50	1.25	0.10	0.62	0.52	-4.26
21	26.41	56.50	1.04	0.11	0.62	0.52	-4.39
22	25.91	53.00	0.83	0.11	0.62	0.51	-4.54
23	25.40	49.50	0.62	0.12	0.62	0.51	-4.69
24	24.89	46.00	0.41	0.12	0.62	0.51	-4.85
25	24.37	44.67	0.20	0.13	0.62	0.52	-5.03
26	23.85	43.33	0.05	0.15	0.62	0.52	-5.21
27	23.33	42.00	-0.10	0.16	0.62	0.53	-5.40
28	22.81	41.00	-0.25	0.18	0.60	0.55	-5.60
29	22.28	40.00	-0.40	0.19	0.58	0.58	-5.80
30	21.75	39.00	-0.55	0.21	0.57	0.60	-6.01
31	21.21	39.50	-0.59	0.21	0.40	0.73	-6.23
32	20.68	40.00	-0.63	0.22	0.24	0.87	-6.47
33	20.13	40.50	-0.67	0.22	0.08	1.00	-6.72
34	19.59	41.83	-0.71	0.23	0.07	1.00	-7.01
35	19.04	43.17	-0.75	0.23	0.06	0.99	-7.30
36	18.49	44.50	-0.78	0.23	0.05	0.99	-7.60

Lat.	MAT (KWIB-EM)	Rel. hum.	$\delta^{18}O_{sw}$	Terr. Fdbck.	Evap. Flux	Precip. Flux	$\delta^{18}O_{precip}$
37	17.94	49.17	-0.81	0.23	0.04	0.99	-7.91
38	17.38	53.83	-0.84	0.23	0.04	0.99	-8.23
39	16.82	58.50	-0.87	0.23	0.03	0.99	-8.57
40	16.26	62.19	-0.90	0.23	0.03	0.98	-8.92
41	15.69	65.89	-0.94	0.23	0.03	0.97	-9.28
42	15.12	69.58	-0.98	0.23	0.03	0.97	-9.66
43	14.55	71.72	-1.02	0.23	0.03	0.93	-10.05
44	13.97	73.86	-1.06	0.23	0.03	0.90	-10.45
45	13.39	76.00	-1.10	0.23	0.03	0.86	-10.85
46	12.81	78.33	-1.13	0.23	0.02	0.83	-11.25
47	12.22	80.67	-1.16	0.23	0.02	0.80	-11.66
48	11.63	83.00	-1.19	0.23	0.02	0.77	-12.07
49	11.04	84.33	-1.22	0.23	0.02	0.74	-12.49
50	10.44	85.67	-1.25	0.24	0.02	0.71	-12.91
51	9.84	87.00	-1.28	0.24	0.02	0.69	-13.34
52	9.24	88.83	-1.31	0.24	0.01	0.67	-13.78
53	8.64	90.67	-1.34	0.24	0.01	0.65	-14.22
54	8.03	92.50	-1.37	0.24	0.01	0.64	-14.68
55	7.41	93.10	-1.40	0.24	0.01	0.62	-15.16
56	6.80	93.70	-1.44	0.24	0.01	0.61	-15.65
57	6.18	94.30	-1.48	0.24	0.01	0.59	-16.16
58	5.56	94.03	-1.52	0.24	0.01	0.57	-16.68
59	4.93	93.77	-1.56	0.24	0.01	0.56	-17.23
60	4.31	93.50	-1.60	0.24	0.01	0.54	-17.79
61	3.67	93.10	-1.63	0.24	0.01	0.50	-18.37
62	3.04	92.70	-1.66	0.23	0.01	0.46	-18.95
63	2.40	92.30	-1.69	0.23	0.01	0.42	-19.51
64	1.76	91.53	-1.72	0.22	0.01	0.40	-20.04
65	1.11	90.77	-1.75	0.22	0.01	0.38	-20.59
66	0.47	90.00	-1.78	0.21	0.01	0.37	-21.14
67	-0.18	87.27	-1.81	0.20	0.01	0.36	-21.70
68	-0.84	84.53	-1.84	0.18	0.01	0.35	-22.28
69	-1.50	81.80	-1.87	0.17	0.01	0.34	-22.88
70	-2.16	80.97	-1.90	0.16	0.01	0.31	-23.50
71	-2.82	80.13	-1.92	0.16	0.01	0.29	-24.12
72	-3.49	79.30	-1.94	0.15	0.01	0.27	-24.72
73	-4.16	78.70	-1.96	0.15	0.01	0.26	-25.31
74	-4.83	78.10	-1.98	0.14	0.01	0.25	-25.92
75	-5.51	77.50	-2.00	0.14	0.01	0.25	-26.55

Lat.	MAT (KWIB-EM)	Rel. hum.	$\delta^{18}O_{sw}$	Terr. Fdbck.	Evap. Flux	Precip. Flux	$\delta^{18}O_{precip}$
76	-6.19	77.07	-2.00	0.13	0.01	0.23	-27.21
77	-6.87	76.63	-2.00	0.12	0.01	0.22	-27.89
78	-7.56	76.20	-2.00	0.12	0.01	0.21	-28.57
79	-8.25	76.60	-2.00	0.11	0.01	0.20	-29.26
80	-8.94	77.00	-2.00	0.10	0.01	0.19	-29.96
81	-9.64	77.40	-2.00	0.08	0.01	0.18	-30.67
82	-10.34	78.93	-2.00	0.06	0.01	0.17	-31.38
83	-11.04	80.47	-2.00	0.04	0.01	0.17	-32.12
84	-11.75	82.00	-2.00	0.02	0.01	0.16	-32.88
85	-12.46	84.00	-2.00	0.00	0.01	0.15	-33.66
86	-13.17	86.00	-2.00	0.00	0.01	0.15	-34.46
87	-13.89	88.00	-2.00	0.00	0.01	0.14	-35.28
88	-14.60	88.17	-2.00	0.00	0.01	0.13	-36.13
89	-15.33	88.33	-2.00	0.00	0.01	0.12	-36.95
90	-16.05	88.50	-2.00	0.00	0.01	0.11	-37.74

APPENDIX D. PRECIPITATION RATES

The following table contains precipitation rates for modern observations from Alder et al., 2003, and model-derived precipitation rates for the Cretaceous based on the relationship between saturation vapor pressure and temperature. All values are in mm/year.

Lat.	Modern	Leaf Physiognomy.	Cool Cretaceous	Warm Cretaceous	Cretaceous WIB-EM
0	1387	2319	1822	2255	2851
1	1431	1975	1562	1911	2381
2	1534	1776	1415	1707	2099
3	1663	1635	1310	1555	1890
4	1834	1639	1341	1578	1935
5	1935	1561	1305	1521	1890
6	1985	1435	1230	1415	1820
7	1956	1718	1482	1709	2256
8	1890	2134	1851	2141	2901
9	1732	2774	2420	2805	3901
10	1573	2646	2319	2621	3750
11	1403	2423	2133	2347	3460
12	1288	2416	2135	2283	3475
13	1062	1975	1743	1823	2851
14	947	1745	1537	1569	2530
15	865	1578	1386	1376	2299
16	767	1302	1133	1176	1928
17	714	1121	964	1053	1695
18	692	997	845	979	1546
19	664	944	800	946	1462
20	628	879	746	901	1362
21	621	857	727	898	1326
22	621	878	749	941	1355
23	621	901	773	989	1386
24	621	926	797	1039	1419
25	621	941	844	1059	1431
26	627	967	900	1091	1458
27	654	1026	990	1159	1534
28	664	1090	1040	1251	1587
29	699	1200	1133	1397	1703
30	729	1308	1222	1542	1809
31	758	1329	1179	1606	1806
32	807	1401	1196	1725	1871
33	839	1452	1202	1814	1904
34	869	1565	1302	1966	1897
35	910	1701	1421	2149	1912
36	929	1800	1507	2286	1881

Lat.	Modern	Leaf Physiognomy.	Cool Cretaceous	Warm Cretaceous	Cretaceous WIB-EM
37	949	1823	1533	2326	1865
38	969	1848	1560	2369	1850
39	986	1867	1582	2404	1829
40	986	1897	1603	2452	1810
41	986	1927	1623	2501	1791
42	978	1945	1632	2534	1760
43	951	1924	1601	2515	1650
44	942	1942	1603	2547	1576
45	915	1922	1572	2528	1474
46	913	1950	1571	2573	1429
47	913	1987	1576	2627	1388
48	912	2024	1579	2682	1346
49	893	2007	1536	2665	1269
50	876	1996	1497	2655	1197
51	876	2024	1486	2695	1149
52	876	2056	1485	2741	1131
53	876	2089	1483	2788	1114
54	876	2124	1480	2836	1095
55	876	2146	1469	2881	1090
56	872	2159	1449	2914	1080
57	852	2131	1402	2892	1050
58	840	2161	1376	2932	1026
59	833	2208	1360	2994	1010
60	804	2196	1306	2975	966
61	779	2178	1271	2992	896
62	756	2161	1237	3011	827
63	704	2062	1157	2916	729
64	681	2037	1120	2916	694
65	633	1937	1043	2808	634
66	614	1919	1011	2819	604
67	585	1866	951	2758	573
68	559	1821	896	2709	545
69	503	1672	793	2502	488
70	458	1529	706	2293	424
71	401	1338	601	2012	352
72	356	1189	519	1793	295
73	330	1119	475	1674	274
74	303	1043	430	1549	252
75	276	966	387	1421	230

Lat.	Modern	Leaf Physiognomy.	Cool Cretaceous	Warm Cretaceous	Cretaceous WIB-EM
76	248	902	355	1296	208
77	218	824	319	1156	184
78	202	797	303	1086	172
79	190	779	282	1046	161
80	181	768	264	1014	151
81	179	789	257	1025	148
82	172	786	246	1007	142